國立交通大學

電子工程學系電子研究所

碩士論文

利用鐵鈦共鍍催化金屬合成柱狀結構之奈米碳管之場發射特性的研究

Study on the Field Emission Characteristics of the Carbon Nanotube Pillars Synthesized from an Fe-Ti Codeposited Catalyst

研究生：張佩琪

指導教授：鄭晃忠 博士

中華民國 九十六 年 七 月

利用鐵鈦共鍍催化金屬合成柱狀結構之奈米碳管之場發射特性的研究

Study on the Field Emission Characteristics of the Carbon Nanotube Pillars Synthesized from an Fe-Ti Codeposited Catalyst

研究生：張佩琪 Student: Pei-Chi Chang
指導教授：鄭晃忠 博士 Advisor: Dr. Huang-Chung Cheng

國立交通大學
電子工程學系 電子研究所碩士班
碩士論文

A Thesis
Submitted to Department of Electronics Engineering & Institute of Electronics
College of Electrical and Computer Engineering
National Chiao Tung University
In Partial Fulfillment of the Requirements
for the Degree of Master
in
Electronics Engineering
2007
Hsinchu, Taiwan, Republic of China

中華民國 九十六年七月

利用鐵鈦共鍍催化金屬合成柱狀之奈米碳管之場發射特性的研究

研究生：張佩琪　　　　　　指導教授：鄭晃忠 博士

國立交通大學電子工程學系　　電子研究所碩士班

摘　要

奈米碳管和基板附著性差會導致奈米碳管場發射特性的退化，而降低場發射的可靠度。在本論文，利用鐵和鈦的共鍍催化金屬來合成奈米碳管，可以改善場發射的可靠度，其中，鐵在催化金屬中的重量百分比為 64 %。使用這種鐵鈦共鍍催化金屬，成長出來的奈米碳管，其根部會部分鑲嵌在基板中，如此，增加了奈米碳管和基板的附著性，進而提升場發射可靠度。在 700 ℃下，利用這種催化金屬在熱化學氣相沈積中合成的奈米碳管，可以在 7.7 V/μm 的電場中維持一小時，保持約 30 mA/cm^2 的穩定電流密度。除此之外，在前處理之後，發現使用鐵鈦共鍍的催化金屬顆粒，較單獨使用鐵作催化金屬的顆粒來得小且均勻，因此，在 550 ℃的低溫下，成長出來的奈米碳管具有較大的成長速率，及較小的長度差異性。

使用這種鐵鈦共鍍作催化金屬的改良方式，前處理之後的催化金屬顆粒相當均勻，

並且相較於使用純鐵作催化金屬的方式，更能合成出高準直性的奈米碳管。這是因為均勻的催化金屬顆粒可使奈米碳管以相同的速率成長，而得到持續的凡得瓦爾力(van der Waals force)。因此，我們使用鐵鈦共鍍催化金屬方式來合成柱狀結構的奈米碳管，並利用微影方式控制柱體密度，來降低電場遮蔽效應。可利用調變柱體間的間距和高度，折衷電場遮蔽效應和場發射面積效應，來獲得最佳的場發射特性。根據本實驗，最佳的場發射特性存在於 R/H 為 2.5，開電場和起始電場均相當低，分別為 1.01 和 2.67 V/μm，電流密度也高達 256 mA/cm^2，並且在施加固定電場 5.33 V/μm 一小時中，場發射的可靠度亦相當良好，電流變異大約只有 20.59 %，平均電流密度約 18.94 mA/cm^2。因此，這種鐵鈦共鍍催化金屬合成的柱狀結構奈米碳管，具有相當潛力來應用在薄膜電晶體液晶顯示器上的背光源，以有效地降低製造材料成本。

Study on the Field Emission Characteristics of Carbon Nanotube Pillars Synthesized from an Fe-Ti Codeposited Catalyst

Student : Pei-Chi Chang　Advisor : Dr. Huang-Chung Cheng

Department of Electronic Engineering &
Institute of Electronics
National Chiao Tung University

Abstract

The weak adhesion between the carbon nanotubes (CNTs) and the substrate resulted in the field emission degradation of CNTs. It reduced the reliability of CNTs for field emission application. In this thesis, a proposed method was achieved to improve the reliability of CNTs by using an Fe-Ti codeposited thin film whose weight percentages of Fe was 64 % as catalyst layer. With the Fe-Ti codeposited catalyst, the roots of the CNTs exhibited a little inserted in the substrate to enhance the adhesion between the CNTs and the substrate. The CNTs synthesized at 700 ℃ in thermal CVD exhibited a stable emission current density with 30 mA/cm^2 at 7.7 V/μm for 3,600 sec. In addition, the catalyst nanoparticles after pretreatment for the Fe-Ti codeposited thin film were smaller and more uniform as compared with those for the pure Fe catalyst thin film. The growth rate and length variation of CNTs synthesized at a low temperature of 550 ℃ were thus improved by using an Fe-Ti codeposited catalyst.

With this proposed method, the catalyst nanoparticles after pretreatment were very uniform and could be utilized to grow the highly aligned CNTs with respect to the results from the pure Fe thin film. It was attributed to the lasting van der Waals force since these uniform catalyst nanoparticles could lead to the grown CNTs with the equal growth rate. Therefore, we utilized the proposed method to synthesize CNT pillars to reduce the screening effect via the pillar density control. By adjusting the interpillar spacing (R) and height (H) of CNT pillars, the optimization of the field emission characteristics was obtained from the compromise of the screening effect and emission sites. According to the works, the maximum of the field emission was obtained by an optimal R/H of 2.5. The effective turn-on field and effective threshold field were as low as 1.01 and 2.67 V/μm, respectively. In the mean while, the maximum current density was as high as 256 mA/cm^2. The reliability of the pillar arrays was determined by a stress test at 5.33 V/μm for 1 hour. It also showed an excellent reliability for the CNT pillars with the current variation coefficient of 20.59 %, and the mean current density of 18.94 mA/cm^2. As a result, the CNT pillars could be potentially applied in the back light unit for TFT-LCD to reduce the material cost.

誌 謝

很高興能夠在兩年的時間內順利攻讀碩士學位，感謝這兩年來許多人對我的幫助，以及所有在國立交通大學教導過我的老師，因為這些老師課堂上的教學，使我在學期間獲得豐富的知識，特別是我的指導教授-鄭晃忠博士，他課程上的教導，以及研究上的指導和啟發，使我研究事半功倍，除此之外，老師對學生的關心以及謙和的態度，讓我在碩士班的兩年中倍感溫馨。再來要感謝在研究上直接帶領我的賴瑞霖學長，謝謝他在實驗和論文撰寫上的幫助，並且常常在我實驗遇到挫折、緊張焦慮的時候，耐心地聽我抱怨、訴苦，並且給予引導和關心。還有謝謝已經畢業的許鈞凱學長和邰翰忠學長，他們在實驗上的經驗傳承和機台訓練。

其次，要感謝交通大學奈米中心（NFC）和國家毫微米實驗室（NDL）提供完善的實驗設備，尤其是要感謝奈米中心的技術人員-林聖欽先生、倪月珍小姐、范秀蘭小姐、陳明麗小姐、陳悅婷小姐、鄭淑娟小姐…等，在實驗設備及維護上給予最大的支持與協助，使我的研究得以順利完成。也感謝何惟梅小姐、顏似妙小姐和簡秀芳小姐在行政方面的協助，以及在大廳的張芬婷小姐和警衛伯伯。還有我曾經在 NFC 中打工的老闆-劉曉玲小姐，謝謝她對我的照顧，以及楊月嬌小姐和俞曉柔小姐的幫忙。

再來要謝謝所有 309B 實驗室的夥伴們，謝謝同組的林高照學長、陳俠威同學、林君翰學弟、李建穎學弟、和已經畢業的柳耀星學長，在研究和實驗上的互相幫忙和學習。還有已經畢業的魏瑛君學姊、林心瑜學姊、和許育瑛學妹，因為有她們在實驗室，使我傷心難過的時候有人陪伴，想吃大餐的時候也有人陪。另外，還有同居的王祐圻同學、韋凱方同學，謝謝他們和我一起分擔過很多實驗室的工作，以及在課業上和許多雜事上的幫忙。還要謝謝研究所的李克慧同學和張俐婷同學，有她們上課變得不無聊，以及張家豪同學在機台操作上和簽 RUN 的協助。還有其他沒有提到的人，只要你有看到這本論文，就要知道我也謝謝你們 ☺

最後，我要大大的感謝我的家人支持我來交大讀電子所，並提供我長年在新竹的各樣開銷，還有要感謝所有關心我的教會朋友，及那愛我的上帝。

Contents

Chapter 1 Introduction

Chapter 2 The Field Emission Characteristics of Carbon Nanotubes Synthesized from an Fe-Ti Codeposited Catalyst

Chapter 3 The Field Emission Characteristics of Carbon Nanotube Pillars Synthesized from an Fe-Ti Codeposited Catalyst

Table Lists

Chapter 1

Chapter 3

Figure Captions

Chapter 1

Chapter 2

Chapter 3

Chapter 1

Introduction

1.1 Overview of Vacuum Microelectronics

1.1.1 History

Since the invention of solid state transistors by John Bardeen, Walter Bratain, and William Shockley in 1948[1.1], vacuum tubes have been gradually replaced by those tiny volume, low cost, better reliability, and more power efficient solid state devices. The so called vacuum microelectronic devices using the professional micro fabrication technology have been successfully fabricated and gave a new life to vacuum electronics due to great improvements on semiconductor manufacturing technology for the past decades. “Vacuum state” devices have many superior advantages with respect to the present “solid state” devices, including radiation hardness, temperature insensitivity, and fast drift velocity. For example, there is negligible radiation effect in vacuum devices due to medium being damaged as the electrons fly in the vacuum [1.2]. Moreover, there is no medium for electrons fly in the vacuum, so there is no lattice scattering or bulk carrier generation/recombination. Therefore, the vacuum microelectronic devices can suffer to 500 ℃ or above as long as the structures of the vacuum devices do not destroyed. Additionally, the saturation drift velocity is limited to less than 3×10^{7} cm/s in all semiconductor due to scattering mechanism whereas the saturation drift velocity in vacuum is limited theoretically to 3×10^{10} cm/s and practically to about $6\text{-}9\times10^{8}$ cm/s [1.3]. Table 1-1 shows the comparison between vacuum microelectronic and semiconductor devices.

Vacuum electronics can be broadly separated into two categories: Thermionic emission or Field emission. The theory of field emission started in 1928, when R. H. Fowler and L. W.

Nordheim published the first theory of electron field emission (Fowler- Nordheim theory) from metals using quantum mechanics [1.4]. The difference concerns the way electrons are emitted from the cathode. Thermionic emission relies on a heated electron emitter, or cathode. The cathode is heated up enough such that the electrons receive enough kinetic energy to leave the surface of the cathode. Field emission, unlike thermionic emission, is possible with a cold cathode. Field emission is a form of quantum tunneling in which electrons pass through a barrier in the presence of a high electric field. This phenomenon is highly dependent on both the properties of the material and the shape of the particular cathode, so that higher aspect ratios produce higher field emission currents. According to the Fowler-Nordheim theory, an applied electric field of approximately 103 V/m is needed for electrons to tunnel through the sufficiently narrow barrier [1.2]. To reach this high field at reasonable applied voltage, it is customary to machine the field emitters into protruding objects to take advantage of field enhancement. It was not until 1968 when C. A. Spindt camp up with a fabrication method to create very small dimension metal cones that vacuum microelectronic triodes became possible [1.2]. Figure 1-1 is a schematic diagram of the triode fabricated by Spindt [1.5]. From the late 1960s to the year 1990, Ivor Brodie, Henry F. Gray, and C. A. Spindt made many contributions to this field. Also, most of research was focused on the devices similar to the Spindt cathode during the past three decades.

In 1991, a group of research of the French company LETI CHEN reported a microtip display at the fourth International Vacuum Microelectronics Conference [1.6]. Their display was the first announcement of a practical vacuum microelectronic device. From then on, a great amount of researchers all over the world devoted themselves to this interesting, challenging, and inventive field. Part of the work focused on fabricating very small radius silicon tip by utilizing modern VLSI technology [1.7-1.8]. Some of them increased the emission current by coating different metals, such as W, Mo, Ta, Pt etc., even diamond on field emission arrays [1.9-1.10]. Different device schemes also have been proposed to enhance the emission current density, stability, and reliability.

1.1.2 Applications of Vacuum Microelectronic Devices

Due to the superior properties of vacuum microelectronic devices, potential applications include high efficiency microwave amplifier and generator [1.11-1.13]. ultra-fast computer, scanning electron microscopy, electron/ion source [1.14-1.15], electron beam lithography, micro-sensor [1.16-1.17], temperature insensitive electronics, radiation hardness analog, and high brightness field emission flat-panel display [1.18-1.21].

Among these applications of the vacuum microelectronics, the first commercial product could be the field emission flat-panel display. The field emission fluorescent display is basically a thin cathode ray tube (CRT), which was first proposed by SRI International and later demonstrated by LETI [1.22].

Various kinds of flat-panel displays, such as liquid crystal display (LCD), light emitting display (LED), vacuum fluorescent display (VFD), plasma display panel (PDP), and electroluminescent display (EL), are developed for the better characteristics of small volume, light weight, and low power consumption. LCDs have become the most popular flat panel displays, however, LCDs have some drawbacks, such as poor viewing angle, temperature sensitivity and low brightness. As a result, some opportunities still exist and waiting for the solutions from other flat panel displays such as field emission display (FED).

1.1.3 Field Emission Displays

A FED is a type of flat panel display using field emitting cathodes to bombard phosphor coatings as the light emissive medium. It is similar to CRT, however it is much thinner than CRT. It uses a large array of fine metal tips or CNTs with many positioned behind each phosphor dot instead of electron gun to emit electrons through a process known as field emission. It has both advantages of CRT (picture quality) and PDP (flatness) which has been evaluated as a next-generation technology of low price and superior quality. The schematic comparisons are revealed in Fig. 1-2[1.23].

Compared to the active matrix LCDs and PDPs, FEDs are energy efficient and could provide a flat panel technology that features less power consumption. They can also be cheaper to make, as they have fewer total components. Moreover, FEDs could generate three times the brightness with wilder viewing angle at the same power level. Full color FEDs have been developed by various research groups from different aspects such as Motorola, PixTech, Futaba, Sony/Candescent, Samsung, and Canon-Toshiba are presently engaged in commercially exploiting FEDs. The products of above mentioned companies are shown in Fig. 1-3.

1.1.4 Theory Background

Electron field emission is a quantum mechanical tunneling phenomenon of electrons extracted from the conductive solid surface, such as a metal or a semiconductor, where the surface electric field is extremely high. If a sufficient electric field is applied on the emitter surface, electrons will be emitted through the surface potential barrier into vacuum, even under a very low temperature. In contrast, thermionic emission is the hot electron emission under high temperature and low electric field. Figure 1-4(a) demonstrates the band diagram of a metal-vacuum system.

Here W_0 is the energy difference between an electron at rest outside the metal and an electron at rest inside the metal, whereas W_f is the energy difference between the Fermi level and the bottom of the conduction band. The work function ϕ is defined as $\phi = W_0 - W_f$. If an external bias is applied, vacuum energy level is reduced and the potential barrier at the surface becomes thinner as shown in Fig. 1-4(b). Then, an electron having energy “W” has a finite probability of passing through the surface barrier. Fowler and Nordheim derive the famous F-N equation (1.1) as follow [1.4]:

$$J = \frac{aE^2}{\phi t^2(y)} \exp[-b\phi^{\frac{3}{2}} v(y)/E], \tag{1-1}$$

where J is the current density (A/cm^2). E is the applied electric field (V/cm), ϕ is the work function (in eV), a = 1.56×10^{-6}, b = -6.831×10^{-7}, y = 3.79x10^{-4}×10^{-4}E$^{1/2}$/ϕ, t^2(y)~1.1 and v(y) can be approximated as [1.24]

$$v(y) = \cos(0.5\pi y), \tag{1-2}$$

or

$$v(y) = 0.95 - y^2. \tag{1-3}$$

Typically, the field emission current I is measured as a function of the applied voltage V. Substituting relationships of J = I/α and E = βV into Eq.(1-1), where α is the emitting area and β is the local field enhancement factor at the emitting surface, the following equation can be obtained

$$I = \frac{A\alpha\beta^2 V^2}{\phi t^2(y)} \exp[-bv(y)\frac{\phi^{\frac{3}{2}}}{\beta V}]. \tag{1-4}$$

Then taking the log. form of Eq. (1-4) and v(y) ~ 1

$$\log(\frac{I}{V^2}) = \log[1.54\times10^{-6}\frac{\alpha\beta^2}{\phi t^2(y)}] - 2.97\times10^7(\frac{\phi^{3/2} v(y)}{\beta V}), \tag{1-5}$$

from Eq. (1-5), the slope of a Fowler-Nordheim (F-N) plot is given by

$$S \equiv slope_{FN} = -2.97\times10^7(\frac{\phi^{\frac{3}{2}}}{\beta}). \tag{1-6}$$

The parameter β can be evaluated from the slope S of the measured F-N plot if the work function ϕ was known

$$\beta = -2.97\times 10^{7}\left(\frac{\phi^{\frac{3}{2}}}{S}\right)\ \ (\mathrm{cm}^{-1}). \qquad (1\text{-}7)$$

The emission area α can be subsequently extracted from a rearrangement of Eq. (1-5)

$$\alpha = \left(\frac{I}{V^{2}}\right)\frac{\phi}{1.4\times 10^{-6}\beta^{2}}\exp\left(\frac{-9.89}{\sqrt{\phi}}\right)\exp\left(\frac{6.53\times 10^{7}\phi^{\frac{3}{2}}}{\beta V}\right)\ \ (\mathrm{cm}^{2}). \qquad (1\text{-}8)$$

For example, the electric field at the surface of a spherical emitter of radius r concentric with a spherical anode (or gate) of radius r+d can be represented analytically by

$$E = \frac{V}{r}\left(\frac{r+d}{d}\right). \qquad (1\text{-}9)$$

Though a realistic electric field in the emitter tip is more complicated than above equation, we can multiple Eq.(1-9) by a geometric factor β` to approximate the real condition.

$$E_{tip} \equiv \text{function of (r,d)} = \beta`\frac{V}{r}\left(\frac{r+d}{d}\right), \qquad (1\text{-}10)$$

where r is the tip radius of emitter tip, d is the emitter-anode(gate) distance and β` is a geometric correction factor [1.25].

For a very sharp conical tip emitter, where d >> r, E_{tip} approaches to β`(V/r). And for r>>d, $E_{tip}$ approaches to $\beta$`(V/d) which is the solution for a parallel-plate capacitor and for a diode operation in a small anode-to-cathode spacing.

As the gated FEA with very sharp tip radius, Eq. (1-10) can be approximated as:

$$E_{tip} = \beta`(V/r). \qquad (1\text{-}11)$$

Combining E = βV and Eq. (1-11), we can obtain the relationship:

$$E_{tip} = \beta V = \beta`(V/r),\ \text{and}\ \ \beta` = \beta r. \qquad (1\text{-}12)$$

The tip radius r is usually in the range from a few nm to 50 nm, corresponding to the parameter β` ranging from 10^{-1} to 10^{-2}.

Besides, transconductance g_m of a field emission device is defined as the change in anode current due to a change in gate voltage [1.1].

$$g_m = \frac{\partial I_C}{\partial V_g}|_{Vc}. \qquad (1\text{-}13)$$

Transconductance of a FED is a figure of merit that gives as an indication of the amount of current charge that can be accomplish by a given change in grid voltage. The transconductance can be increase by using multiple tips or by decreasing the gate-to-cathode spacing for a given anode-to-cathode spacing.

According to the above mention equations (especially Eq.1-5), the following approaches may therefore be taken to reduce the operating voltage of the field emission devices:

1) To find techniques to reproducibly sharpen the tips to the atomic level (increase β).
2) To lower the work function of the tip (ϕ).
3) To narrow the cone angle (increase β).
4) To reduce the gate-opening diameter (increase β).

1.2 Cathode Structures and Materials for Field Emission Displays

Field emission display is one of the most promising emissive type flat-panel displays, which can overcome the drawbacks of TFT-LCD, such as poor viewing angle, temperature sensitivity, low contrast and low brightness. This section introduces some novel cathode structures and synthesizes these novel emitter materials for FED operations.

1.2.1 Spindt-type Field Emitters

The “Spindt” cathode was first proposed by C. A. Spindt in 1968 [1.26]. The scanning electron microscope (SEM) image of a spindt type field emission triode has been shown in Fig. 1-1. It was first invented by Spindt of SRI and improved for the electron source of high-speed switching devices or microwave devices [1.2]. In 1970s, Meyer of LETI applied Spindt-typed emitters for a display and introduce a resistive layer as the feedback resistance to stabilizing the field emission from Spindt-type emitters [1.27].

The structure of Spindt-type FED includes a substrate, a cathode electrode of an electron emission unit formed thereon having a substantially conical shape, and a gate electrode of a lead-out electrode stacked on a substrate around the cathode electrode having an insulating layer. In the Spindt type FED a voltage is applied between the cathode electrode and the gate electrode in a vacuum to thereby produce a high electric field. As a result, electrons are emitted from a tip end of the cathode electrode through the electron emission mechanism in an electric field. In addition, the Spindt-type FED has a conical electron emission portion formed on a cathode electrode. It higher electron drawing efficiency since the electron emission portion is arranged in the vicinity of the center of the gate electrode where the electric field is most concentrated, and the directivity of electron emission is regular.

The merits of the Spindt-type field emitters are summarized as following: (1) High emission current efficiency, more than 98 % anode current to cathode current can be achieved for the symmetric structure of Spindt tip and the gate hole, the lateral electric field to the metal tip can be cancelled out. (2) The fabrication is self-aligned, easy process; uniform field emission arrays can be fabricated easily. Some research groups have successfully fabricated commercial FED products based on Spindt-type field emitters such as motorola, Pixtech, Futaba and Sony/Candesent.[1.28], the products of above mentioned companies are shown in Fig. 1-3.

However, there are some drawbacks of Spindt-type field emitters when fabricating Spindt-type FED such as (1) High gate driving voltage required; for a Spindt-type field emission triode with 4 μm gate aperture, the driving voltage is typically more than 60 V, which results in the high cost of the driving circuits. To reduce the gate driving voltage, frontier lithography technologies such as E beam lithography must be applied to reduce the gate aperture to the sub-micron level. (2) The emission property degrades for the chemically instable of the metal tips. (3) Huge, expensive high vacuum deposition system required during fabricating large area Spindt-type FED.

1.2.2 Si Tip Field Emitters

An alternative approach to fabricate tip type field emitters is to fabricate the Si tip field emitters based on the semiconductor fabricating process. Figure 1-5 depicts the SEM micrographs of Si tips array, Si tip field emission triodes array formed by chemical mechanical polishing (CMP) [1.29] and double gate of Si field emitter arrays [1.30]. Symmetric device structure and similar advantages with Spindt-type field emitters can be obtained. However, high temperature oxidation sharpening process prohibits Si tip from large area fabrication.

1.2.3 Surface Conduction Electron Emitter (SCE)

A surface conduction electron emitter display (SED) is a flat panel display technology that uses surface conduction electron emitters for every individual display pixel. The surface conduction emitter emits electrons that excite a phosphor coating on the display panel, the same basic concept found in traditional CRT televisions. The key technology to the electron emitters begins with the creation of an extremely narrow slits (~ several nanometers) between two electric poles in thin film of PdO (Palladium Oxide). Electrons are emitted from one side of the slit when approximately 10 V of electricity are applied. Some of these electrons are scattered at the other side of the silt and accelerated by the voltage (approximately 10 kV) applied between the glass substrates; causing light to be emitted when they collide with the phosphor-coated glass plate. The PdO film is coated by inject printing or screen-printing technology and this is a low cost process. This means that SEDs use small cathode ray tubes behind every single pixel (instead of one tube for the whole display) and can combine the slim form factor of LCDs and plasma displays with the superior viewing angles, contrast, black levels, color definition and pixel response time of CRTs. The major problem of SED is that the efficiency is still low and the power consumption will be very high. Figure 1-6 shows the SEM image of SCE cathode array, structure and a 36-inch display of SED [1.31-1.32].

The research of SED was began by Canon in 1986, and in 2004, Toshiba and Canon announced a joint development agreement originally targeting commercial production of SEDs. In October 2006, Toshiba's president announced the company plans to begin full production of 55" SED TVs in 2007. In December 2006, Toshiba President and Chief Executive Atsutoshi Nishida said Toshiba is on track to mass-produce SED TV sets in cooperation with Canon by 2008.

1.2.4 Carbon and Nano-sized Emitters

Carbon and nano-sized emitters is so-called carbon nanotube (CNT), is known to be useful for providing electron emission in field emission devices, such as cold cathodes that are used in a field emission display. Although Spindt-type emitters are generally used for FEDs, they still have a problem in that the life span of micro-tips is shortened due to atmospheric gases or a non-uniform field during a field emission operation. Moreover, the work function of the conventional metal emitters is too high to decrease a driving voltage for field emission. To overcome the problem, CNTs which have a substantially high aspect ratio, excellent durability due to their structure and excellent electron conductivity have been instead of Spindt-type emitters for field emission. CNTs are are anticipated to be an ideal electron emission source since they feature a low work function, the resultant electron emission source can be driven by applying low voltages, and the method of fabricating the same is not complicated. They will thereby offer advantages to realize a large size panel display in terms of view angle, definition, power consumption, and temperature stability.

1.3 Field Emission Properties of Carbon Nanotubes

1.3.1 Structure and Properties of Carbon Nanotubes

Recently, carbon nanotubes have attracted a lot of attention owing to their unique properties and potential for various applications. The discovery of CNTs occurred in 1991 as Sumio Iijima of NEC Corporation found these tiny needles, consisting of concentric graphite tubes, on the electrodes used to prepare fullerenes [1.33]. CNTs can be divided into two categories. The first is called multiwalled carbon nanotubes (MWNTs). MWNTs are close to hollow graphite fibers [1.34], except that they have a much higher degree of structural perfection. They are made of sheets of carbon atoms with a cylindrical shape and generally consist of co-axially arranged 2 to 20 cylinders「Fig. 1-7(b)」. The interlayer spacing in MWNT ($d_{(002)}$ = 0.34 nm) is slightly larger than that in single crystal graphite ($d_{(002)}$ = 0.335 nm) [1.35]. This is attributed to a combination of tubule curvature and van der Waals force interactions between successive garphene layers. The second type of the nanotube is made up of just a single layer of carbon atoms. These nanotubes are called the single-walled nanotubes (SWNTs) and possess good uniformity in diameter about 1.2 nm「Fig. 1-7(a)」. They are close to fullerenes in size and have a single-layer cylinder extending from end to end [1.36-1.37].

Most experimentally observed CNTs are multi-walled structures with outer most shell diameters exceeding 10 nm. Since current conduction in a MWNT is known to be mostly confined to the outermost single-walled nanotube and since band gap of a SWCNT varies inversely with its diameter, MWNTs are metallic in nature. SWNTs can be either metallic or semiconducting depending on the way the roll-up of the graphene sheet occurs - an aspect termed as Chirality, and if all the roll-up types are realized with equal probability, 1/3 of the SWNTs end up being metallic and 2/3 semiconducting. The structure of a SWNT can be conceptualized by wrapping a one-atom-thick layer of graphite called graphene into a seamless cylinder. The way of the graphene sheet is wrapped is represented by a pair of indices (n,m) called the chiral vector. The integers n and m denote the number of unit vectors along two directions in the honeycomb crystal lattice of graphene. If m=0, the nanotubes are called "zigzag". If n=m, the nanotubes are called "armchair". Otherwise, they are called "chiral". Figure 1-8 depicts these structures of a SWNT [1.38] [1.39].

CNts have been attracting much attention for their unique physical and chemical properties such as high mechanical strength, chemical stability, high aspect ratio, super-therml conductivity, and electron emission properties [1.40] [1.41]. CNTs could be one of the strongest and stiffest materials known, in terms of tensile strength and elastic modulus respectively. This strength results from the covalent sp^2 bonds formed between the individual carbon atoms. The highest tensile strength an individual multi-walled carbon nanotube has been tested to be is 63 GPa [1.42]. Under excessive tensile strain, the tubes will undergo plastic deformation, which means the deformation is permanent. This deformation begins at strains of approximately 5 % and can increase the maximum strain the tube undergoes before fracture by releasing strain energy. For the thermal conductivity of CNTs , it is predicted that carbon nanotubes will be able to transmit up to 6000 watts per meter per kelvin at room temperature; compare this to copper, a metal well-known for its good thermal conductivity, which only transmits 385 W/m/K. The temperature stability of carbon nanotubes is estimated to be up to 2800 degrees Celsius in vacuum and about 750 degrees Celsius in air [1.43].

1.3.2 Potential Applications of Carbon Nanotubes

Since Iijima reported the synthesis of CNTs by arc discharge process [1.33], many reports on the CNT synthesis were published in various deposition methods such as arc discharge, laser ablation [1.44], pyrolysis of hydrocarbon [1.45], and chemical vapor deposition (CVD) method [1.46-48]. CNTs have many exceptional properties that make them attractive for a variety of applications such as FEDs, microelectronics [1.49], hydrogen storage [1.50], scanning probes of atomic force microscopes (AFMs) [1.51], fuel-cell [1.52], and back-light units (BLUs) [1.53]. In particular, many reports have shown that CNTs have outstanding electrical field emission properties. Therefore, CNTs are attractive as cold cathode field emission sources, especially for applications requiring high current densities and lightweight packages.

According to Fowler-Nodiem theory, the electric field at the apex of a needle-shaped tip is enhanced by a factor $\beta = h/r$, where h is the height of the tip and r is the radius of curvature of the tip apex. The CNT is a stable form of carbon and can be synthesized by several techniques. They are typically made as threads about 10-100 nm in diameter with a high aspect ratio (>1000). These geometric properties, coupled with their high mechanical strength and chemical stability, make CNTs attractive as electron field emitters. Several groups have recently reported good electron field emission from CNTs [1.54-1.56].

In 1999, Samsung pronounced a 4.5-inch CNT-FED (Fig. 1-9(c)). A fully sealed field-emission display 4.5 in. in size has been fabricated using SWNTs-organic binders. They mixed a conglomeration of SWNTs into a paste with a nitrocellulose binder and squeezed the concoction through a 20-μm mesh onto a series of metal strips mounted on a glass plate (Fig. 1-9(b)). As the CNTs emerged from the mesh, they were forced into a vertical position. The metal strips with the CNTs sticking out of them served as the back of the display. The front of the display was a glass plate containing red, green, and blue phosphors and strips of a transparent indium-tin-oxide anode running from side to side. The glass plates were separated by spacers with the thickness of 200 μm (Fig. 1-9(a)). Once assembled, the edges were sealed and air was pumped out of the display. The fabricated displays were fully scalable at low temperature, below 415 °C, and the turn-on field of less than 1 V/μm and emission currents of 1.5 mA at 3 V/μm (current density, J =90 μA/cm^2) were achieved. Brightness of 1800 cd/m^2 at 3.7 V/μm with fluctuation of around 7 % was observed [1.57].

Samsung's 5-inch CNT-FED (Fig. 1-9(d)) could be the pioneer of a new generation of more energy efficient, high performance flat panel displays for portable computers. The CNTs appear to be durable enough to provide the 10000 hour lifetime considered being a minimum for an electronic product. The panel consumes just half the power of an LCD to generate an equivalent level of screen brightness. They could also be cheaper than LCDs or other types of FEDs being developed. Until now, at last five major Japanese electronic manufactures are working on this technology.

1.4 Thesis Organization

In chapter 1, the overview of vacuum microelectronics, basic principles of field emission theory and applications of carbon nanotubes are described.

In chapter 2, we utilize the Ti-Fe thin film whose weight percentage of Fe was 64 % as catalyst layer compared to pure Fe catalyst layer for CNTs growth. The improvements of reliability in field emission and growth rate at low temperature are included to realize the properties and mechanism of Fe-Ti codeposited catalyst thin film.

In chapter 3, we discussed the effects of growth time on the length of CNT pillars to understand the mechanism of Ti-Fe codeposited catalyst layer for CNTs growth. In the second part, we investigated the ratio of the interpillar spacing (R) to pillar height (H) to obtain the optimization of the field emission characteristics.

Finally, the summary and conclusions are provided in chapter 4.

Chapter 2

The Field Emission Characteristics of Carbon Nanotubes Synthesized from an Fe-Ti Codeposited Catalyst

2.1 Introduction

Carbon nanotubes have attracted a great deal of attention because of its amazing physical and chemical characteristics, such as high aspect ratio, low work function (5 eV), small tip radius of curvature, good chemical stability, strong mechanical strength, high conductivity, and electron emission properties [2.1][2.2]. Carbon nanotubes were thought to be very potential in many applications, such as microelectronics, scanning probes, fuel-cell, and FEDs. Among them, FEDs were one of the most realizable applications in near future. However, there were still reliability problems which can seriously reduce the lifetime of CNTs-based electron emitters. Generally, two kinds of reliability issues were observed: (1) abrupt decreases in emission current with increasing electric field and (2) a gradual degradation in emission current with high emission current density for a long period. Several reports indicated that poor adhesion between the CNTs and the substrates could cause an abrupt decrease in emission current resulting from a mechanical damage at high electric field [2.3]. Furthermore, high contact resistance between the CNTs and the substrates could result in a gradual degradation in emission current because of the Joule heat generated in high resistive contact regions [2.4]. Several methods have been proposed to improve the adhesion and/or the contact resistance between CNTs and substrates by post treatment such as spin-on-glass(SOG) coating, polymethyl methacrylate(PMMA) solutions coating, and Zinc power mixture [2.5][2.6]. Nevertheless, some of them might increase the complexity of processes or cause structural damages to CNTs.

Nowadays, several methods have been developed to synthesize CNTs, such as arc discharge [2.7], laser ablation [2.8], plasma-enhanced CVD [2.9], electron cyclotron resonance CVD [2.10], and thermal CVD [2.11]. Generally, the selective growth of CNTs by thermal CVD is simple, low cost, and well-developed method, is preferred to synthesize the CNTs in this thesis. However, the growth rate of CNTs at low temperatures is slow. It has been known that the morphology of catalyst nanoparticles after pretreatment is of critical importance of the CNTs growth, including the diameter, length, density. Therefore, control of the surface morphology of the catalyst nanoparticle is an essential prior to the CNTs growth. According to Lindemann criterion, the melting point decreases as the catalyst particles sizes reduced as the Fig. 2-1 [2.12]. And the nano-sized catalyst particles are more active compared with bulk catalyst metals due to surface effect [2.13]. The melting temperature of nanoparticles was based on size-dependent cohesive energy by considering the surface effects. The melting temperature of nanoparticles (T_{mp}) is linear to the reciprocal of the crystal size, i.e., $T_{mp}= T_{mb} (1-C/D)$, where T_{mb} is the melting temperature of the corresponding bulk materials, D is the crystal size and C is a material constant. Apparently, the proper determination of D is key issue. The smaller catalyst nanoparticles with the lower melting temperatures could be utilized to the CNTs growth at low temperatures in thermal CVD to increase growth rates.

With the novel method, we utilized the Ti-Fe thin film whose weight percentage of Fe was 64% as catalyst layer to promote the adhesion between the CNTs and the substrate for reliability improvement of CNTs, and to increase CNT growth rates at low temperatures by using thermal CVD. In addition, the field emission characteristics and the growth mechanism of CNTs by using the Fe-Ti codeposited catalyst were realized.

2.2 Motivation

For commercialization of FED, the reliability of CNT-based FED is an important issue. The degradation of field emission resulted from that the CNTs were pulled out of the substrate after field emission measurement owing to weak adhesion of CNTs to the substrate. The effects of the various post-treatments, such as thermal and mechanical treatments, on the field emission characteristics of CNT films for improving the reliability of field emission were reported. However, these methods not only complicate processes but also damage CNTs. They still can not resolve the issue of reliability effectively. Therefore, a new method for this issue is needed. For CNT growth, the Ti thin film was usually deposited on the substrate as the adhesion layer between the catalyst layer and the substrate. The Fe, Co, and Ni were used to be the catalyst for CNT growth. In this chapter, we codeposited Ti and Fe thin film whose weight percentages of Fe was 64 % as a proposed catalyst layer for CNT growth, and expected to enhance the adhesion between the CNTs and the substrate to improve reliability of CNTs. In addition, we did the AFM analysis for the Fe-Ti codeposited nanoparticles after H_2 pretreatment at 700 ℃ for more understanding the mechanism of the novel method. From the AFM image (Figure 2-2)[2.14], the nanoparticles of the proposed sample are more uniform and smaller than those of the conventional one whose catalyst layer was pure Fe thin film. Accordingly, we applied the novel method to CNTs growth at low temperature for the understanding the properties and mechanism of the Ti-Fe codeposited catalyst.

2.3 Experimental Procedures

An array of 5×5 squares was defined on the photoresist-coated N-type silicon wafers by lithography for selectively grown CNTs. The squares in array had the dimension of 100×100 μm^2 with 100-μm inter-space. Subsequently, a 50-nm-thick Ti was deposited by the dual electron-gun evaporation system as a buffer layer to improve adhesion between the catalyst and the substrates, and to avoid silicon carbide formation. After that, two different methods, conventional and proposed ones, were utilized to prepare the catalyst of CNTs. For the conventional samples, a 5-nm-thick Fe layer was also deposited by the dual electron-gun evaporation system as the catalyst of CNTs. On the other hand, Fe co-deposited with Ti was utilized as the catalyst of CNTs for the proposed samples. The weight percentage of Fe in the co-deposited layer for the proposed samples was about 64 % with constant quantity of Fe as compared with the conventional ones. (The ratio of specific gravity for Fe to Ti is 7.8/4.5.) After deposition, photoresist with Ti buffer layer and catalyst was removed by the lift-off process in acetone for both specimens. The experimental procedures for CNTs synthesis was shown as Fig. 2-3. Then, both of them were loaded into the thermal CVD to grow CNTs.

For the reliability study, the conventional and proposed samples were pretreated at 700 °C in H_2 and N_2 (400/600 sccm) ambient for 5 min and then grew CNTs at 700 °C with ethylene C_2H_4, H_2, and N_2 (5/100/500 sccm) for 15 min. On the other hand, the conventional and proposed samples were pretreated at 550 °C in H_2 and N_2 (200/500 sccm) ambient for 12 min and then grew CNTs at 550 °C with C_2H_4 and N_2 (70/500 sccm) for 15 min for the investigation of CNT growth at low temperatures.

After the synthesis of CNTs, the samples were analyzed with scanning electron microscopy (SEM, Hitachi S-4700) to observe the density and the morphology of CNTs. A dual beam (focused ion beam and electron beam) system was performed to discover the root of CNTs. The wall structure and crystallinity of CNTs were determined by high-resolution transmission electron microscopy (HRTEM) and the components of nanoparticles were analyzed by energy dispersive spectroscopy (EDS). A Raman spectrum was performed to offer the information about the crystallization of CNTs. The catalyst nanoparticles after pretreatment were analyzed by atomic force microscopy (AFM).The field emission properties of CNTs were characterized by a high–vaccum measurement environment with a base pressure of 5×10^{-6} Torr. Cathode contact was made directly on the wafer. A glass plate coated with indium-tin-oxide (ITO) was positioned 150 um above the tip of CNTs as an anode. All cables were shielded except for the ground return path to the power source. The emission current densities of CNTs were measured as a function of applied electron field, using Keithley 237 high voltage units as DC source and Keithley 238 high current units as ground source. The measurement was auto-controlled by the computer with IEEE 488 interface. The schematic experimental flow chart was shown in Fig. 2-4.

2.4 Results and Discussion

2.4.1 The Reliability Improvements of Carbon Nanotubes for Field Emission Applications

The SEM micrographs of the CNTs in the conventional and the proposed samples were shown in Figs. 2-5(a) and 2-5(b) correspondingly. The roots of the CNTs for the proposed samples exhibited a little inserted (indicated by an arrow in Fig. 2-5(a)) but those for the conventional ones were only terminated on the surface (indicated by an arrow in Fig. 2-6(b)). The transparent phenomenon implied a better conductive region around the roots. The inset of Fig. 2-5(b) displayed a SEM image of the proposed samples cleaved across the patterned region where a CNT with part of it plunged into the co-deposited metal layer was observed on the cleaved edge (marked by a circle). Therefore, the larger contact area and stronger adhesion for the proposed sample were depicted. The emission currents of both specimens were measured from 0 to 7.7 V/μm at 5×10^{-6} torr and the curves of emission current density versus electric field (J-E curve) were shown in Fig. 2-6. For the conventional samples, an abrupt decrease of emission current in the first measurement was indicated by an arrow in Fig. 2-6(a). The decrease in emission current did not recover in the subsequently measurements and the curves of the next 4 measurements were almost the same. It can be attributed to that part of the CNTs with poor adhesion were pulled off at high electric field during the first measurement and the remained CNTs with sufficient adhesion can sustain the force induced from electric field to provide smooth curves without abrupt decrease. On the other hand, for the proposed specimens, the curve of the first measurement was very close to the next 4 curves and no obvious abrupt current drop was observed as shown in Fig. 2-6(b). It resulted from that the enlarged contact area of the partially immersed structure of CNTs can provide sufficient adhesion to overcome the electric-field-induced force during measurements. Figs. 2-7(a) and 2-7(b) displayed the emission current density versus time for both the conventional and the proposed specimens tested at 7.7 V/μm for 3,600 sec. The emission current density of the conventional samples reduced from 60 mA/cm^2 to 20 mA/cm^2 after 700 sec and to 10 mA/cm^2 after 2,500 sec. However, the proposed samples exhibited a relative stable emission current density with 30 mA/cm^2 for 3,600 sec. Fig. 2-7(c) was the plot of the emission current density versus time for the conventional samples at 6.25 V/μm for 3,600 sec. The current density in the initial was about 30 mA/cm^2 as the same as the proposed samples at 7.7 V/μm, but unstable and reduced to 10 mA/cm^2 after 500 sec. It might be attributed to that the partially immersed structure with larger contact area can suppress the contact resistance and reduce the Joule heat generated in high resistive contact regions and prevent the CNTs from heat induced damages. For the first 400 sec in the Fig. 2-7(c), the current density was a little increasing because of the thermal emission. Fig. 2-8 showed the cross-sectional views of SEM for both samples before and after the stress for reliability analysis. Obviously, part of the CNTs in the conventional specimens disappeared after the time stress but the CNTs in the proposed ones had almost no change. It also manifested that the proposed samples with a partially immersed structure can prevent the CNTs from physical damages and improved the reliability of emitters.

For the CNTs formation mechanism has been proposed as the following steps: (i) carbon source gas decomposition at the surface of the catalyst nanoparticles; (ii) formation of surface carbide in the reaction zone; (iii) carbon diffusion into the nanoparticle volume; (iv) carbon release, after some oversaturation at the catalyst nanoparticle.

In order to realize the growing process of CNTs for the proposed and conventional samples with respect to Ti-Fe codeposited thin film and pure Fe one as catalyst layer. The two mechanisms were put forward in this section. According to the calculated surface energy for period elements diagram, the surface energy of Fe was higher than Ti as shown in Fig. 2-10 [2.15]. As a result, for the conventional specimens, the ultra-thin Fe catalyst would tend to melt and agglomerate into nanoparticles during pretreatment due to different surface energy from the Ti buffer layer. And the nanoparticles were only laid on the surface of Ti buffer layer. In contrast, for the proposed ones, the co-deposited Ti film would merge with the underneath Ti buffer layer and the Fe atoms simultaneously nucleated to form nanoparticles during pretreatment. So the nanoparticles in the proposed samples were partially immersed in the Ti metal. Accordingly, the synthesized CNTs for the conventional samples were only terminated on the surface of Ti metal but the CNTs for the proposed ones were partially immersed in the Ti metal. The schematic plots to depict such mechanisms for these two specimens were illustrated in Figs. 2-10(a) and 2-10(b). Therefore, this amazing structure of proposed sample provided better adhesion and lower contact resistance between the CNTs and the substrates. It could prevent the CNTs from heat induced destruction to improve the reliability of CNTs for the application as electron emitters.

2.4.2 The Improvements of Carbon Nanotube Growth Rate at Low Temperatures

The morphological images of CNTs taken by SEM were displayed in Fig. 2-11. From the comparison between the images of Fig. 2-11(a) and 2-11(b), the CNTs in the proposal samples exhibited a much longer length as compared with those in the conventional ones. The length of conventional samples was about 437 nm, but that of the proposed ones was about 2.13μm. It might be attributed to the suppression of coalescence of the Fe nanoparticles in the Fe-Ti codeposited film during the CNTs growth. It was remarkably observed by the SEM images of Fig. 2-12. Most of the catalytic particles in the proposal samples as Fig. 2-12(b) were smaller than those in the conventional ones as Fig. 2-12(a). For the conventional samples, the range of the catalyst particle size was from 30 nm to 170 nm, and the average diameter of them was 97.4 nm. For the proposed samples, the range of the catalyst particle size was from 50 nm to 100 nm, and the average diameter of them was 81.1 nm. It has been known that the smaller size of the catalyst nanoparticle would be sufficient for carbon diffusion and supersaturation of carbon atoms in the catalyst nanoparticle due to shorter volume diffusion path length. In addition, the cap lift-off to occur and the growth of the CNTs to start, the nanoparticles must have sufficiently great curvature (i.e., it must be small enough) so that the graphene layers of the cap are sufficiently strained so that cap liftoff, and addition of carbon in tubular form, is energetically favorable. In other words, CNTs nucleation and growth will only occur if the catalyst nanoparticles do not exceed a certain maximum size [2.16]. Therefore, the higher growth rate was exhibited in the proposal sample. As a result, the longer length of CNTs was obtained in the proposal one.

In addition, the less length variation of CNTs was also shown in Fig. 2-11(b) than those in Fig. 2-11(a). It might be due to more uniform catalytic particles in the proposal samples as Fig. 2-13(b) than those in the conventional ones as Fig. 2-13(a). The morphology of the catalytic particles weas shown in the cross section of the AFM images (Fig. 2-13).The Raman spectrum of the CNTs for the conventional and the proposed samples showed similar results, as shown in Fig. 2-14. It means that there was no obvious difference of the crystallinity in the CNTs for these two samples. It also implied that the Ti co-deposited with Fe might not participate in the growth of CNTs for the proposed samples. The TEM images were shown in

Fig. 2-15(a) and Fig. 2-15(b) with respect to the conventional and proposed samples. The layer-by-layer structure of graphite could be clearly observed. They could also demonstrate that the CNT in this TEM image was a multi-wall structure. Moreover, the composition of the catalytic nanoparticle was analyzed by EDS via the TEM instrument. The EDS spectrum in Fig. 2-16 showed that only Fe, C, and Cu existed in the results of the EDS analysis. The peaks of Cu were from the Cu mesh which was used to hold CNTs in the TEM system. The peak of C was from the CNT and the peaks of Fe were from the catalytic nanoparticle enclosed in the CNT. No signal of Ti was detected which indicated that the Fe would not form the alloy with Ti in this process. From the images of TEM and the analysis of EDS, they implied that the Fe played a critical role in the growth of CNTs and Ti seemed not involve in the formation of CNTs by Ti-Fe alloy. The plots of current density versus electrical field for the both samples were shown in Fig. 2-17. The turn-on field was defined as the field with the current density of 10 μA/cm^2. For the conventional samples, the current density was much smaller than the proposed ones, and it was much less than 10 μA/cm^2 at 6.25 V/μm. On the other hand, the current density of the proposed samples was 3.36 mA/cm^2 at 6.25 V/μm, and the turn on field was 4.44 V/μm.

To explain the smaller and more uniform catalytic nanoparticles in the proposal samples, the formation schemes of the nanoparticles for the conventional samples and the proposed ones were plotted as Figs. 2-18. For the conventional samples, the Fe film directly transferred to nanoparticles at 550 ℃ and subsequently the coalescence of these nanoparticles proceeded due to the difference of surface energy between Fe and Ti, as shown in Fig. 2-18(a). The formation mechanism of catalytic nanoparticles might be that Fe atoms nucleated at 550 ℃ to form nanoparticles and the codeposited Ti atoms merged with the underlaid Ti buffer layer. Ti atoms in the proposed samples played a role to disperse the Fe nanoparticles. Owing to the existence of the codepsited Ti, it regarded and suppressed the coalescence of the Fe nanoparticles, as shown in Fig. 2-18(b). Hence, the CNTs in the proposal samples had more uniform distribution and higher growth rate at low temperature as compared with those in the conventional ones.

2.5 Summary

The CNTs grown from an Fe-Ti codeposited catalyst at 700 ℃ in thermal CVD exhibited a partially immersed structure with larger contact area to the Ti film as compared with those for the conventional ones. This amazing structure provided better adhesion and lower contact resistance between the CNTs and the substrates. With better adhesion, the abrupt decreases in emission current were suppressed remarkably and the characteristics of field emission could be stabilized to obtain smooth J-E curves. The proposed samples exhibited a relative stable emission current density with 30 mA/cm^2 at 7.7 V/μm for 3,600 sec. Furthermore, the reduction of contact resistance could diminish the generation of Joule heat to prevent the CNTs from heat induced destruction. By utilizing the Fe-Ti codeposited catalyst layer, the reliability of CNTs could be also improved for the application as electron emitters.

In addition, the proposed structure was utilized to growth CNTs at low temperatures of 550 ℃ in thermal CVD. The higher growth rate was exhibited in the proposal samples. The length of conventional samples was about 437 nm, but that of the proposed ones was about 2.13 μm. In the mean while, the less length variation of CNTs was also shown in the proposed samples than those in the conventional ones. It was due to smaller and more uniform catalytic particles in the proposal samples than those in the conventional ones. For field emission measurement, the current density of the proposed samples was much less than 10 μA/cm^2 at 6.25 V/μm. The current density of the proposed samples was as high as 3.36 mA/cm^2 at 6.25 V/um, and the turn-on field was 4.44 V/μm.

Chapter 3

The Field Emission Characteristics of Carbon Nanotube Pillars Synthesized from an Fe-Ti Codeposited Catalyst

3.1 Introduction

Carbon nanotubes(CNTs), a self-organized nanoscale structure, have a variety of applications such as field emission displays (FEDs) [3.1], X-raytubes [3.2], flat lamp [3.3] and backlight units (BLU) for liquid crystal displays (LCDs) [3.4], because of their excellent field emission characteristics. Especially, BLU has been remarkably investigated for a recent few years because of development of large area LCD TV. The schematic of a typical BLU is shown in Fig. 3-1(a)[3.5] including light source, reflector, light guide, diffuser, and brightness enhancement film (BEF). The light source can be an incandescent light bulb, light emitting diode (LEDs), cold cathode fluorescent lamp (CCFL), hot cathode fluorescent lamps (HCFL). All the backlights employ a diffuser and a BEF. The diffuser posited between the light source and the display panel is used to scatter the light for display uniformity. The BEF is used to enhance display brightness. The cost structure of materials for TFT-LCDs is described as Fig. 3-1(b). As Fig. 3-1(b) shows, the cost of BLU module for 15 inch monitor is 23 %, and the cost for 30 inch LCD TV monitor is as high as 38 %. They imply that the reduction of BLU cost is an important issue. CNTs are thus utilized to BLU not only for the reduction of cost but also for less power consumption, optical films needless, no toxic chemicals, and super color performance [3.6].

Many synthesis methods for CNTs have been investigated and reported since the discovery of CNTs. It is indispensable to lower the turn on field (which is defined as the electronic field to reach current density with 10 $\mu A/cm^2$) and threshold field (which is defined as the electronic field to reach current density with 10 mA/cm^2) to achieve practically applicable field emission emitters that operate with low power consumption. For CNTs-FEA, the high density of CNTs can provide a great deal of field emission sites which can raise the emission current density (due to the increase of the emission area, α) but the density of CNTs will affect the field enhancement factor (β) which is also strongly relative to the emission properties of CNTs. For CNTs with high density, the screening effects reduce the field enhancement factor (β), therefore, suppress the field emission current density, as shown in Figure 3-2 [3.7]. Obviously, it is important to obtain an optimized density of CNTs to improve the field emission properties, such as turn-on field, threshold field, and emission current density, as shown in Figure 3-3 [3.8]. Well control of density and surface morphology of CNTs are thus required for applications in the near future. To effectively control the density of CNTs and surface morphology, the CNT pillars have been investigated. According to the prediction of Nilsson *et al.*[3.7], the field emission will become maximum when the interpillar distance is about two times the height of the pillar [3.9].

Uniform and small catalyst nanopartilces after pretreatment are known to be the key for growing highly aligned CNTs. It is attributed to the lasting van der Waals force since these uniform nanoparticles could lead to the grown CNTs with the equal growth rate. Therefore, the CNT pillars were easily synthesized from uniform and small catalyst nanoparticles after pretreatment.

3.2 Motivation

The pillar-like CNTs are well to control the density and the morphology of CNTs. It has been reported that the screening effect of CNTs can be effectively reduced by the density control of the pillars. Therefore, the field emission characteristics can be enhanced from the compromise of the screening effect and emission sites. In Chapter 2, we utilized an Fe-Ti thin film whose weight percentage of Fe was 64 % as a catalyst layer, the nanoparticles after pretreatment were more uniform and smaller. As a result, it could be desirable for as many CNTs per unit surface area as possible to grow with the equal growth rate. The growing CNTs can support each other due to the lasting van der Waals force to obtain the highly aligned CNTs. Therefore, the CNT pillars could be easily synthesized by the proposed method. By using CNT pillars as light source for BLUs in TFT-LCDs, high brightness and excellent uniformity could be achieved. As a result, the diffuser and BEF could not be needed for BLUs in TFT-LCDs. Therefore, the CNT pillars could be potentially applied in the BLUs for TFT-LCDs to reduce the material cost.

In this chapter, the pillar arrays of aligned CNTs were fabricated with Fe-Ti codeposited catalyst to form a device with area of 0.02 cm^2. By adjusting the ratio of the interpillar spacing (R) to pillar height (H) with fixed diameter, an optimized field emission was obtained. In the mean while, the mechanism of Fe-Ti codeposited catalyst for CNTs growth was more complete via the study for the effects of growth time on the length of CNT pillars.

3.3 Experimental Procedures

Here, we also used two different catalyst thin films, conventional and proposed ones, (as the same as Chapter2). For the conventional samples, a 5-nm-thick Fe layer was deposited as the catalyst of CNTs. On the other hand, Fe co-deposited with Ti was utilized as the catalyst of CNTs for the proposed samples. The weight percentage of Fe in the co-deposited layer for the proposed samples was about 64 % with constant quantity of Fe as compared with the conventional ones. The formation of the patterns was as shown in Fig. 3-4, A photoresist was spin-coated on an N-type Si (100) substrate and the emitting sites were defined by the mask which has several 6-μm-diameter circles with interspacing of 12, 15, 20, 25, 30, and 35 μm by photolithography, as shown in Fig. 3-4(a). Afterward, a thin Ti film (50 nm) was deposited on the Si substrate as the buffer layer which had excellent adhesion to the Si substrate, as shown in Fig. 3-4(b). A catalytic film was deposited directly on the photoresist-patterned Si substrate by dual E-gun evaporation system, as shown in Fig. 3-4(c). Then the patterns were formed after removing the photoresist by lift-off method as depicted in Fig. 3-4(d). Finally, the CNT pillars were grown selectively by thermal CVD system, as shown in Fig. 3-4(e).

The samples were pretreated at 700 ℃ in N_2 and H_2 (500/100 sccm) for 8 min, and then grew CNTs at 700 ℃ with C_2H_4, N_2, and H_2 (20/500/100 sccm) for different time from 8 to 120 min. The growth condition of CNTs in the thermal CVD system was shown in Fig. 3-5.

After the synthesis of CNTs, the samples were analyzed with scanning electron microscopy (SEM, Hitachi S-4700) to observe the density and the morphology of CNTs. The catalyst nanoparticles after pretreatment were analyzed by atomic force microscopy (AFM). The field emission properties of CNTs were characterized by a high–vaccum measurement environment with a base pressure of 5×10^{-6} Torr. Cathode contact was made directly on the wafer. A glass plate coated with indium-tin-oxide (ITO) was positioned 150 um above the tip of CNTs as an anode. All cables were shielded except for the ground return path to the power source. The emission current densities of CNTs were measured as a function of applied electron field, using Keithley 237 high voltage units as DC source and Keithley 238 high current units as ground source. The measurement was auto-controlled by the computer with IEEE 488 interface.

3.4 Results and Discussion

3.4.1 The Effect of Growth Time on the Length of Carbon Nanotube Pillars

The rate of growth under given reaction conditions is an important issue concerning CNTs growth: how long can CNTs be grown, and how fast do they grow? For the investigation of the issue and the mechanism of the CNTs growth with conventional and proposed catalyst films, we measured lengths of the CNT pillars as a function of growth time. The cross-section views of the CNT pillars for the conventional and proposed samples with different growth time were taken by scanning electron microscope and displayed in Fig. 3-6 and Fig. 3-7, correspondingly. The lengths of the CNT pillars synthesized from the conventional method for different time were about 5.6 μm for 8 min, 15.7 μm for 15 min, 22.4 μm for 30 min, 47 μm for 60 min, and 69.8 μm for 120 min. On the other hand, the lengths of the CNT pillars grown from the proposed method for different time were about 4.48 μm for 8 min, 12 μm for 15 min, 19.4 μm for 30 min, 52.2 μm for 60 min, and 118 μm for 120 min. The relationship between the length and the growth time for both samples were plotted in Fig. 3-8. As shown in Fig. 3-8, the growth rate of CNT pillars in conventional samples seemed to saturate when the growth time was over 60 min and the growth rate of CNT pillars in proposed samples sustained almost a constant in 120 min. For the conventional sample, the growth rate of the CNT pillars was about 0.78 μm/min in the first 60 min, and appeared to decrease to 0.39 μm/min in the last 60 min. For the proposed samples, the length of CNT pillar increased linearly with growth rate of 0.98 μm/min.

The observation of CNT pillars for the conventional samples revealed growth and saturation steps. It could be possible that the inactivation of the metal catalyst nanoparticles included overcoating with carbon or conversion of the metal into a metal carbide or other non-catalytic form [3.10]. Slowing or complete stoppage of nanotube growth with increasing growth time has been attributed to catalyst deactivation, overcoating, or coalescence.

From Fig. 3-8, the growth rate of CNT pillars for the conventional samples was slightly faster than that for the proposed ones in the initial few minutes, about first 15 min. It could be explained by the possible mechanism as shown in Fig. 3-9. The conventional samples had more carbonaceous diffusion path due to more nanoparticle surfaces exposed to the reaction gases in the first few minutes. In the contrast, the proposed samples had a lot of nanoparticles which were merged in the Ti thin. There were less carbonaceous diffusion path for the proposed samples. As a result, the conventional samples had higher growth rate than the proposed ones in the initial few minutes. After that, the catalyst nanoparticles were covered by the CNTs no matter the nanoparticle was in the bottom or top of CNTs. The CNTs growth rate was dominated by the carbonaceous volume diffusion but the surface diffusion. The smaller nanoparticles had shorter volume diffusion path, and resulted in higher growth rate of CNTs pillars. The proposed samples had smaller nanoparticles, as shown in Fig. 3-10. Therefore, the growth rate of CNT pillars for the proposed samples increased, and was higher than that for the conventional ones.

For the proposed samples, the grown CNTs were denser and aligned, as shown in Fig. 3-11. It could be due to that the proposed samples had smaller nanoparticles. It confirmed our previous opinion which was the grown CNTs per unit surface area with the equal growth rate by using an Fe-Ti catalyst layer for CNT pillars synthesis.

3.4.2 The Optimization of Spacing to Height Ratio for Carbon Nanotube Pillars

The fabricated CNT pillars in the proposed samples for growth time of 15 min were shown by SEM images in Fig. 3-12. The pillars were aligned perpendicular to the substrate, and their height (H) was about 12 μm. There were six different spacing (R) between pillars of 12, 15, 20, 25, 30, and 35 μm. The R-to-H ratio (R/H) was 1, 1.25, 1.67, 2.08, 2.5, and 2.92, respectively. Each pillar can be regarded as an individual emitter since the electron filed emission can be neglected inside the pillar due to the screening effects. The emitter device was diode structure with the area of 0.02 cm^2. The emission current versus voltage (I-V plot) of the pillar arrays was shown in Fig. 3-13(a) with the spacing 150 um between the anode and the cathode. It showed that the emission current was as high as several million Ampere at the operating voltage. The corresponding Fowler-Nordheim (FN) plots were shown in Fig. 3-13(b) and the linearity of the F-N plot confirmed the field emission phenomenon.

The emission current of device was divided by the device area of 0.02 cm^2 to get turn-on field and threshold field of one device and the results were shown in Table 3-1. The turn-on field (E_{on}) and the threshold field (E_{th}) were defined as the field for current density of 10 μA/cm^2 and for 10 mA/cm^2, respectively. The curve of turn-on field versus R was plotted in Fig. 3-14 and showed that the turn-on field remain almost a constant for R/H ratio larger than 2.5. As the simulation results shown in the work of Nilsson, et al., the screening effect is greatly reduced when the interspacing of emitters is two times of its height. The local enhancement factor will not be improved obviously even the interspacing between emitters was increase greatly. It also hints that the turn-on field will not be decreased remarkably with increasing the interpillar spacing more.

The reliability of the pillar array was determined by a stress test at voltage with 800 V (5.33 V/μm) for 1 hour. The current versus time plot was shown in Fig. 3-15(a). The coefficient of standard variation (CV) and the mean current density (J_{mean}) were shown in Table 3-2. The CV was defined as the standard variation to the mean value of current. The lower CV means higher reliability of field emission for pillar-like CNTs. Table 3-2 revealed that the lowest CV (20.59 %) and the highest J_{mean} (18.94 mA/cm^2) occurred in R of 30 μm. The J_{mean} versus R was plotted in Fig. 3-15(b). As shown in this figure, the emission current increased rapidly with enlarging R from 12 μm to 25 μm and then increased slowly even a slightly decreased with larger R. The increasing of emission current resulted from the suppression of screening effect by enlarging the R, however, the improvement in screening effect was getting unobvious and emission areas was also getting small that caused a trade-off for the total emission current of device. The trade-off between the suppression of screening effect and the reduction of emission sites leaded to an optimal R to obtain a maximum emission current density and here was 30 μm, about 2.5 times of the H, in our experiments.

The fluorescent images of field emission with R of 30 μm under the stress test were shown in Fig. 3-16. It obviously observed that the CNT pillars had high brightness even through a period time of 1 hr, as shown in Fig. 3-16(b). In addition, the field emission fluorescent images of the CNT pillars with H of 12 μm and R of 30 μm and the full plane CNTs with emission area of 0.01 cm^2 for different voltages were shown in Fig. 3-17 and Fig. 3-18. The brightness was enhanced with the increasing voltage form 400 V to 800 V. The brightness of the CNT pillars was much higher than that of the full plane CNTs under the equal voltage. The field emission current density versus time of CNT pillar and that of full plane CNTs for different voltages were plotted in Fig. 3-19(a) and 3-19(b), respectively. They obviously showed the current density of the CNT pillar was much higher than that of the full plane CNTs under the equal voltage. The plot of the mean current density versus field under field emission stress test for 120 sec for the CNT pillars and the full plane CNTs was shown in Fig. 3-20. The mean current density increased by the increasing field.

The fabricated CNT pillars in the proposed samples for growth time of 8 min were shown by SEM images in Fig. 3-21. The height (H) of the CNT pillars was about 6.5 μm. There were also six different spacing (R) between pillars of 12, 15, 20, 25, 30, and 35 μm. The R-to-H ratio (R/H) was 1.84, 2.31, 3.07, 3.85, 4.62, and 5.38, respectively. The emitter device was also a diode structure with the area of 0.02 cm^2. The emission current versus voltage (I-V plot) of the pillar arrays was shown in Fig. 3-22(a) with the spacing 150 um between the anode and the cathode. It showed that the emission current was several micron Ampere at the operating voltage. The corresponding Fowler-Nordheim (FN) plots were shown in Fig. 3-22(b). The results of the field emission were shown in Table 3-3. An optimal R to obtain a maximum emission current density and here was 15 μm, about 2.31 times of the H (6.5 μm) for the growth time of 8 min due to the trade-off between the suppression of screening effect and the reduction of emission sites. The curve of maximum field emission current density versus interpillar spacing for the CNT pillars was plotted in Fig. 3-23.

3.5 Summary

The CNT pillars synthesized by using the proposed method exhibited a linear growth rate of 0.98 μm/min in 2 hours but the growth rate of the CNT pillars in the conventional samples tended to saturate at 0.39 μm/min after about 40 min. This phenomenon might be due to the smaller dimension of nanoparticles in the proposed samples could hold its activity at the same temperature better than those in the conventional samples. Although, the length of CNT pillars for the conventional sample was longer than those for the proposed ones due to more carbonaceous diffusion paths in the initial few minutes. Moreover, the CNTs in the proposed samples also showed a straighter morphology as compared with those in the conventional ones which might result from that the high density of nanoparticles in the proposed samples restricted the growth direction of the carbon nanotubes. It is helpful to form pillars with better uniformity in direction and then gain a more uniform emission current.

Additionally, we showed that the R/H played a crucial role for the field emission properties. The optimal interpillar spacing of 30 μm and 15μm were also found for the pillars with H of 12 μm and 8μm, respectively, to obtain a largest emission current density. They were also found that a trade-off between the suppression of screening effect and the reduction of emission area caused by decreasing the R was the main factor for the optimization of the R. The optimal R/H was about from 2.3 to 2.5. For the CNT pillars with growth time of 15 min, a low turn-on field of 1.01 V/μm was obtained for the CNT pillars with R of 30 μm (H=12μm). An excellent reliability for the CNT pillars was also shown in R/H of 2.5 at 800 V (5.33 V/μm) for 1 hour. The coefficient of current variation was as low as 20.59 %, and the mean current density was as high as 18.94 m A/cm^2. Besides, a very bright light emission was observed by applying the CNT pillars from 400 V (2.67 V/μm) to 800 V (5.33 V/μm). The

CNT pillars showed a wonderful potential for the application in FEDs or BLUs without adding extra expensive or complex processes.

Chapter 4

Summary and Conclusions

By using an Fe-Ti thin film whose weight percentages of Fe was 64 % as catalyst layer, the CNTs grown from an Fe-Ti codeposited catalyst at 700 ℃ in thermal CVD exhibited a partially immersed structure with larger contact area to the Ti film as compared with those from a pure Fe catalyst. This amazing structure provided better adhesion and lower contact resistance between the CNTs and the substrates. With better adhesion, the abrupt decreases in emission current were suppressed remarkably and the characteristics of field emission could be stabilized to obtain smooth J-E curves. The proposed samples exhibited a relative stable emission current density with 30 mA/cm^2 at 7.7 V/μm for 3,600 sec. In contrast, the emission current density of the conventional samples reduced from 60 mA/cm^2 to 20 mA/cm^2 after 700 sec and to 10 mA/cm^2 after 2,500 sec. Additionally, the higher CNT growth rate could be also achieved via Fe-Ti codeposited structure at 550 ℃ in thermal CVD as compared with those of the pure Fe catalyst. The less length variation of CNTs was also shown in the proposed samples than those in the conventional ones. It was due to smaller and more uniform catalytic particles after pretreatment in the proposal samples than those in the conventional ones. Besides, the Ti codeposited with Fe might not participate in the CNT growth for the proposed samples, and played a role to disperse the Fe nanoparticles and retard the coalescence of the nanoparticles after pretreatment.

With an Fe-Ti codeposited catalyst layer, the nanoparticles after pretreatment were more uniform, smaller, and denser. The CNT pillars were thus successfully synthesized using such a catalyst because of the grown CNTs per unit surface area with the almost equal growth rate. The growing CNTs could support one another with the lasting van der Waals force to obtain highly aligned CNTs. The CNT pillars synthesized by using the proposed method exhibited a linear growth rate of 0.98 μm/min in 2 hours but the growth rate of the CNT pillars in the conventional samples tended to saturate at 0.39 μm/min after about 40 min. This phenomenon might be due to the smaller dimension of nanoparticles could hold the activity during the CNT growth for the proposed samples. Although, the length of CNT pillars for the conventional sample was longer than those for the proposed ones due to more carbonaceous diffusion paths in the initial few minutes. Moreover, the CNTs in the proposed samples also showed a straighter morphology as compared with those in the conventional ones which might result from that the high density of nanoparticles in the proposed samples restricted the growth direction of the carbon nanotubes. It is helpful to form pillars with better uniformity in direction and then gain a more uniform emission current. In addition, we showed that the R/H played a crucial role for the field emission properties. An optimal interpillar spacing of 30 μm and 15μm were also found for the pillars with H of 12 μm and 8 μm, respectively, to obtain a largest emission current density. They were also found that a trade-off between the suppression of screening effect and the reduction of emission area caused by decreasing the R was the main factor for the optimization of the R. The optimal R/H was about from 2.3 to 2.5. For the CNT pillars with growth time of 15 min, a low turn-on field of 1.01 V/μm was obtained for the CNT pillars with R of 30 μm (H=12μm). An excellent reliability for the CNT pillars was also shown in R/H of 2.5 at 800 V (5.33 V/μm) for 1 hour. The coefficient of current variation was as low as 20.59 %, and the mean current density was as high as 18.94 m A/cm^2. Besides, a very bright light emission was observed by applying the CNT pillars from 400 V (2.67 V/μm) to 800 V (5.33 V/μm). The CNT pillars showed a wonderful potential for the application in FEDs or BLUs without adopting extra expensive or complex processes.

Table 1-1

Comparison between vacuum microelectronics and solid-state electronics.

Items	Solid State Microelectronics	Vacuum Microelectronics
Current Density	10^4 – 10^5 (A/cm^2)	similar
Turn-on Voltage	0.1 – 0.7 V	5 – 300 V
Structure	solid/solid interface	solid/vacuum interface
Electron Transport	in solid	in vacuum
Electron Velocity	3×10^7 (cm/sec)	3×10^{10} (cm/sec)
Flicker Noise	due to interface	due to emission
Thermal & Short Noise	comparable	comparable
Electron Energy	< 0.3 eV	a few to 1000 eV
Cut-off Frequency	< 20 GHz (Si) & 100 GHz (GaAs)	< 100 – 1000 GHz
Power	small – medium	medium – large
Radiation Hardness	poor	excellent
Temperature Effect	-30 – 50 °C	< 500 °C
Fabrication & Materials	well established (Si) & fairly well (GaAs)	not well established

Table 3-1

Field emission properties of CNTs with different spacing between pillars for the device area of 0.02 cm^2 (growth time of 15 min).

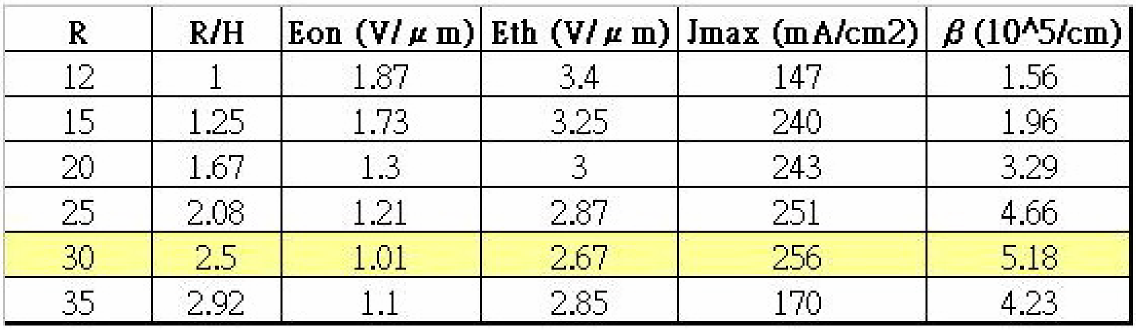

R	R/H	Eon (V/μm)	Eth (V/μm)	Jmax (mA/cm2)	β (10^5/cm)
12	1	1.87	3.4	147	1.56
15	1.25	1.73	3.25	240	1.96
20	1.67	1.3	3	243	3.29
25	2.08	1.21	2.87	251	4.66
30	2.5	1.01	2.67	256	5.18
35	2.92	1.1	2.85	170	4.23

Table 3-2

Field emission properties of CNTs with different spacing between pillars at 800V for hour.

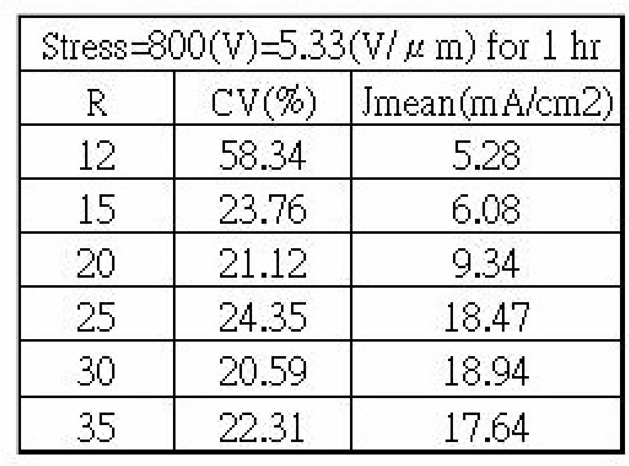

Stress=800(V)=5.33(V/μm) for 1 hr		
R	CV(%)	Jmean(mA/cm2)
12	58.34	5.28
15	23.76	6.08
20	21.12	9.34
25	24.35	18.47
30	20.59	18.94
35	22.31	17.64

Table 3-3

Field emission properties of CNTs with different spacing between pillars for the device area of 0.02 cm^2 (growth time of 8 min).

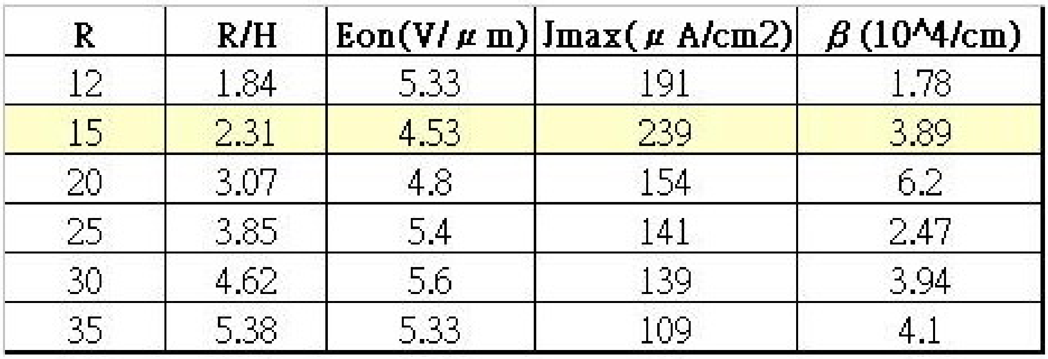

R	R/H	Eon(V/μm)	Jmax(μA/cm2)	β(10^4/cm)
12	1.84	5.33	191	1.78
15	2.31	4.53	239	3.89
20	3.07	4.8	154	6.2
25	3.85	5.4	141	2.47
30	4.62	5.6	139	3.94
35	5.38	5.33	109	4.1

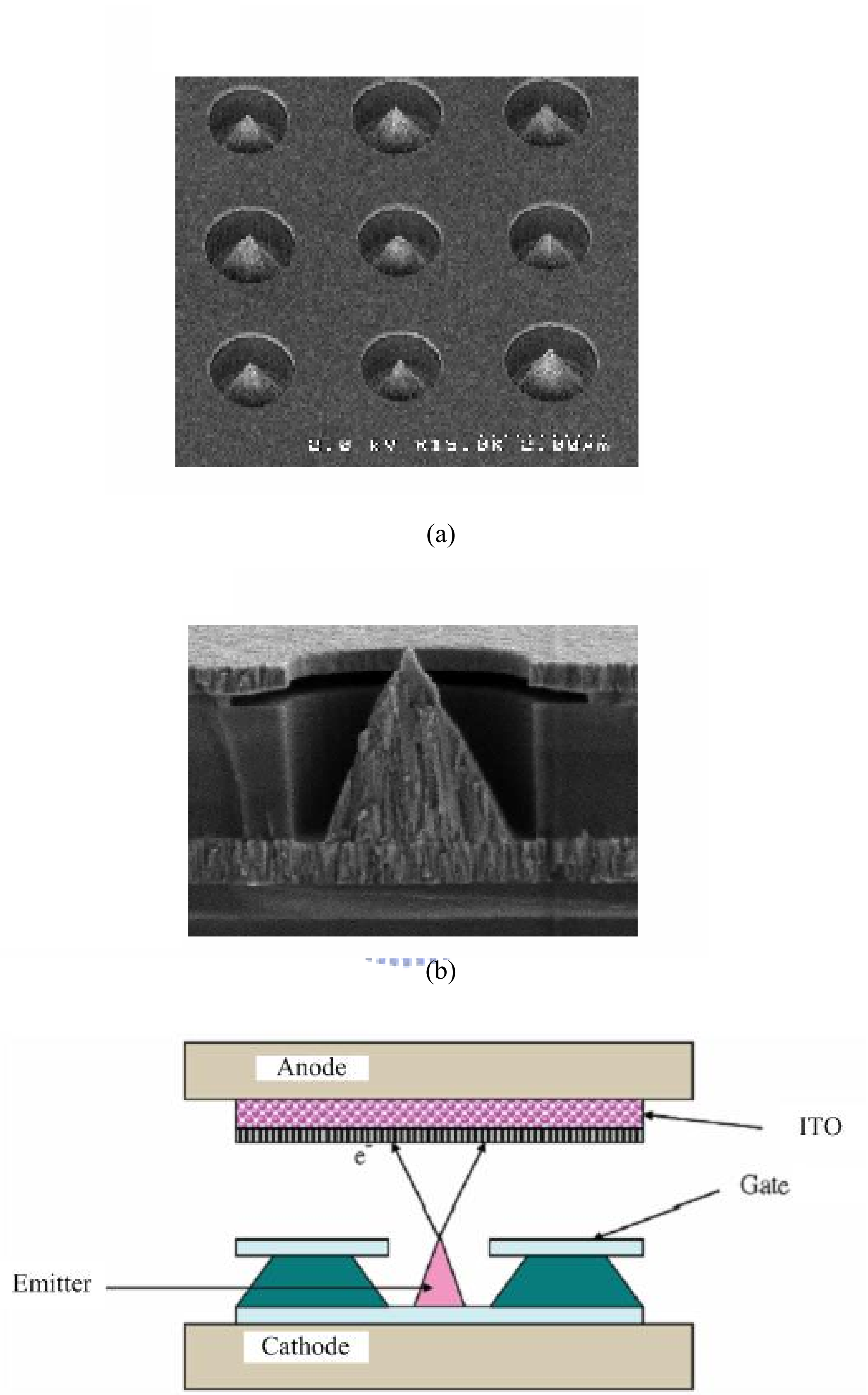

(a)

(b)

(c)

Figure 1-1 The SEM micrograph of (a) Spindt type triodes array, (b) Spindt type field emission triode, and (c) Emitting way of spindt type triode. [1.5]

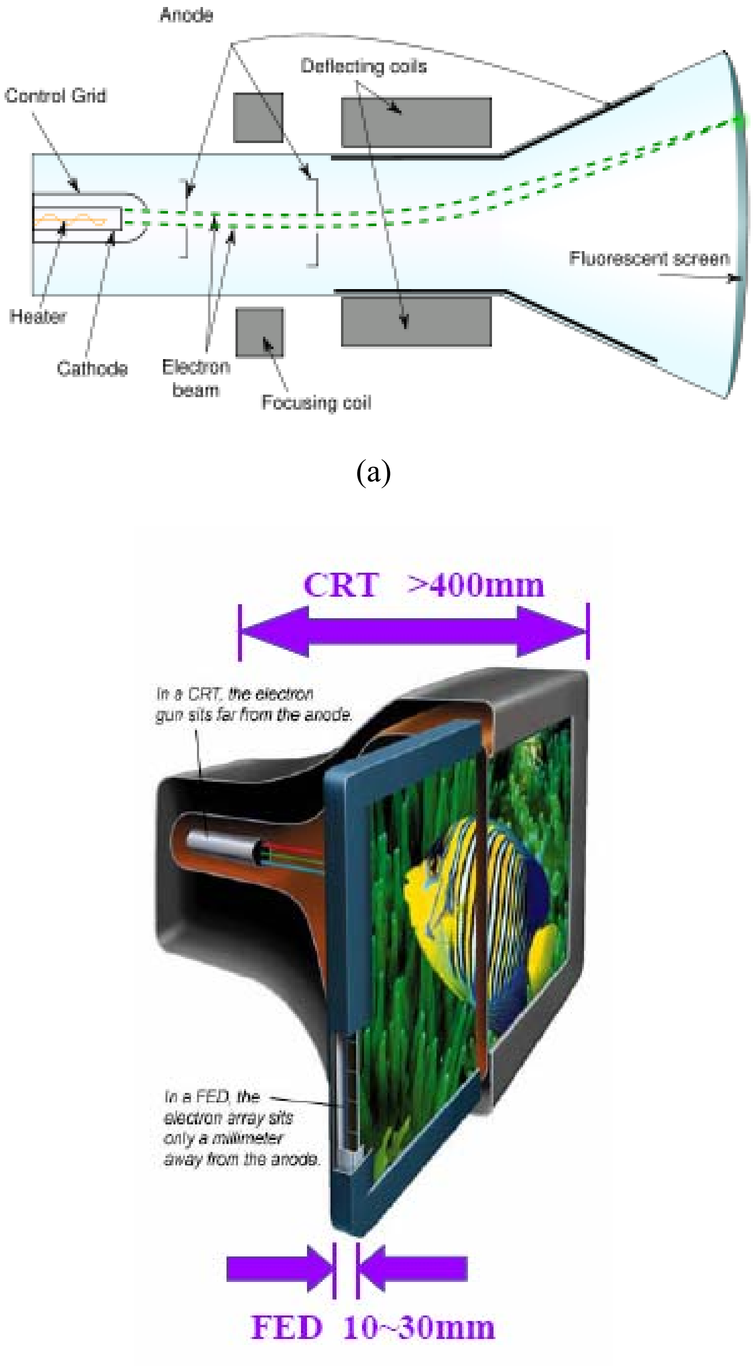

(a)

(b)

Figure 1-2 The schematic diagram of (a) conventional CRT and (b) comparison between CRT and FED. [1.23]

(a) (b)

(c) (d)

(e) (f)

Figure 1-3 The full color FED products: (a) Motorola 5.6" color FED based on Spindt-type , (b) Pixtech 5.6" color FED based on Spindt-type, (c) Futaba 7" color FED based on Spindt-type, (d) Sony/Candescent 13.2" color FED based on Spindt-type, (e) Samsung 32" under-gate CNT-FED, and (f) Canon-Toshiba 36" SED-TV.

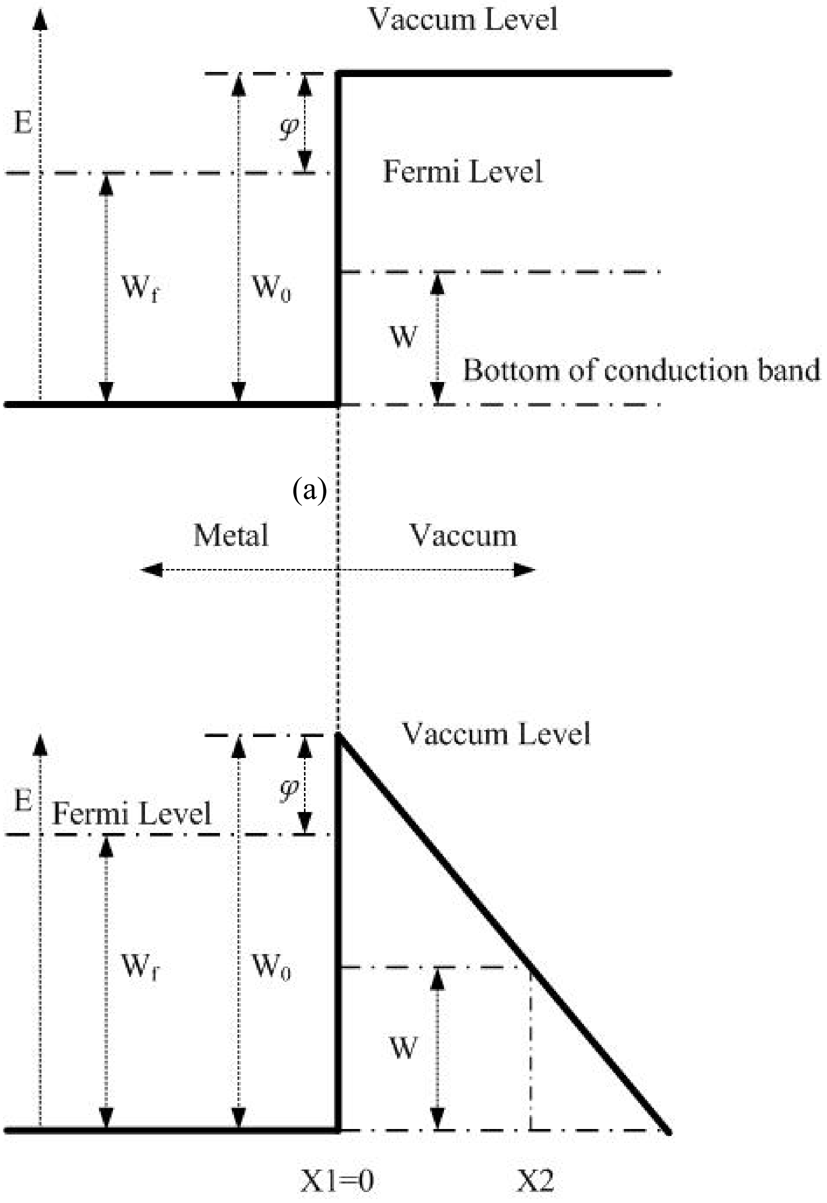

(a)

(b)

Figure 1-4 Energy diagrams of vacuum-metal boundary (a) without external electric field, and (b) with an external electric field.

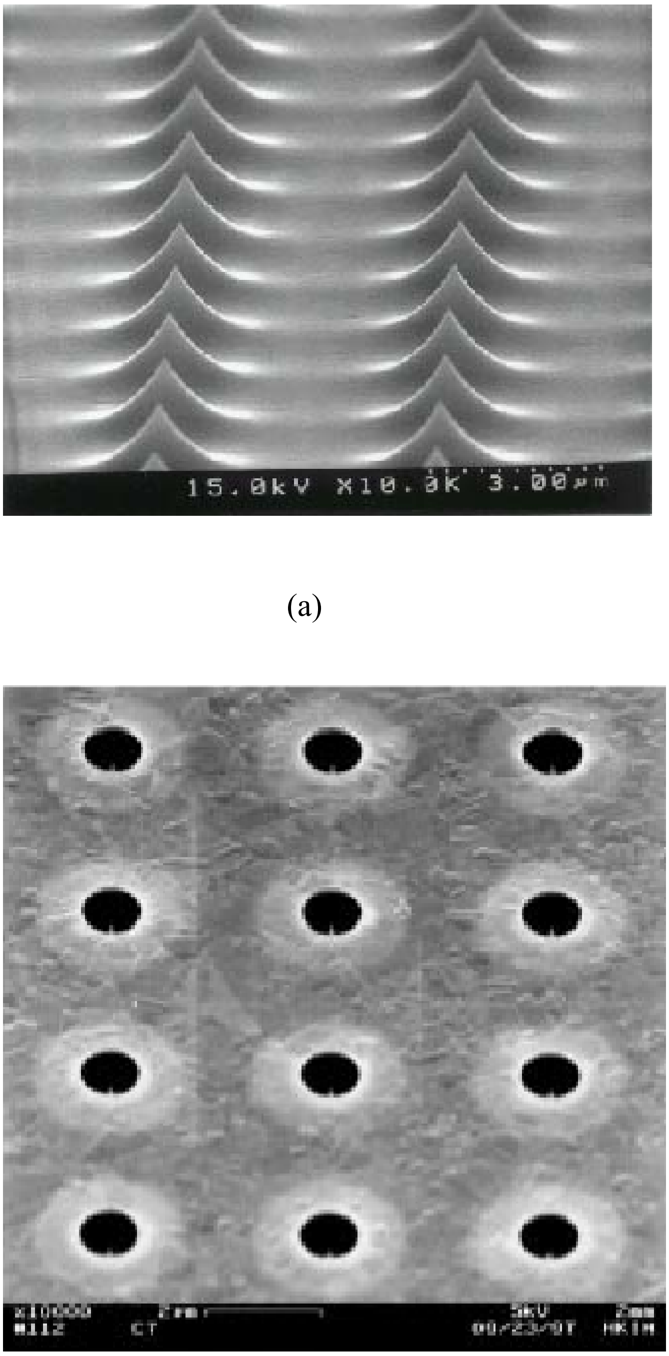

(a)

(b)

Figure 1-5 (a) Si tip formed by isotropic etching and (b) Si tip field emission triodes array formed by CMP [1.29] [1.30]

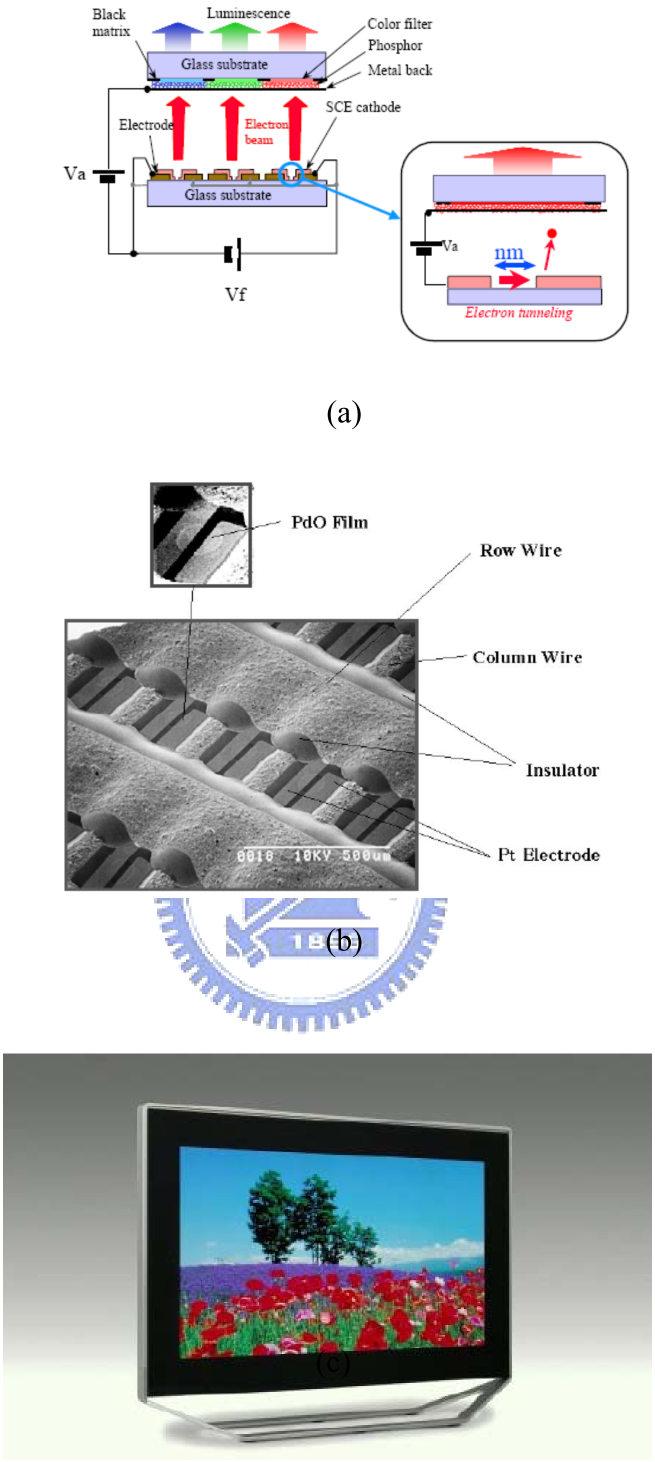

(a)

(b)

(c)

Figure 1-6 (a) The structure of SED, (b) SEM image of SCE cathode array, and (c) A 36-inch prototype of surface conduction electron emitter display. [1.31] [1.32]

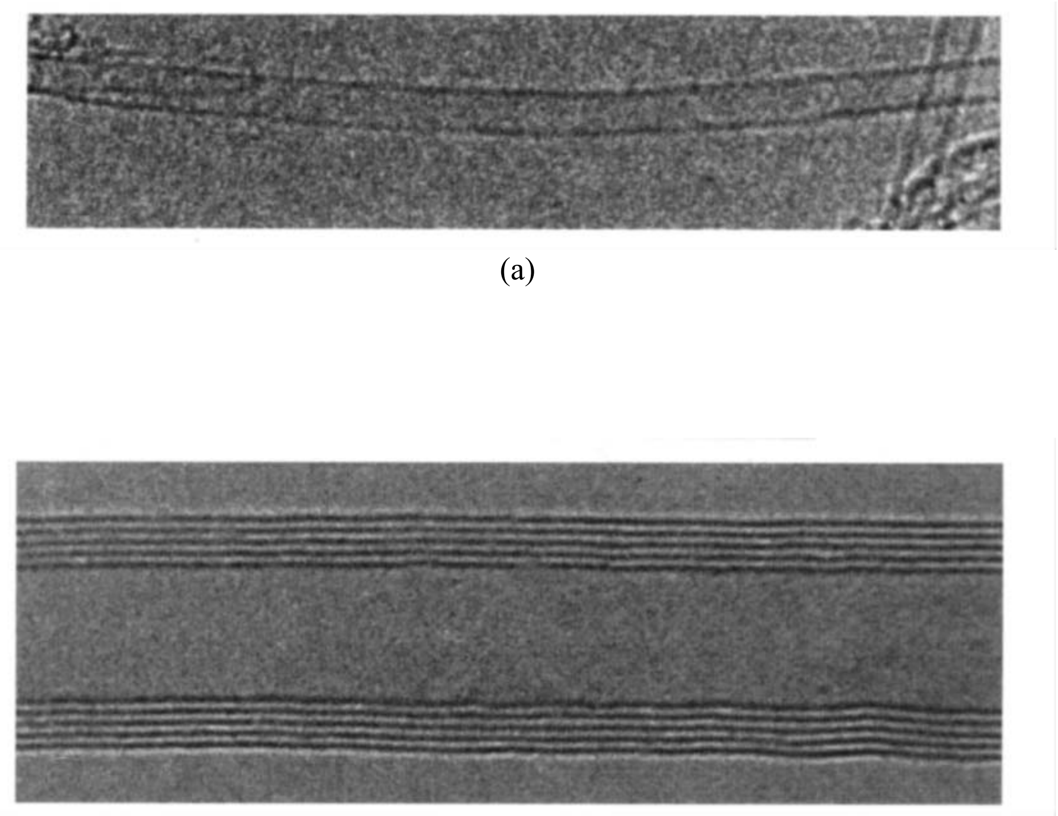

(a)

(b)

Figure 1-7 High-resolution transmission electron microscopy images of (a) SWNTs and (b) MWNTs. Every layer in the image (fringe) corresponds to the edges of each cylinder in the nanotube assembly.

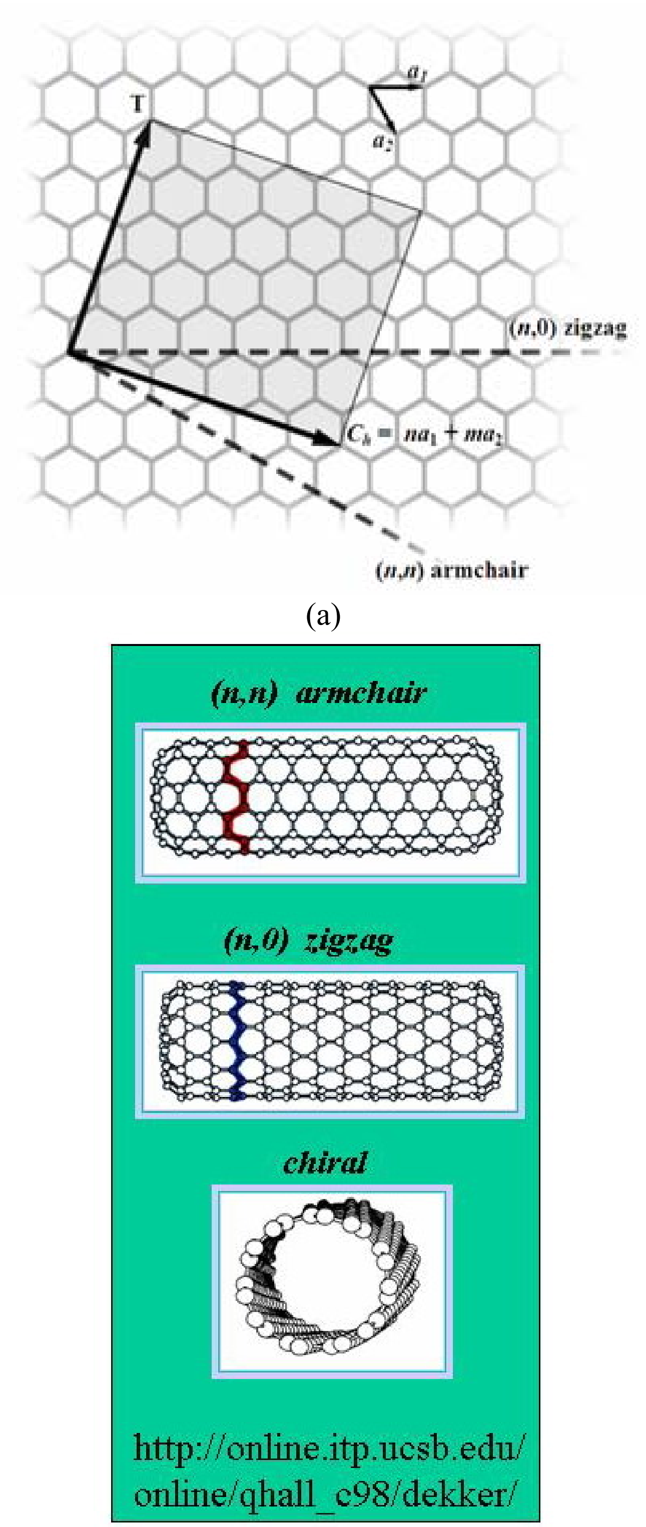

(a)

(b)

Figure 1-8 Molecular models of SWNTs with (a) chiral vector and (b) the categories of the configuration [1.38] [1.39].

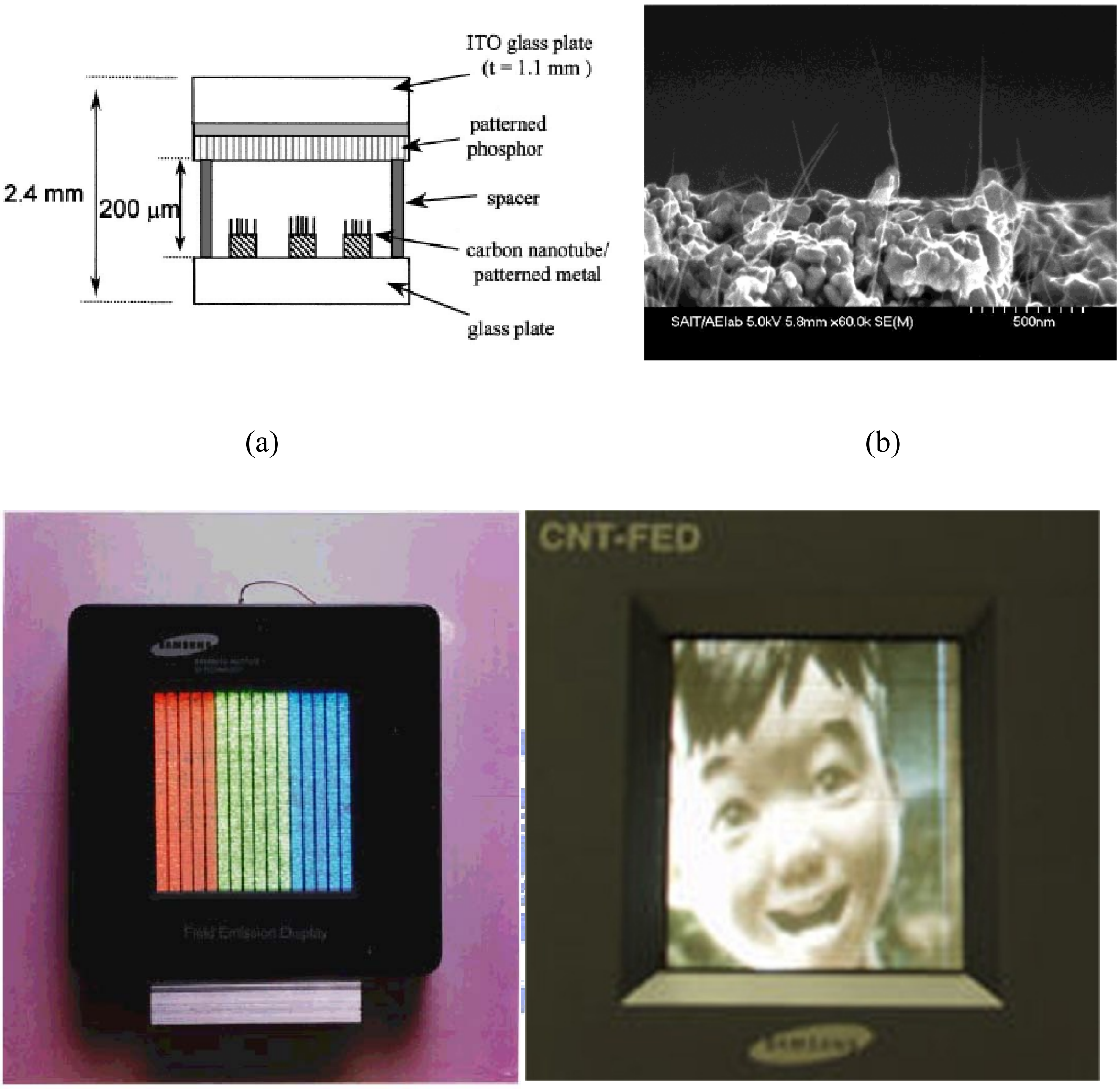

(a) (b)

(c) (d)

Figure 1-9 (a) Schematic structure of the fully sealed 128 lines matrix-addressable CNT-FED, (b) Cross section SEM image of CNT cathode from Samsung's FED,(c) A 4.5-inch FED from Samsung, the emitting image of fully sealed SWNT-FED at color mode with red, green, and blue phosphor columns, and (d) A prototype of 5" CNT flat panel display by Samsung. [1.57]

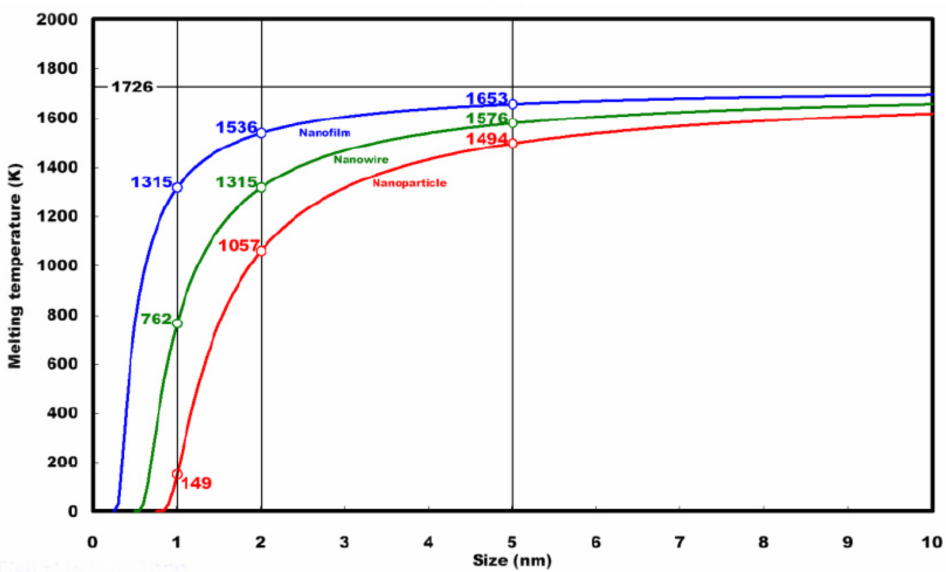

Figure 2-1 Lindemann criterion [2.12]

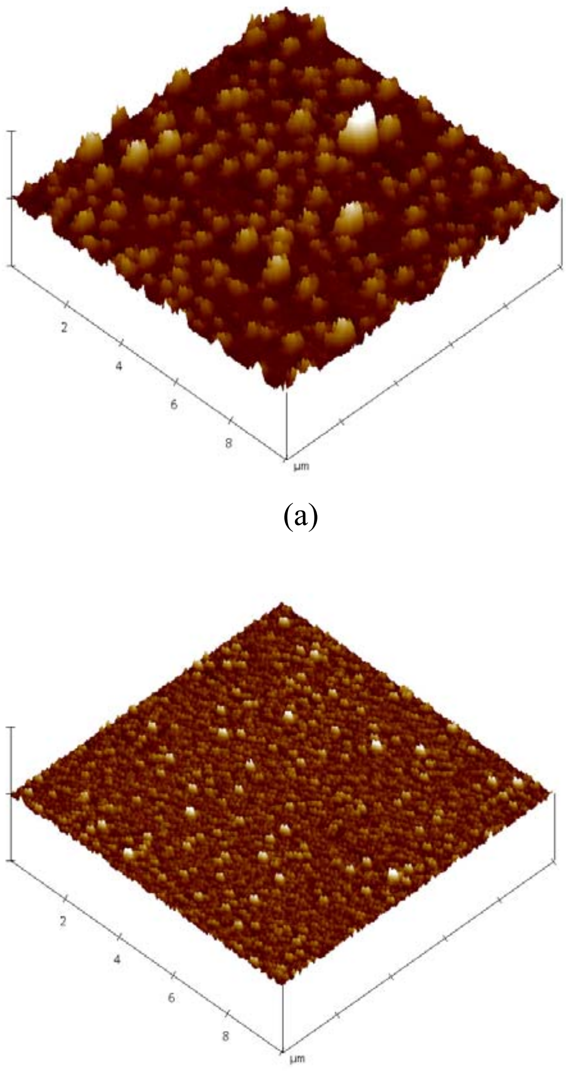

(a)

(b)

Figure 2-2 AFM of the nanoparticles after H_2 (400 sccm) and N_2 (600 sccm) at 700 ℃ for 5 min: (a) the pure Fe catalyst layer (the conventional sample), and (b) the Ti-Fe codeposited catalyst layer (the proposed sample). [2.14]

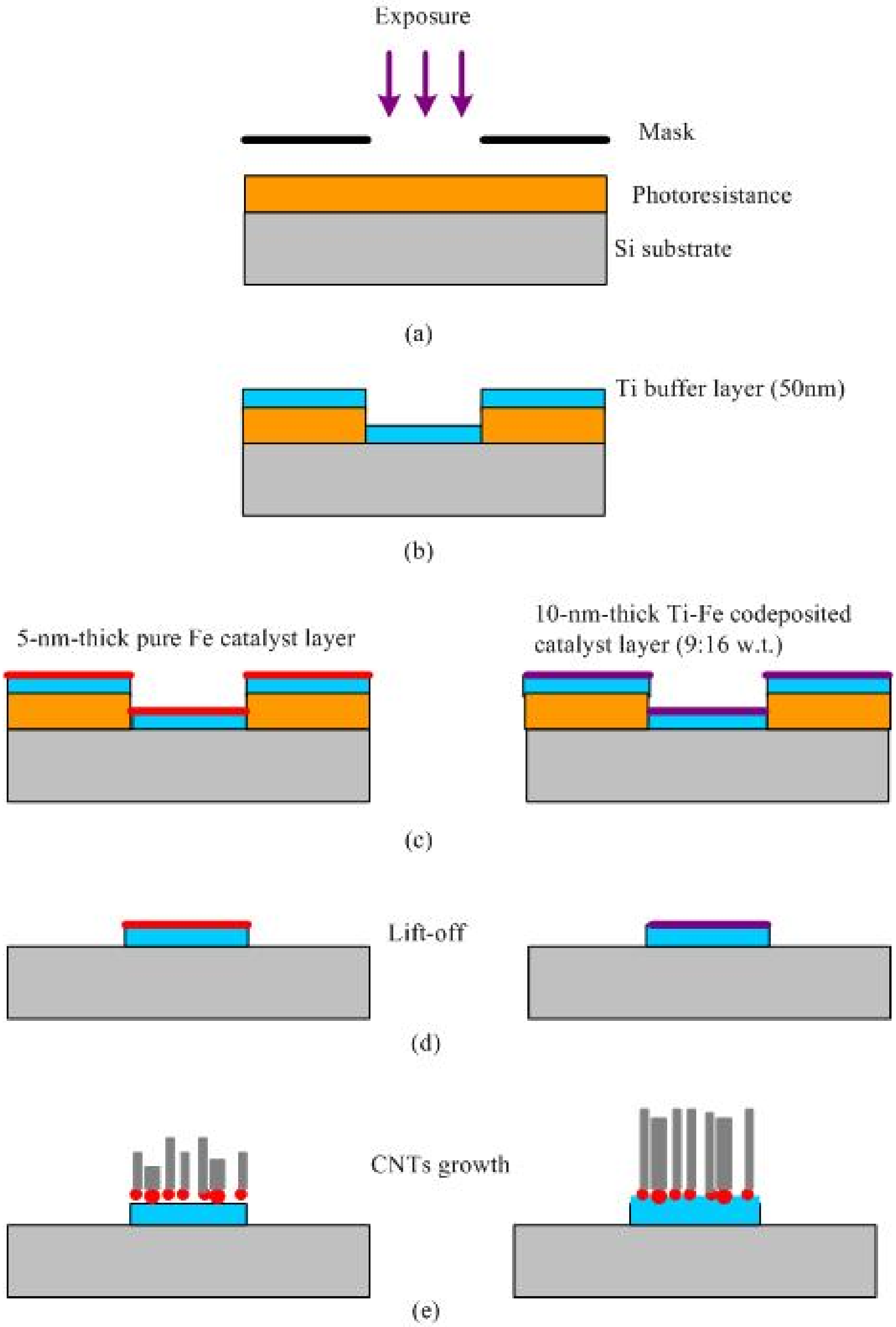

Figure 2-3 The experimental procedures for CNTs synthesis.

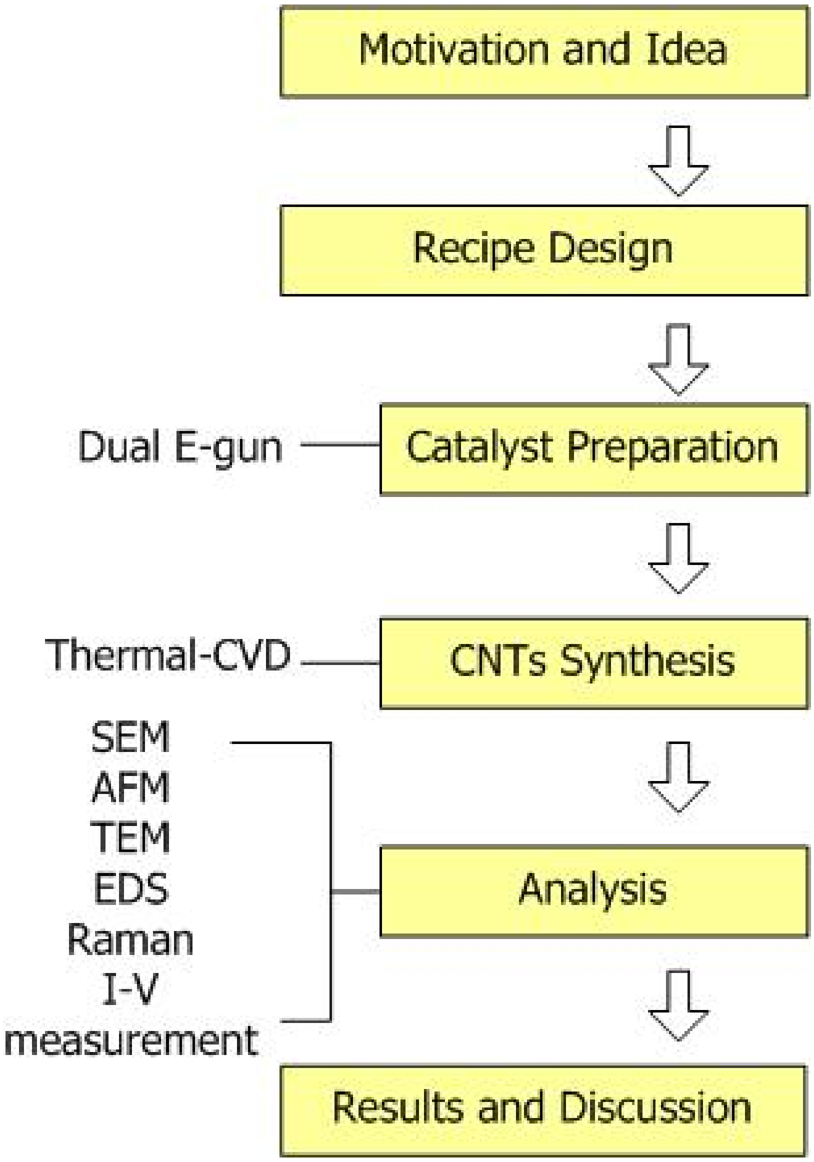

Figure 2-4 The schematic experimental flow chart

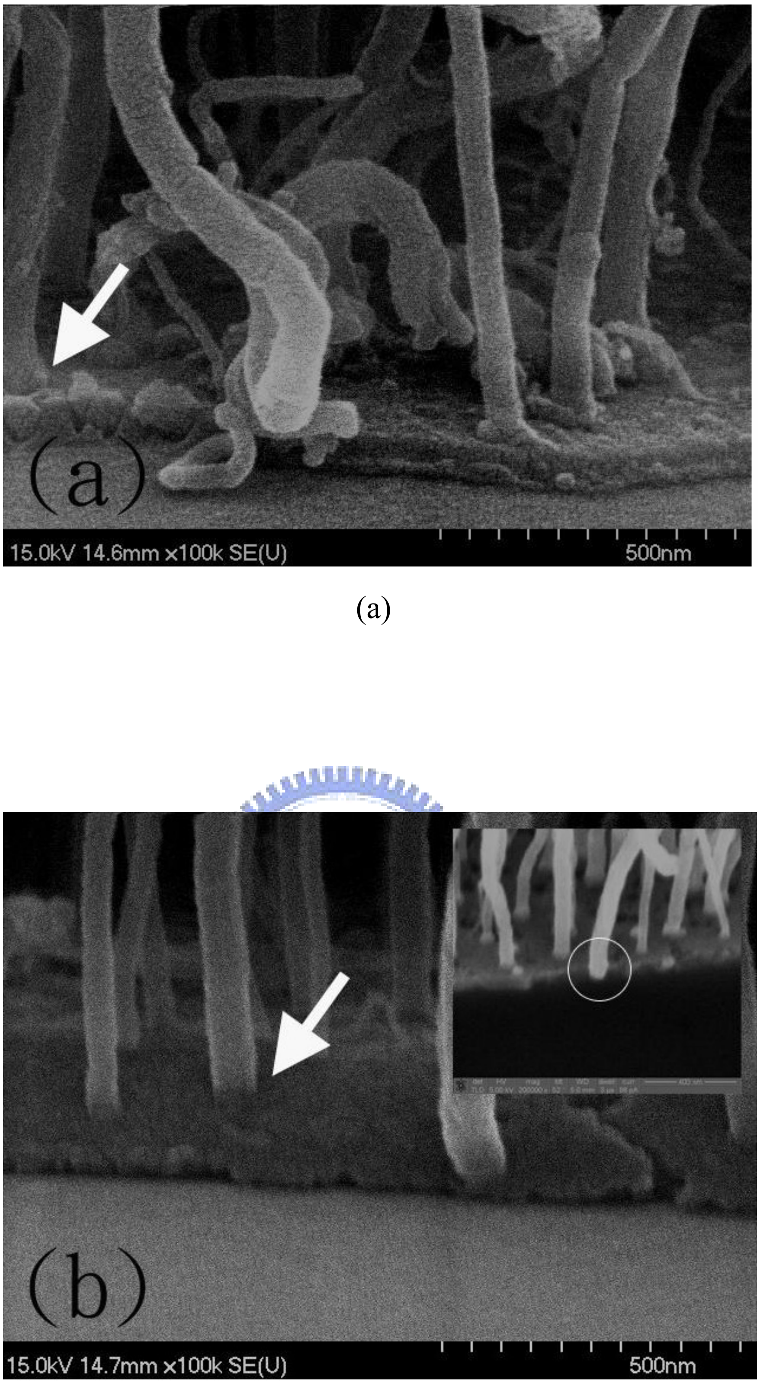

(a)

(b)

Figure 2-5 (a) The SEM image of the conventional samples and (b) the SEM image of the proposed samples (the inset in (b) is the SEM micrograph of the proposed samples cleaved across the patterned region and a CNT partially immersed in the catalytic layer is marked by a circle)

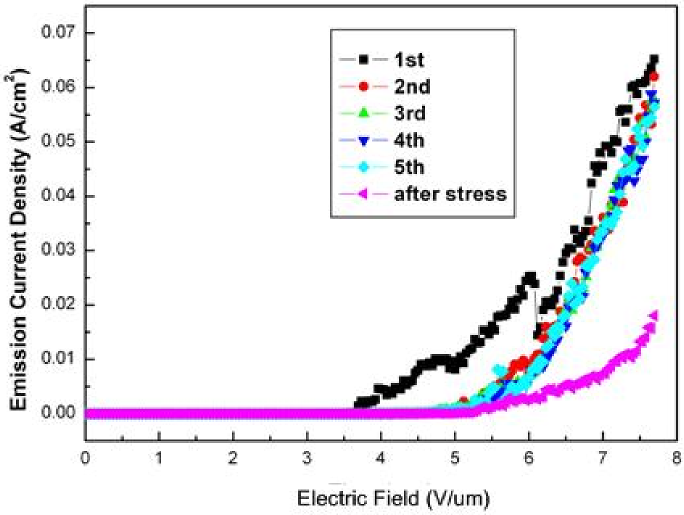

(a)

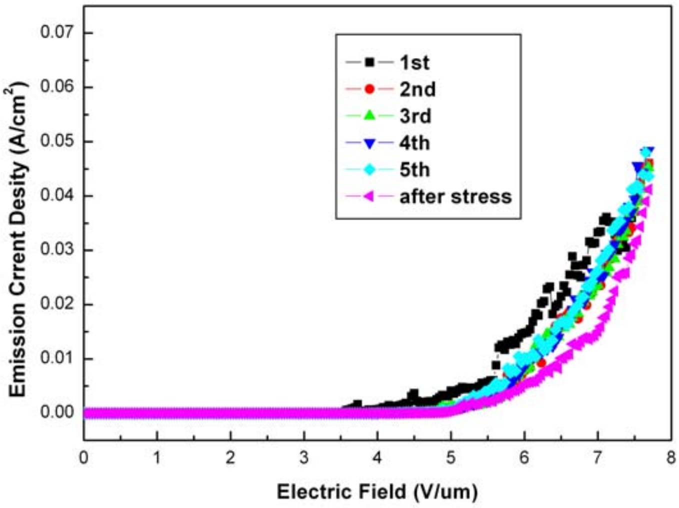

(b)

Figure 2-6 The plot of emission current density versus electric field for (a) the conventional samples and (b) the plot of emission current density versus electric field for the proposed samples.

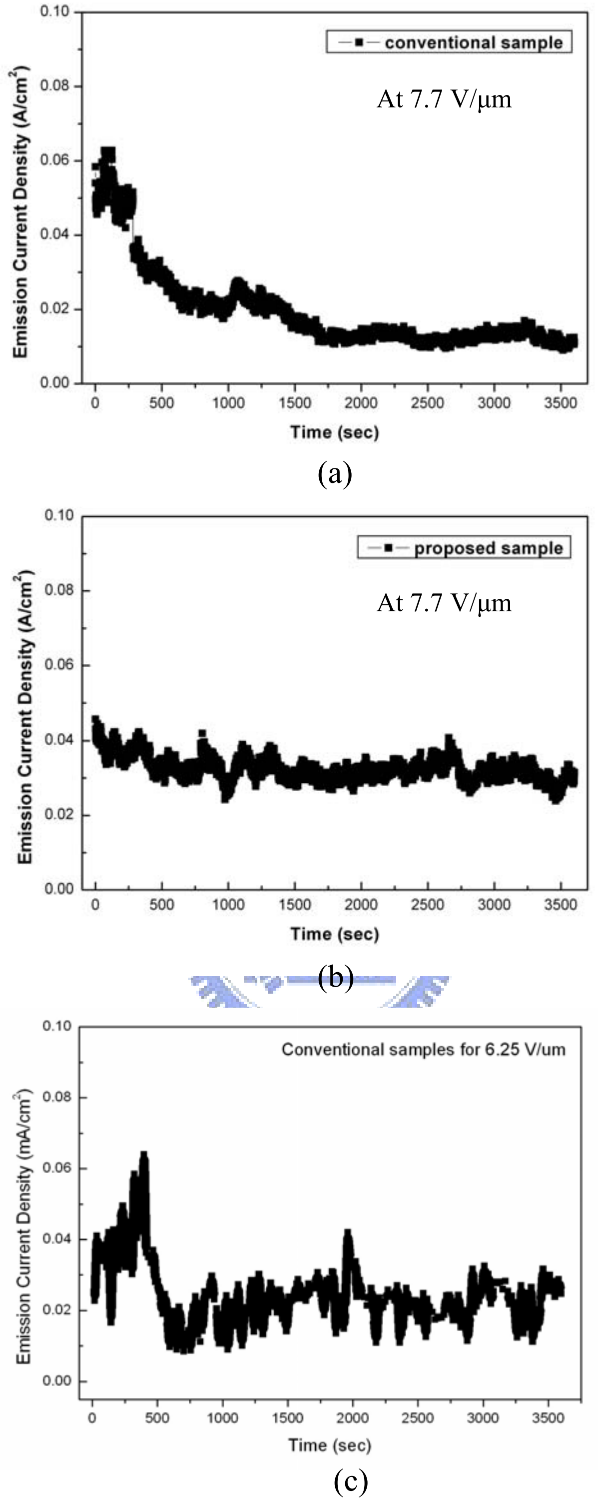

Figure 2-7 The plot of emission current density versus time for 3,600 sec (a) for the conventional samples at 7.7 V/μm, (b) for the proposed samples at 7.7 V/μm and (c) for the conventional samples at 6.25 V/μm.

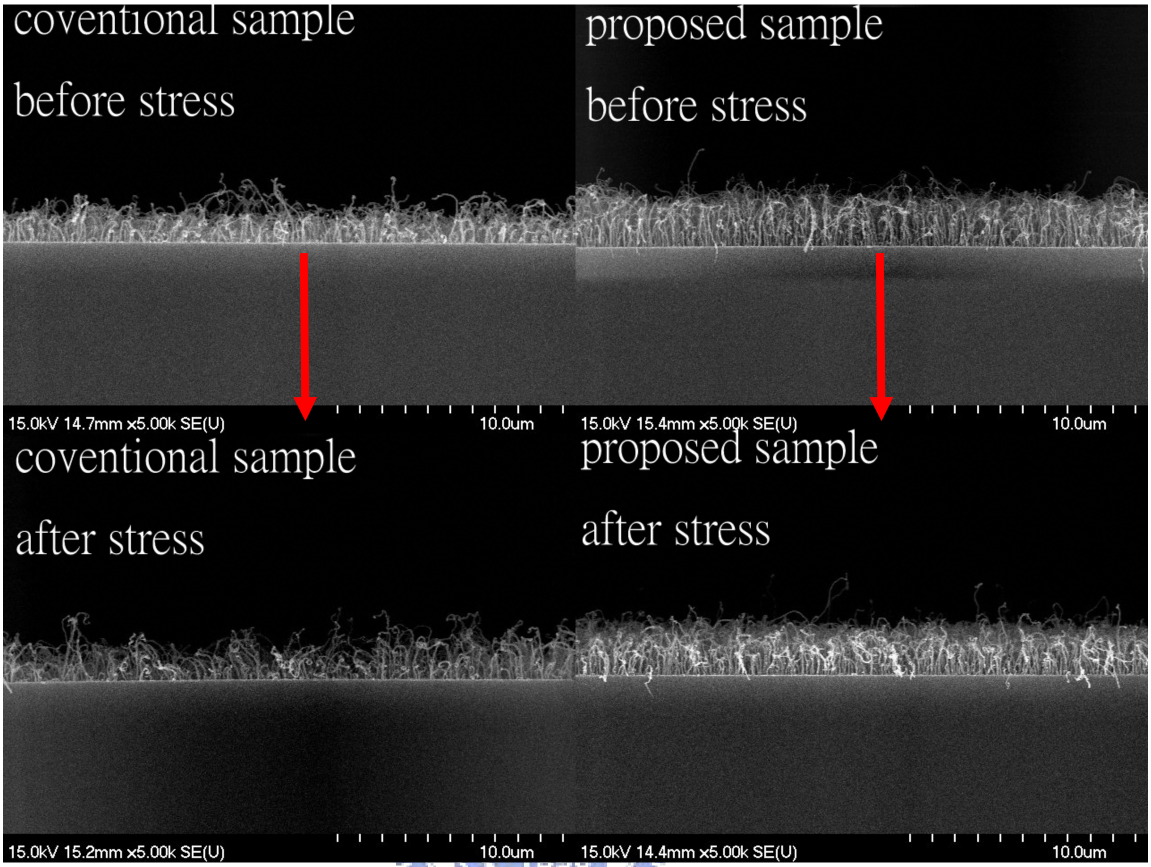

Figure 2-8 It shows the SEM images of both the conventional and the proposed specimens before and after the time stress.

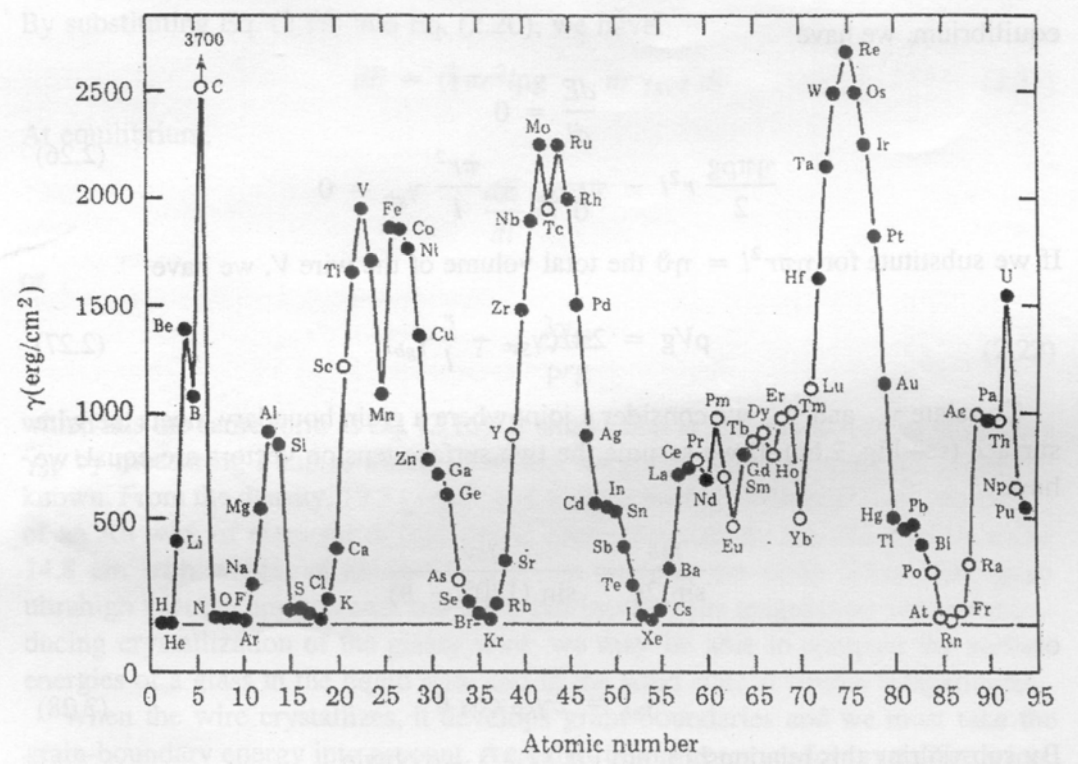

Figure 2-9 The calculated surface energy for period table elements.[2.16]

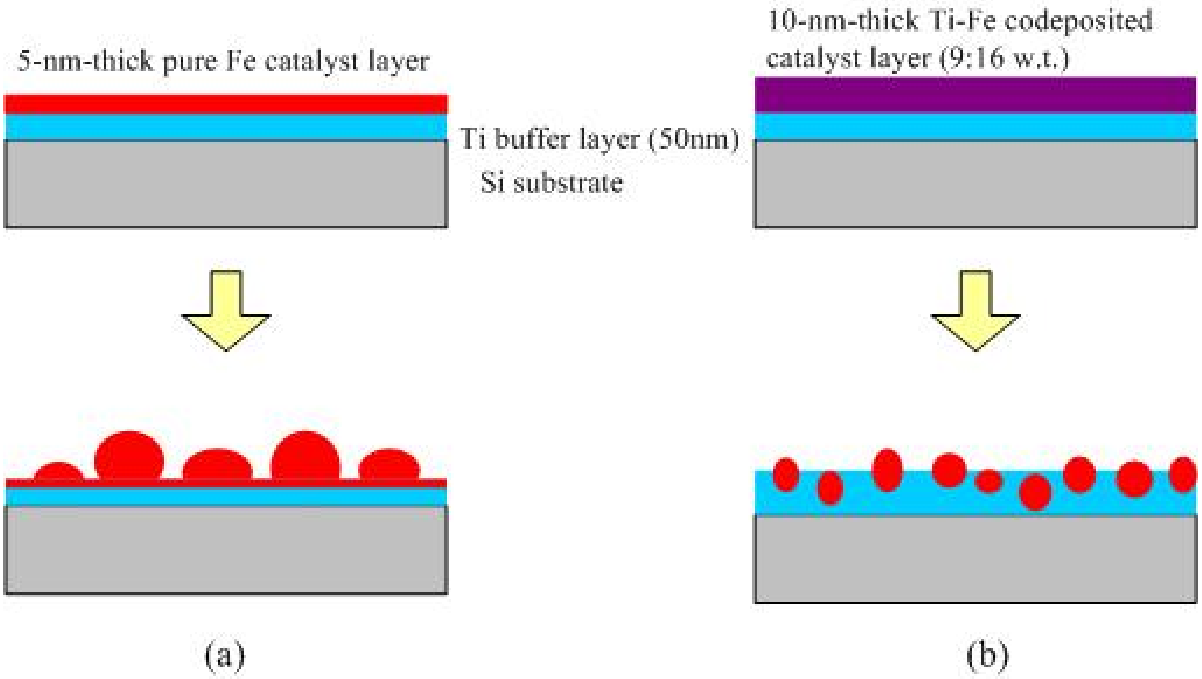

Figure 2-10 The mechanism of the nanoparticle formation for (a) the conventional samples and (b) the proposed samples.

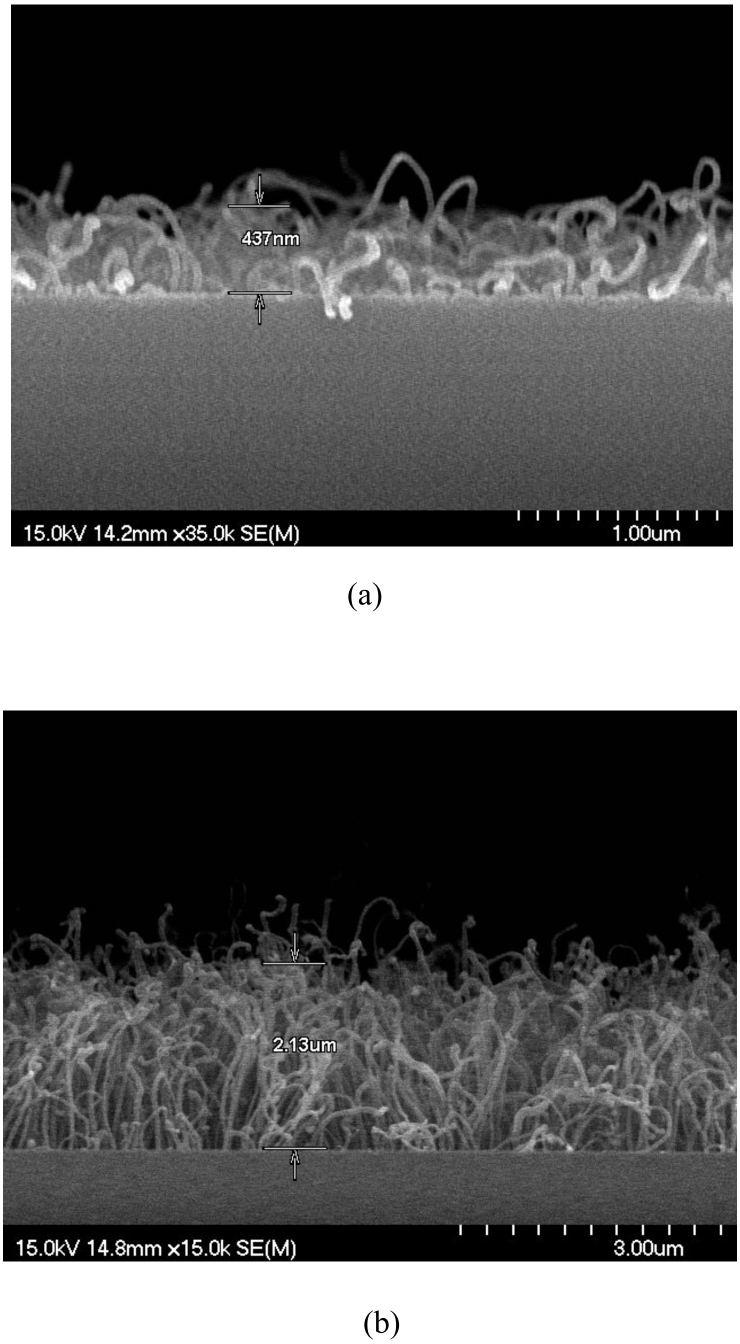

Figure 2-11 The SEM images of CNTs after thermal CVD synthesis for (a) the conventional samples and (b) the proposed samples.

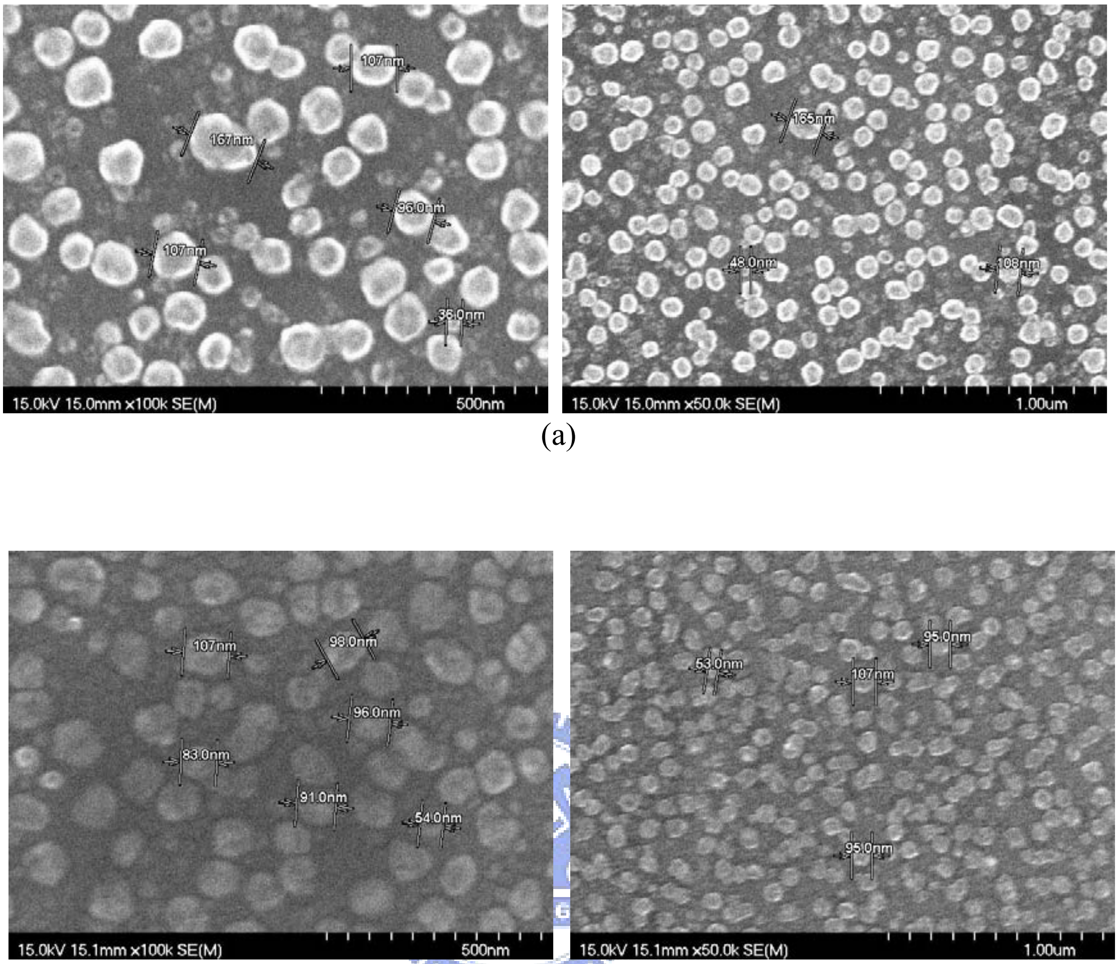

(a)

(b)

Figure 2-12 The SEM images of the nanoparticles after H_2 (200 sccm)and N_2 (500 sccm) pretreatment for 12 min at 550 ℃. (a) the conventional samples and (b) the proposed samples.

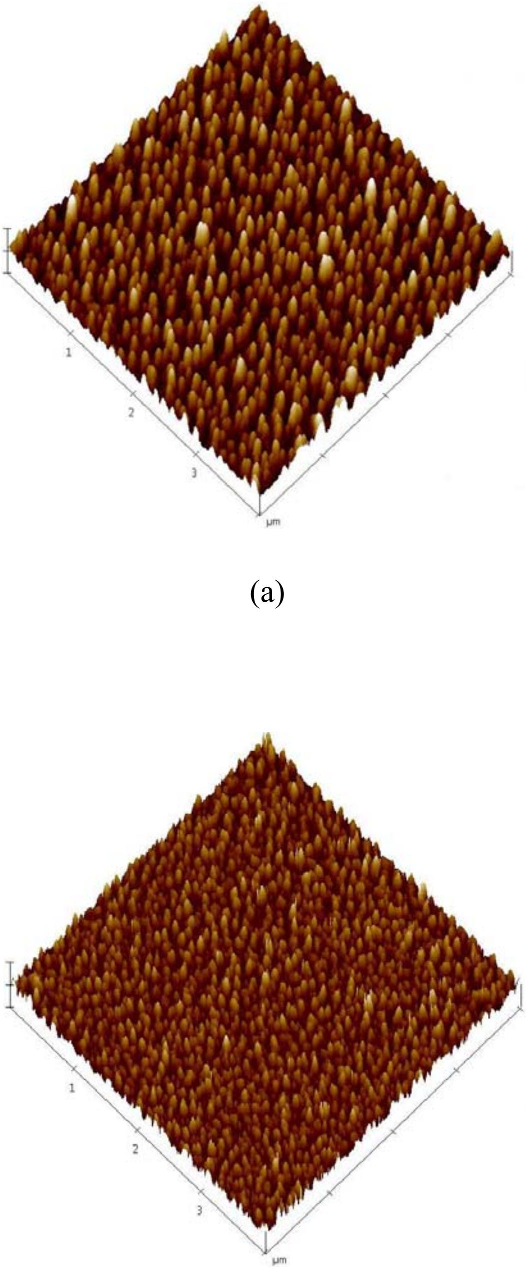

(a)

(b)

Figure 2-13 The AFM images of the nanoparticles after H_2 (200 sccm)and N_2 (500 sccm) pretreatment for 12 min at 550 ℃. (a) the conventional samples and (b) the proposed samples.

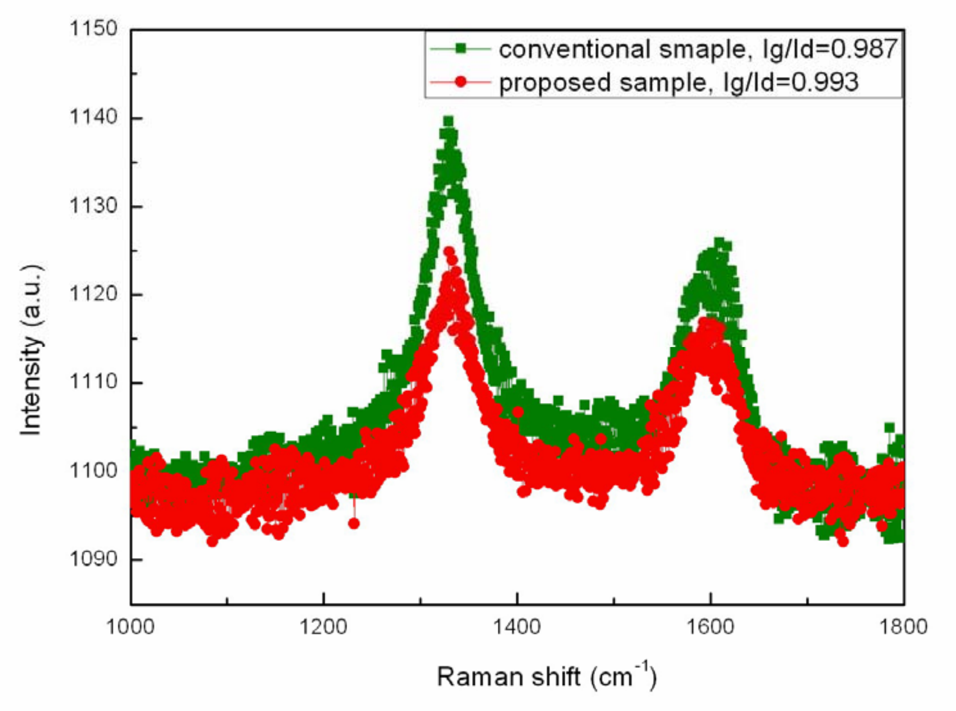

Figure 2-14 Raman spectra of the CNTs for the conventional samples and the proposed samples.

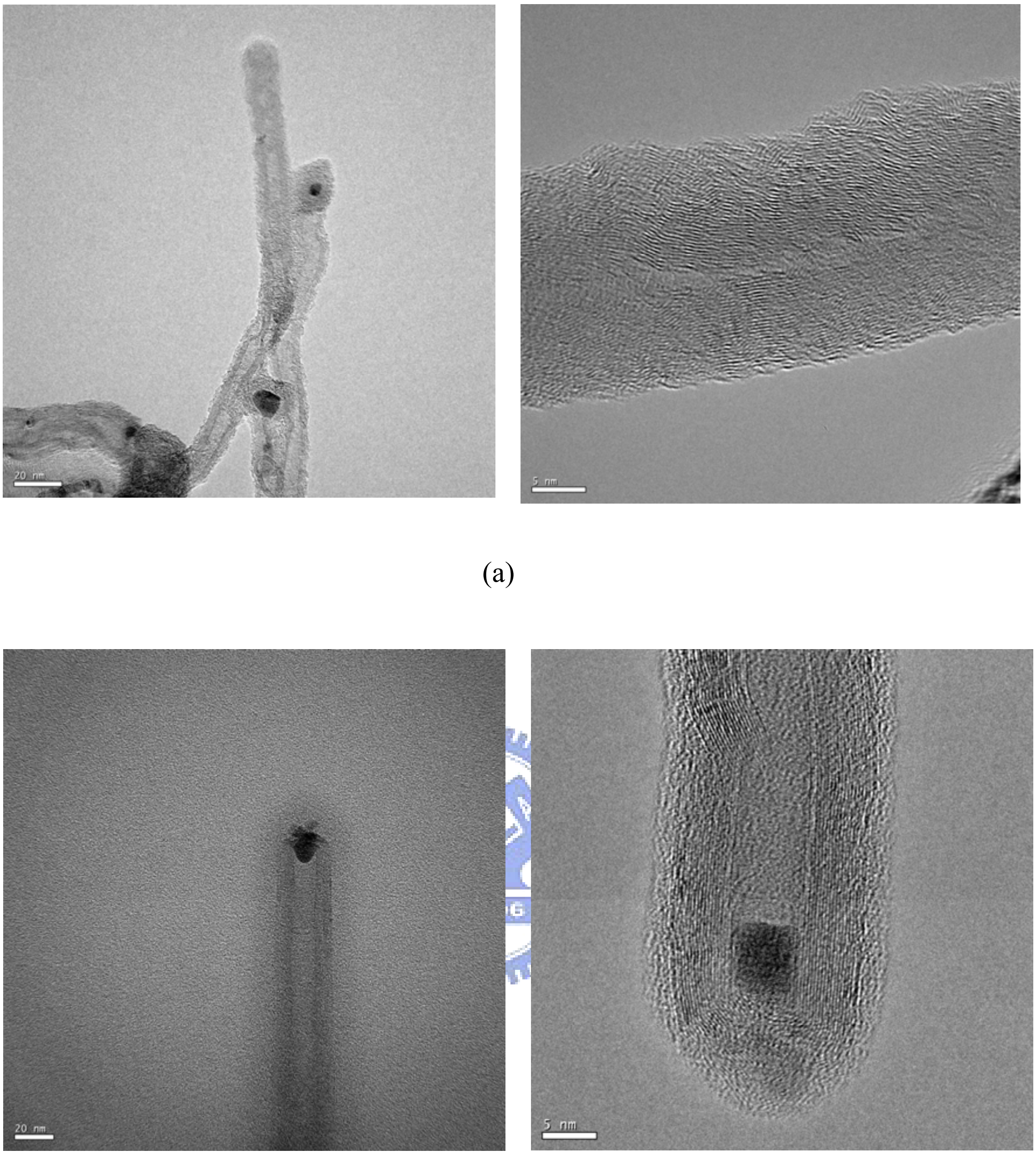

(a)

(b)

Figure 2-15 The TEM images of the CNTs for (a) the conventional samples and (b) for the proposed samples.

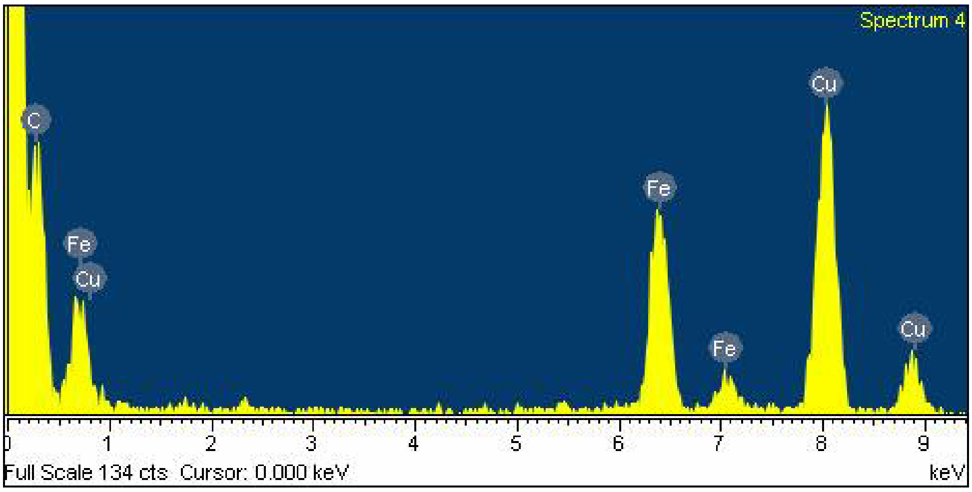

(a)

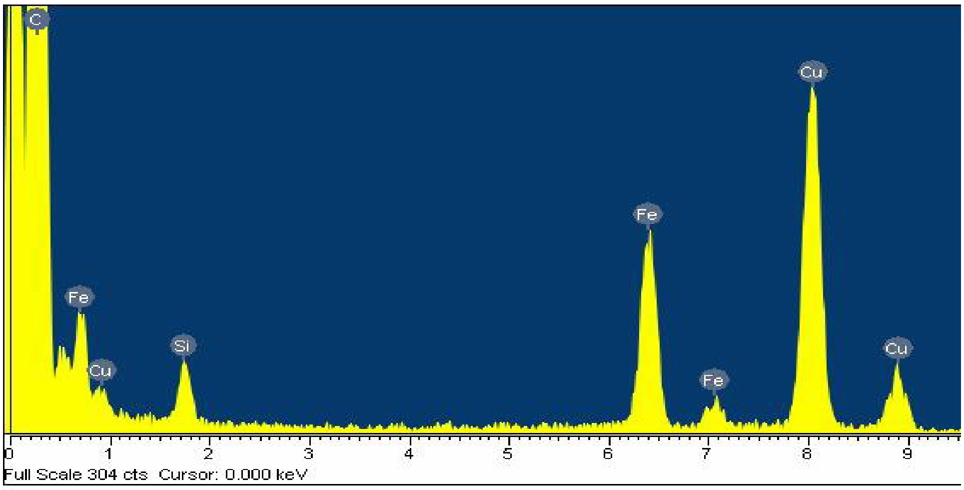

(b)

Figure 2-16 The EDS analysis of the CNTs for (a) the conventional samples and (b) the proposed samples.

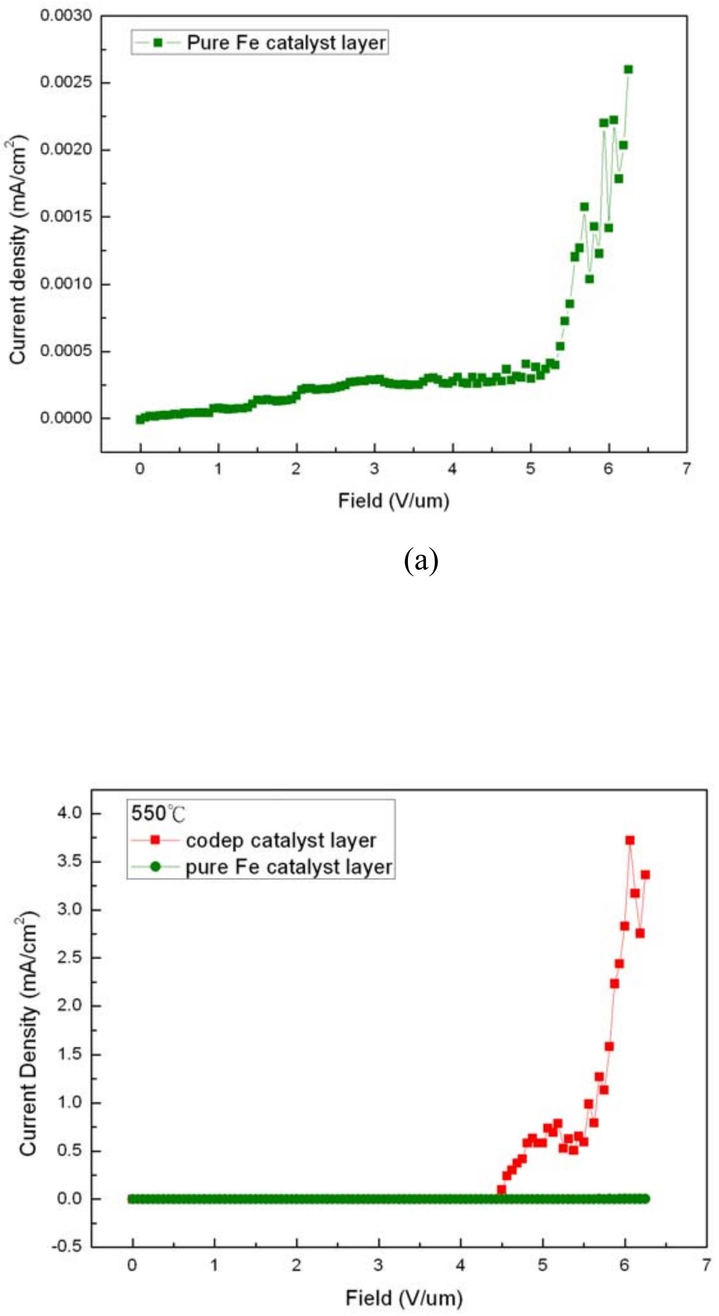

(a)

(b)

Figure 2-17 The current density versus electrical field for (a) the conventional samples and (b) the proposed samples.

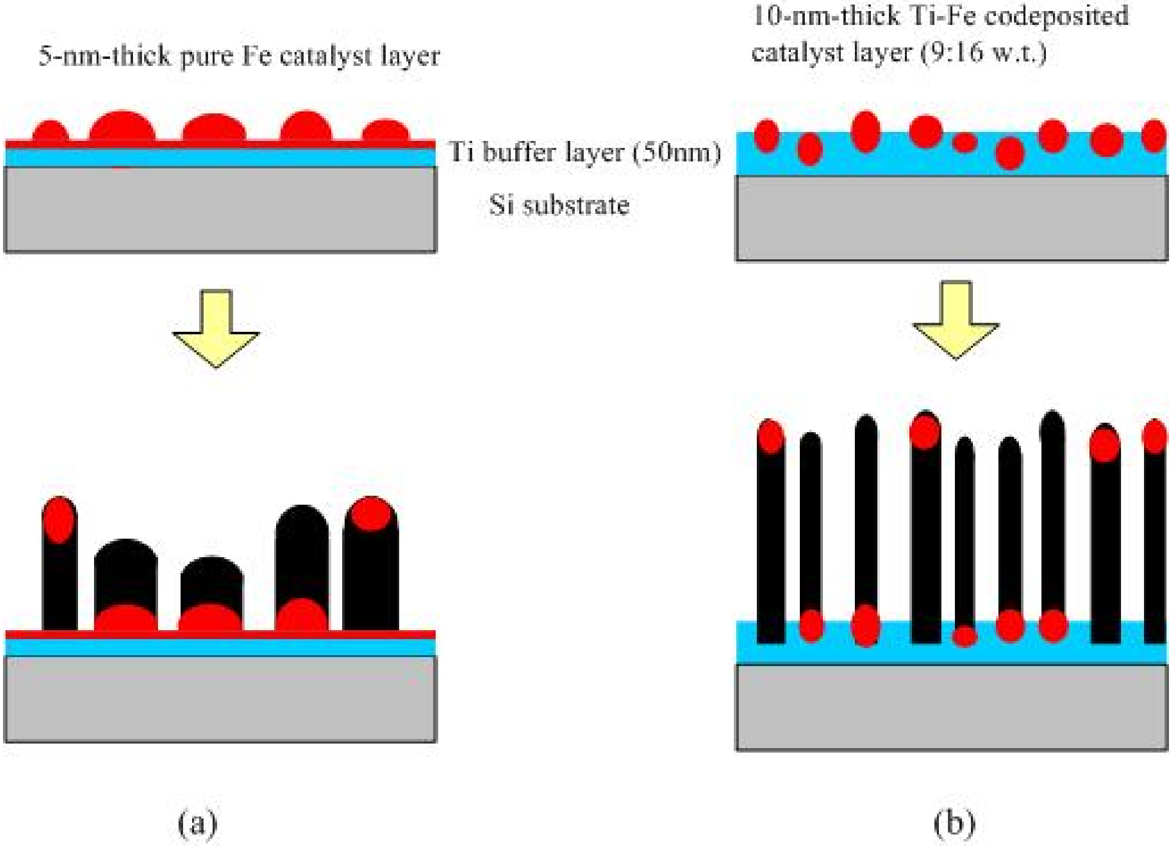

Figure 2-18 The schematic diagram of the CNTs growth for (a) the conventional samples and (b) the proposed samples.

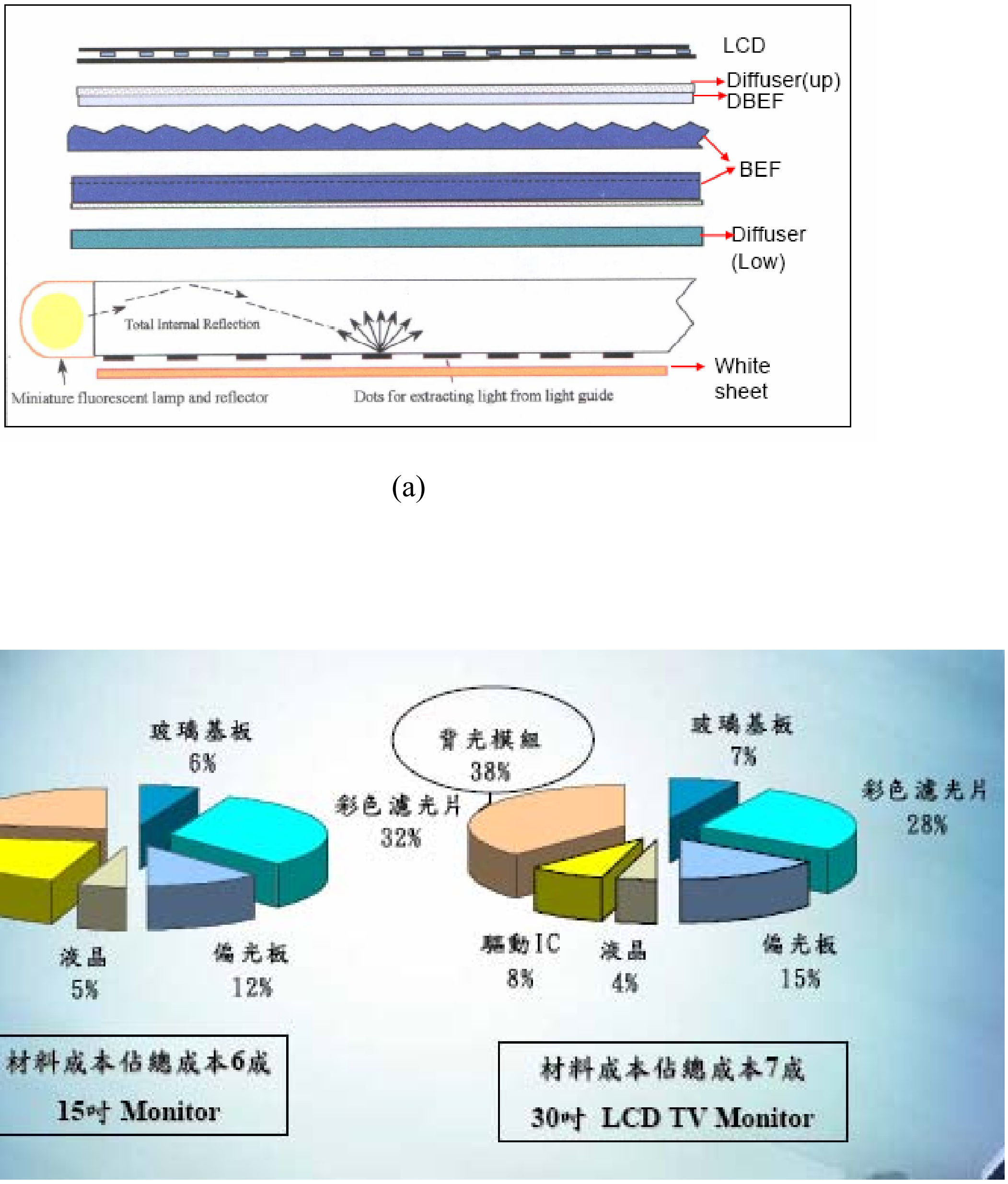

(a)

(b)

Figure 3-1 (a) The schematic of a typical BLU for LCDs and (b) the cost structure of materials for TFT- LCDs. [3.1]

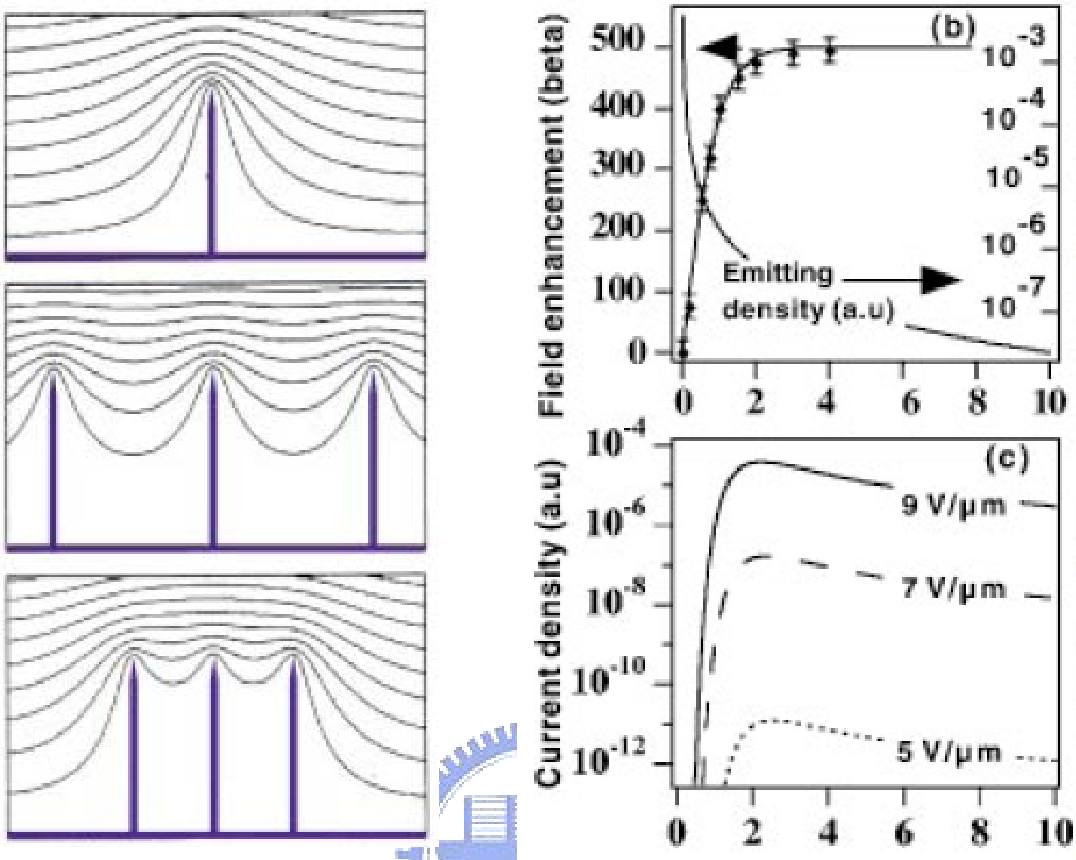

(a)

Figure 3-2 (a) Simulation of the equipotential lines of the electrostatic field for tubes of 1 μm height and 2 nm radius, for distances between tubes of 4, 1, and 0.5 μm, (b) along with the corresponding changes of the field enhancement factor β and emitter density ,and (c) current density as a function of the distance. [3.7]

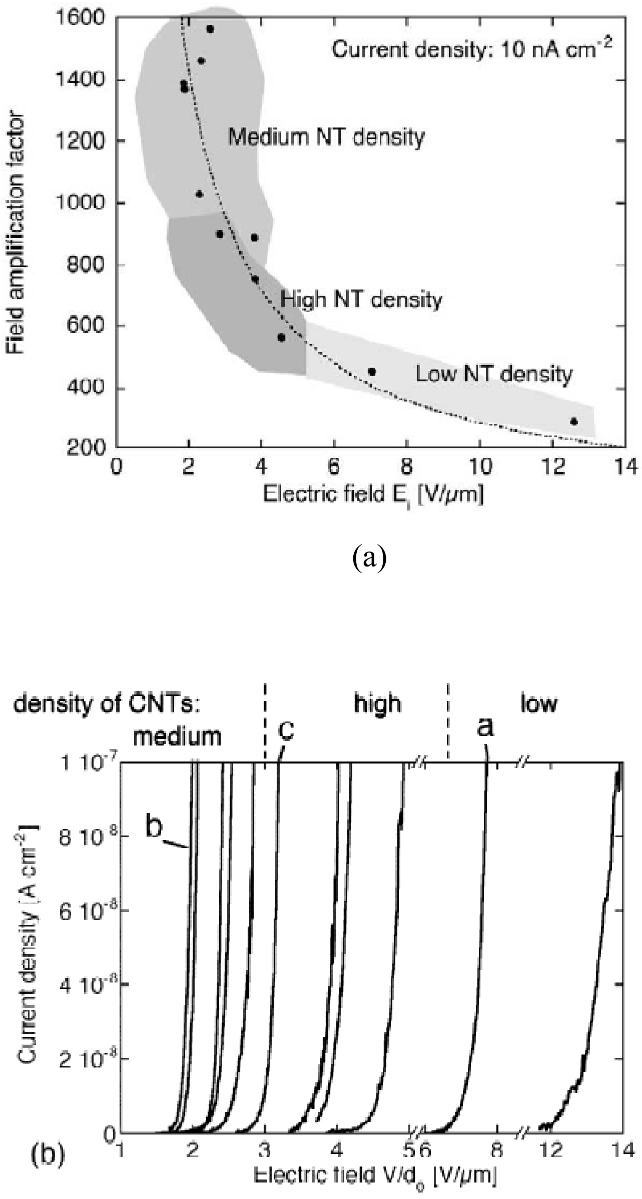

Figure 3-3 (a) Field amplification factor β as a function of the onset field after training, Ei, for the films obtained by CVD with different catalyst concentrations and (b) Low current field emission characteristics of the 11 samples after training. [3.8]

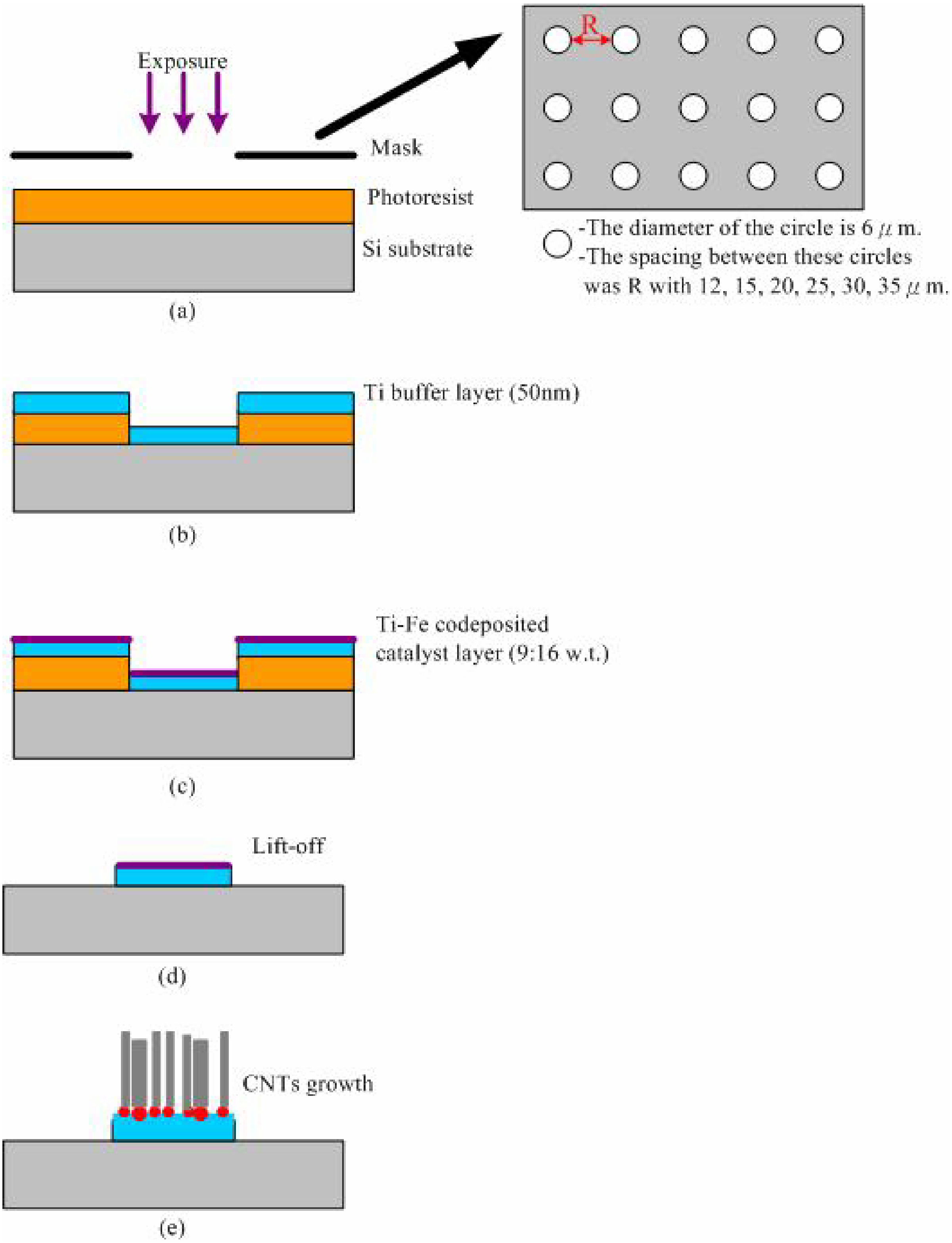

Figure 3-4 Experimental procedures for CNT pillars synthesized

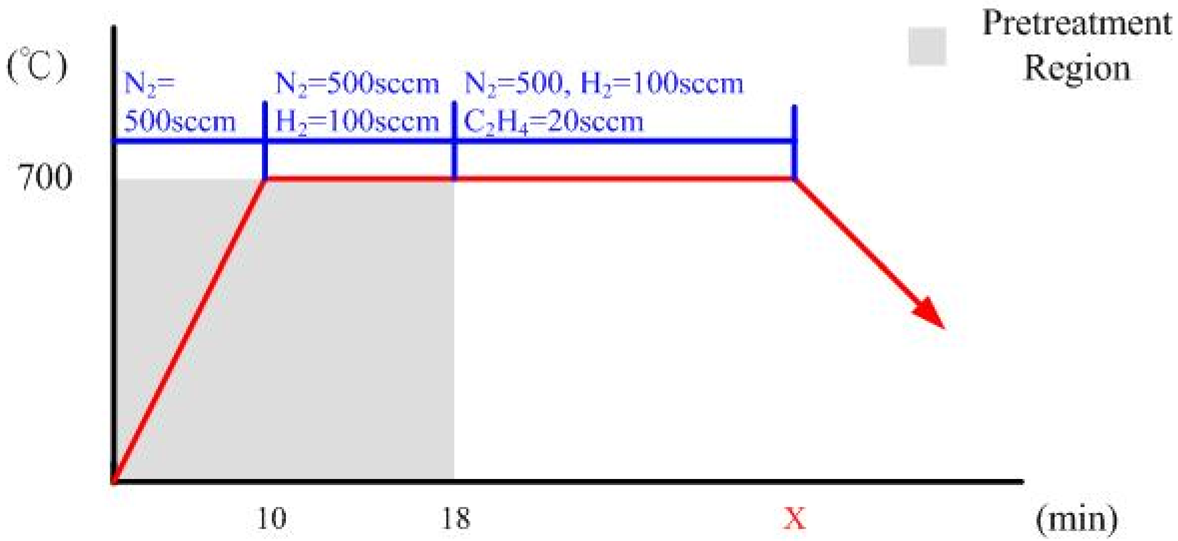

Figure 3-5 Growth condition of CNT pillars in the thermal CVD system.

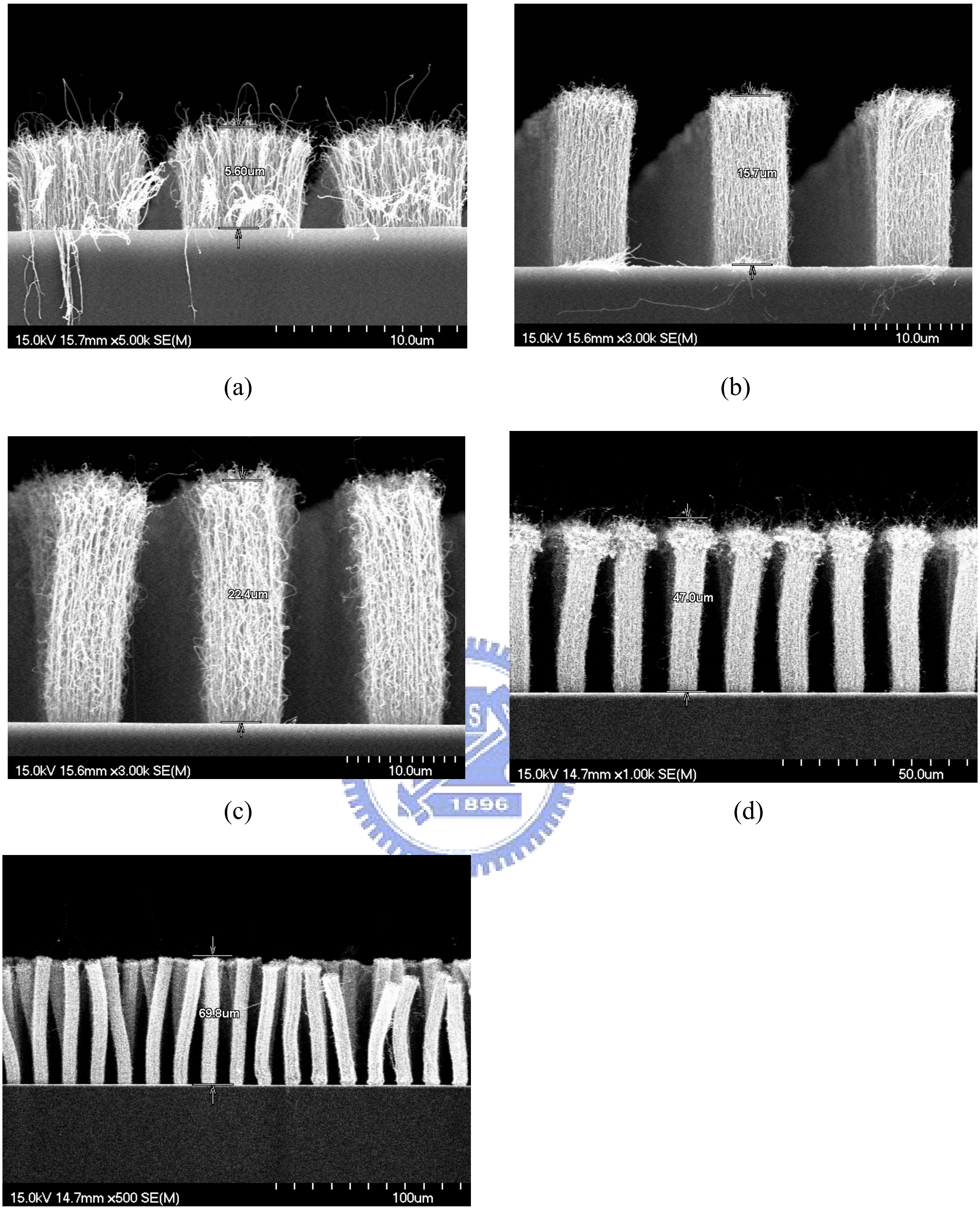

(a) (b) (c) (d) (e)

Figure 3-6 The SEM images of the CNT pillars of the conventional samples for different grown time, (a) 8 min, (b) 15 min, (c) 30 min, (d) 60 min, and (e) 120 min.

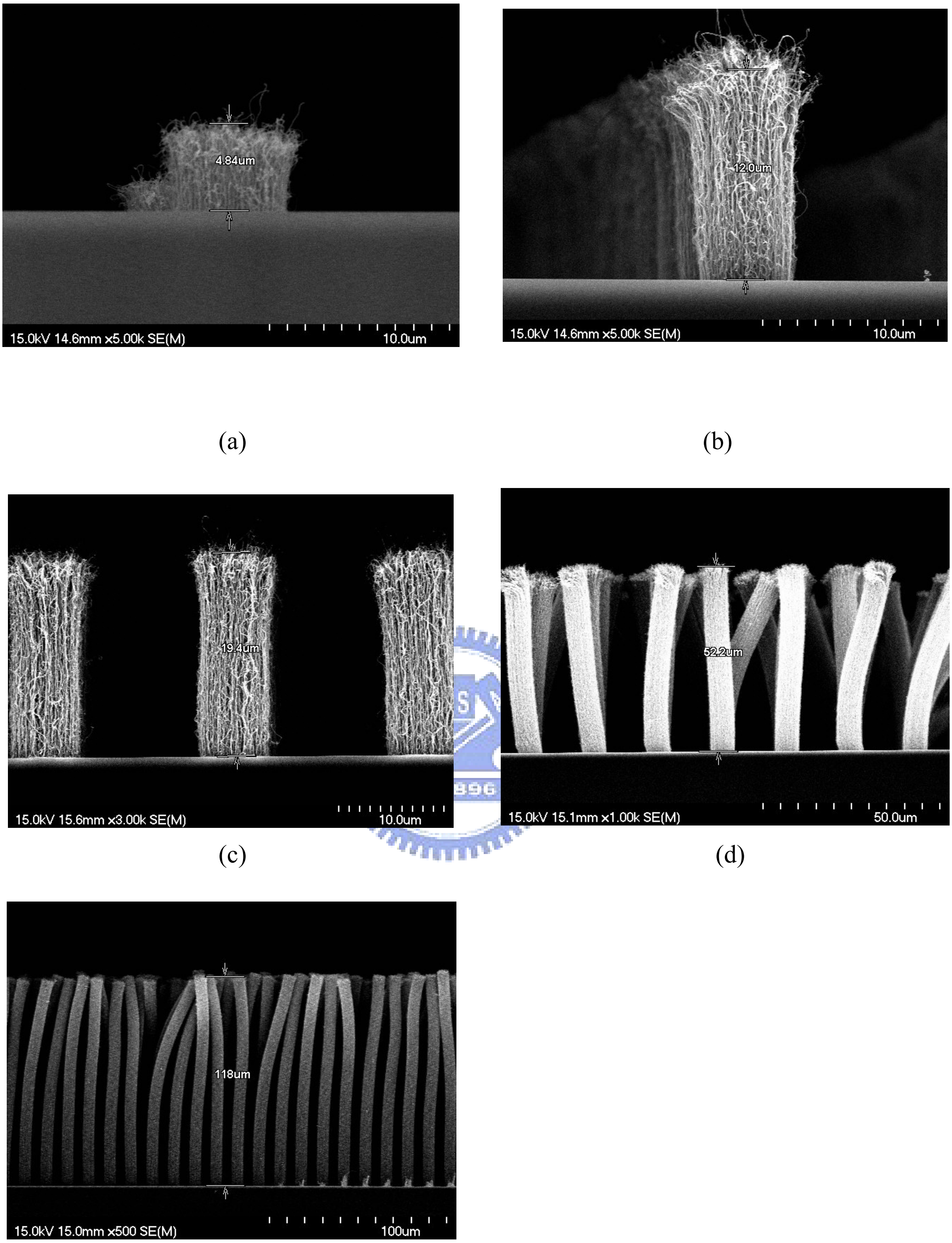

(a) (b)

(c) (d)

(e)

Figure 3-7 The SEM images of the CNT pillars of the proposed samples for different growth time, (a) 8 min, (b) 15 min, (c) 30 min, (d) 60 min, and (e) 120 min.

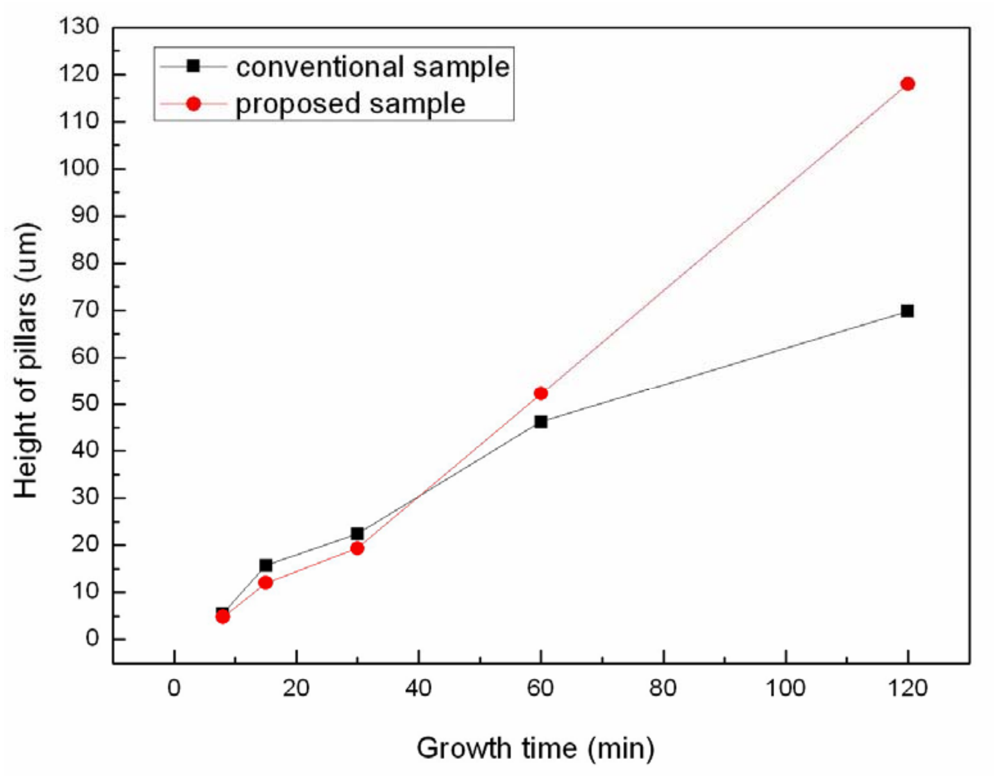

Figure 3-8 The lengths of the CNT pillars vs. the growth reaction time for the conventional and proposed samples.

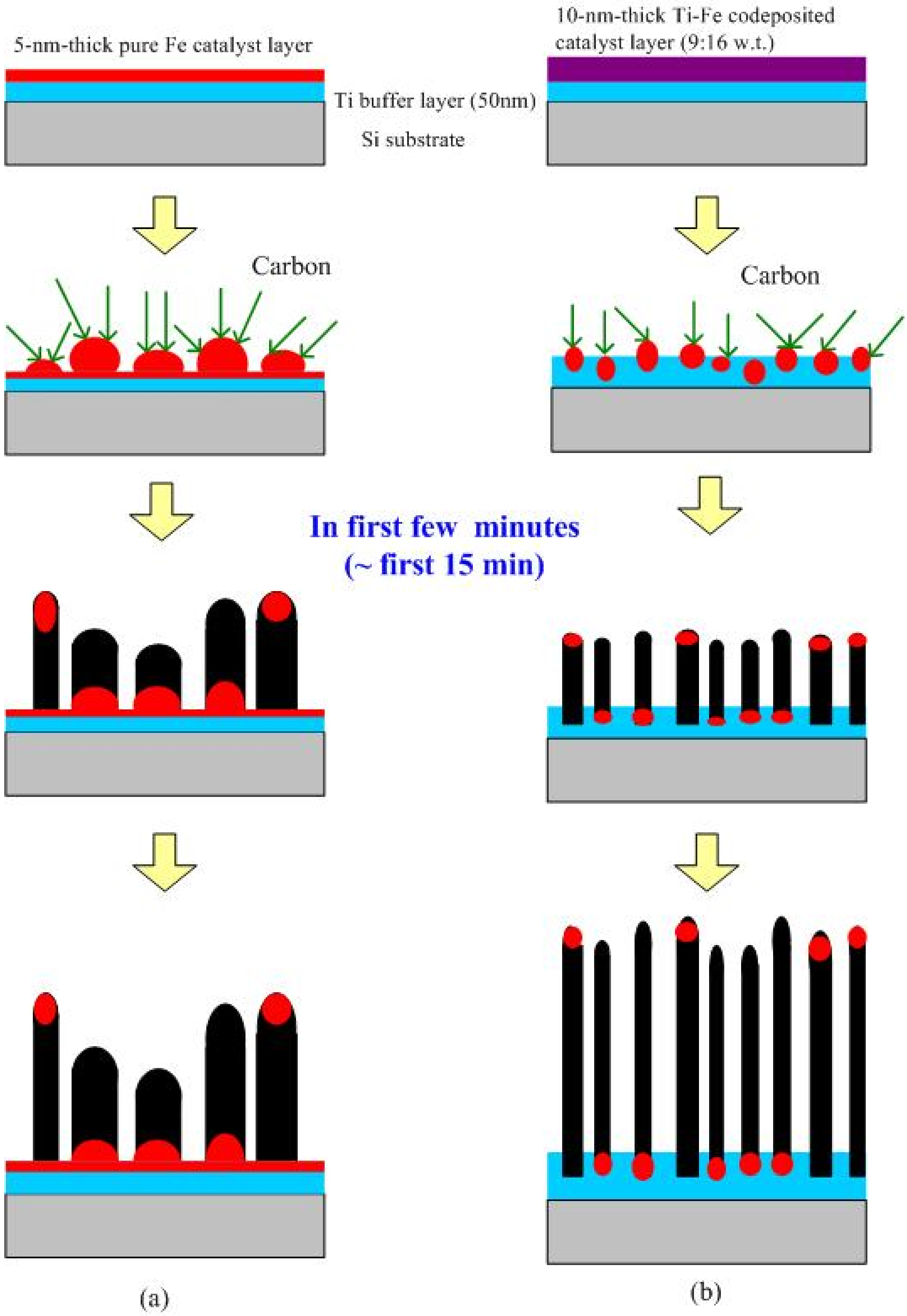

Figure 3-9 The schematic mechanism of the CNT pillar growth for (a) the conventional and (b) the proposed samples.

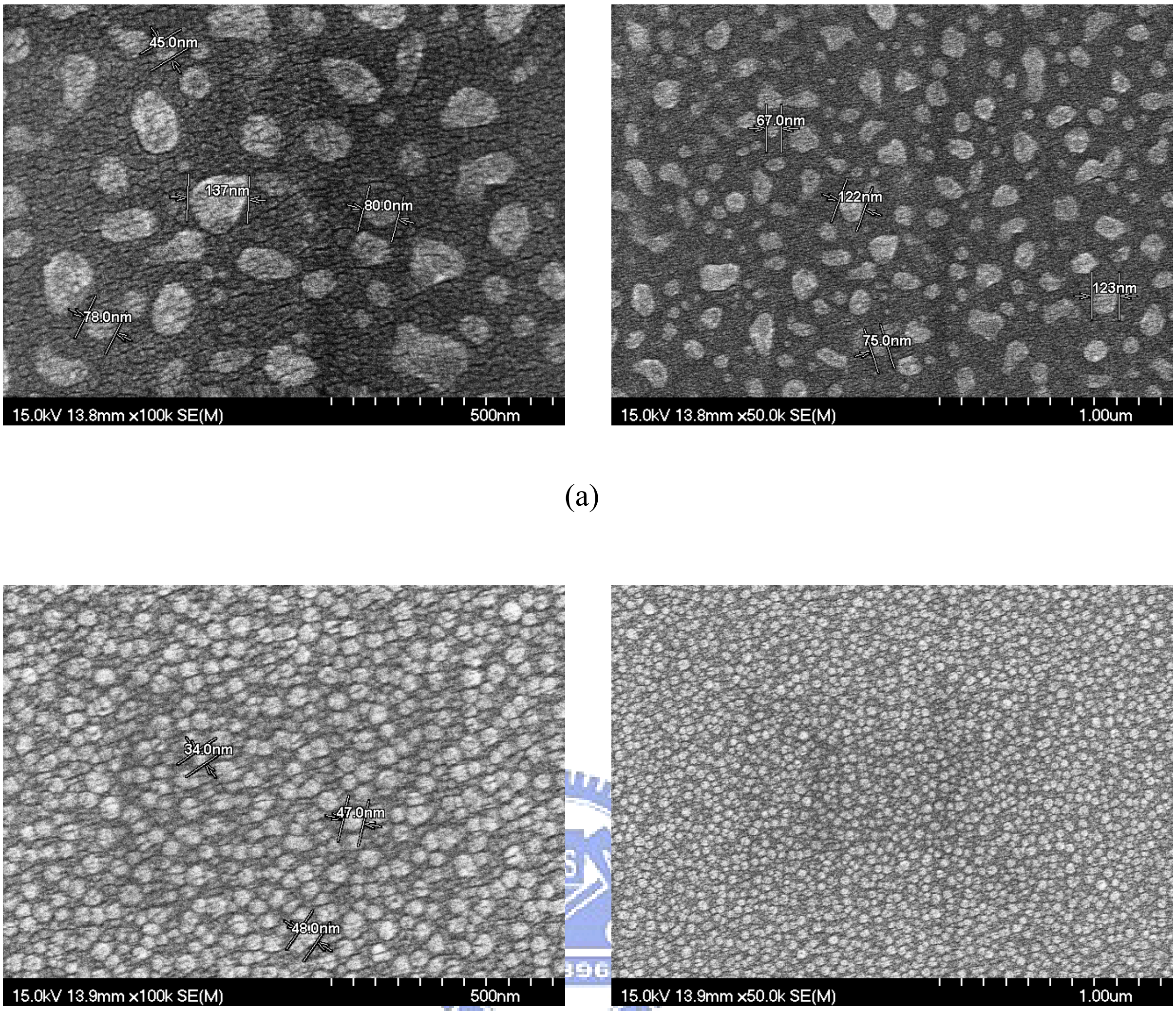

(a)

(b)

Figure 3-10 The SEM images of the catalyst nanoparticles after pretreatment for (a) the conventional and (b) the proposed samples.

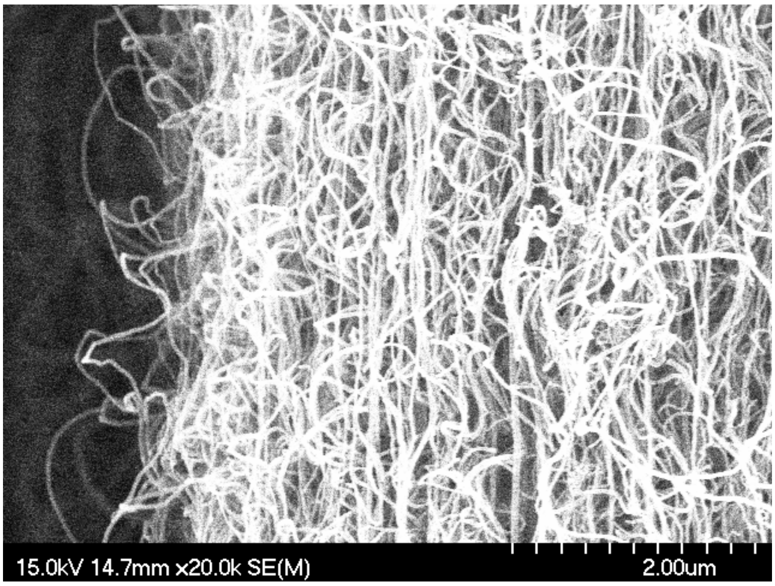

(a)

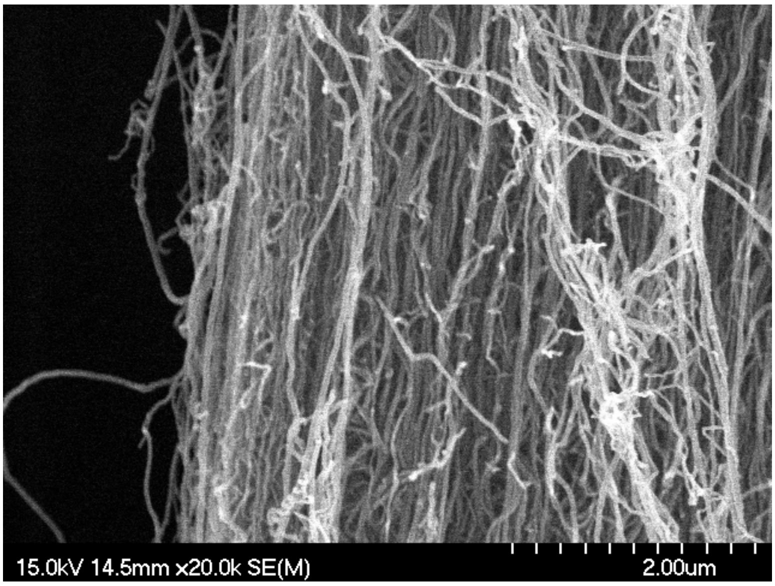

(b)

Figure 3-11 The SEM images of the CNT pillars growth for (a) the conventional and (b) the proposed samples.

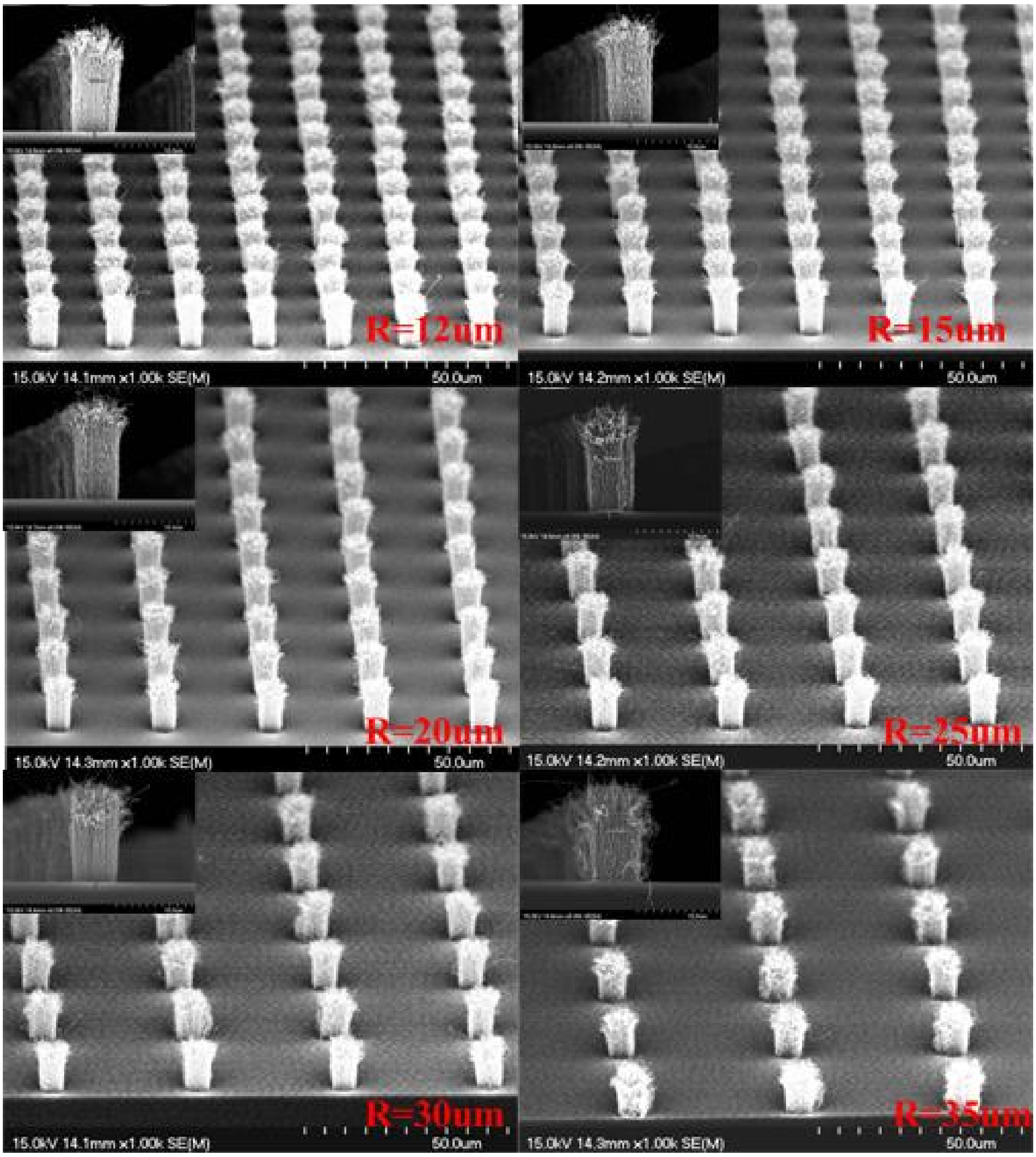

Figure 3-12 The SEM images of CNT pillars in the proposed samples for growth time of 15 min with different R.

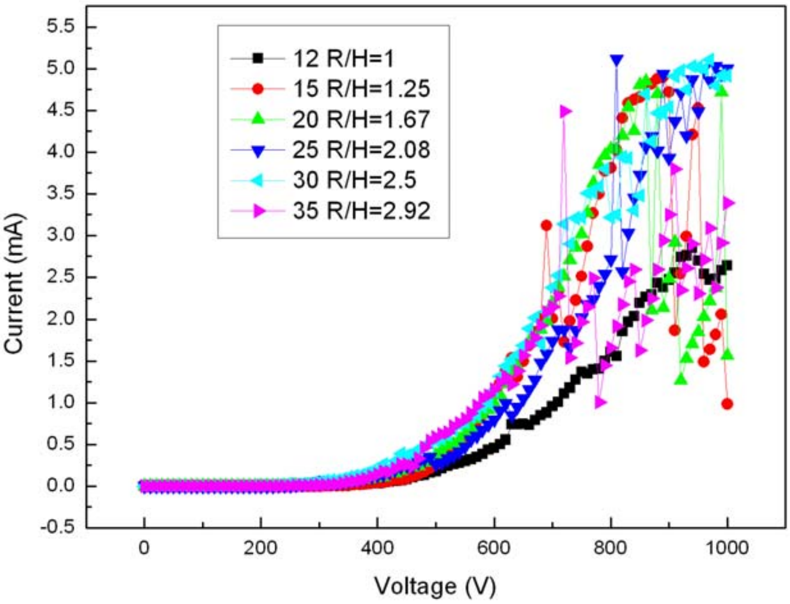

(a)

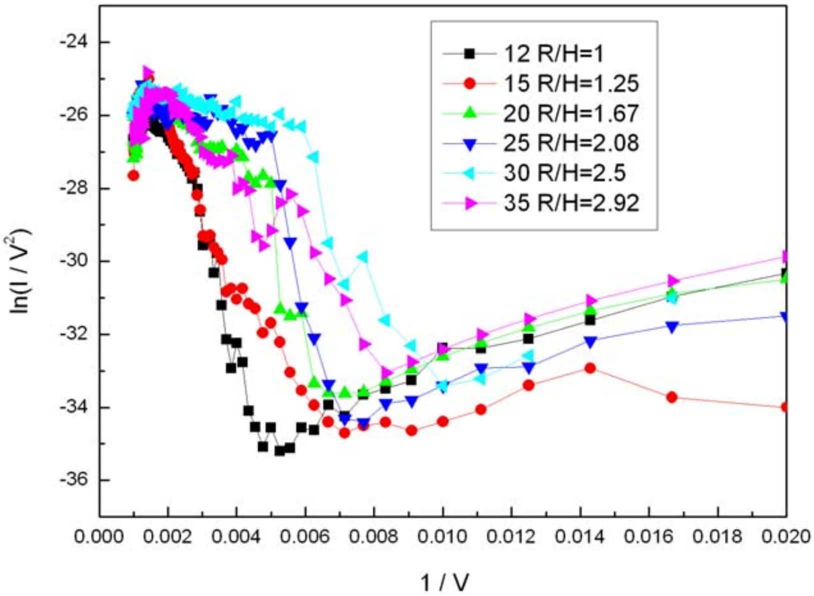

(b)

Figure 3-13 Field emission properties of CNT pillars with different spacing between pillars for growth time of 15 min. (a) I-V curve and (b) F-N plot.

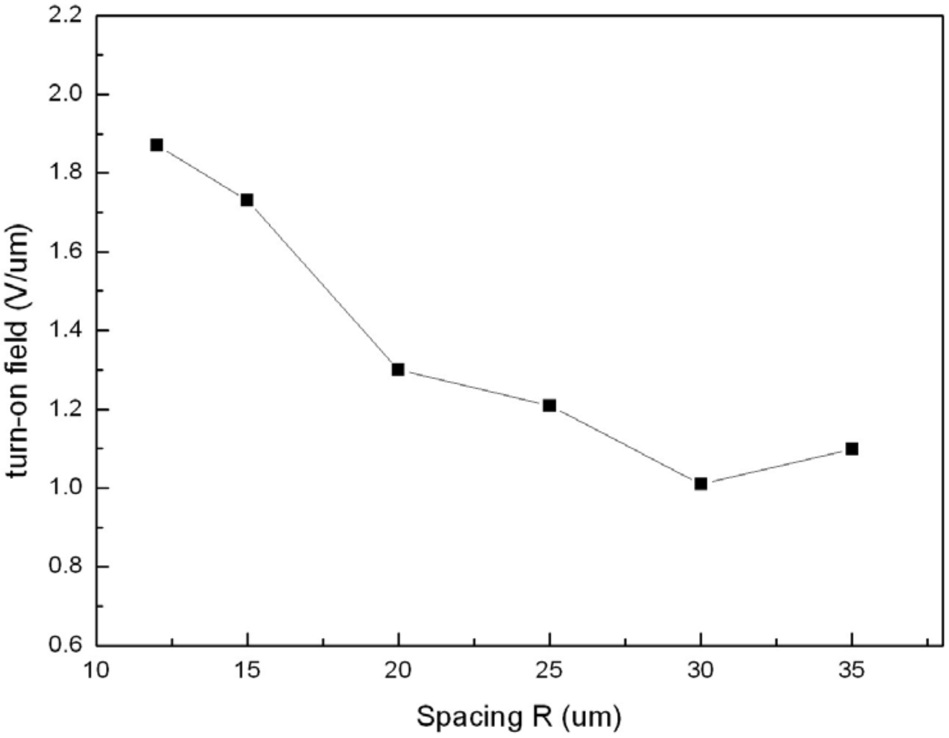

Figure 3-14 The curve of turn-on field versus interpillar spacing for the CNT pillars for growth time of 15 min.

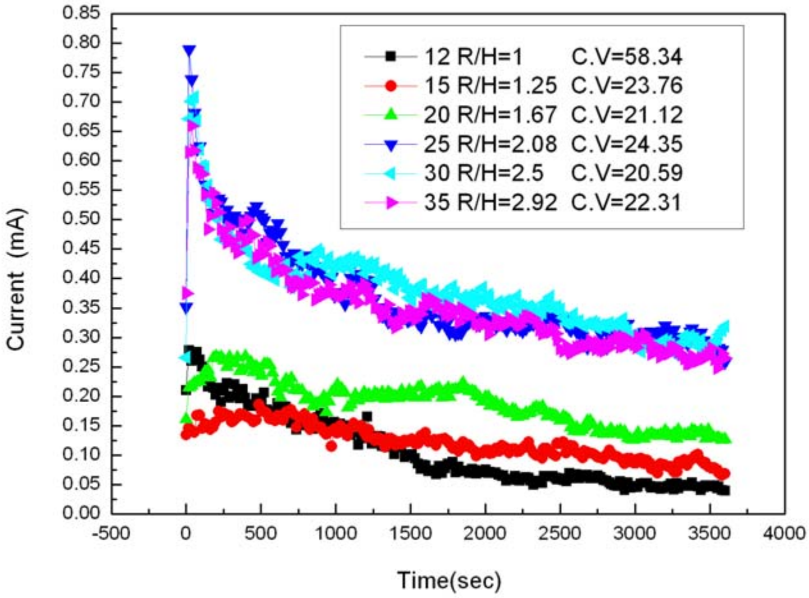

(a)

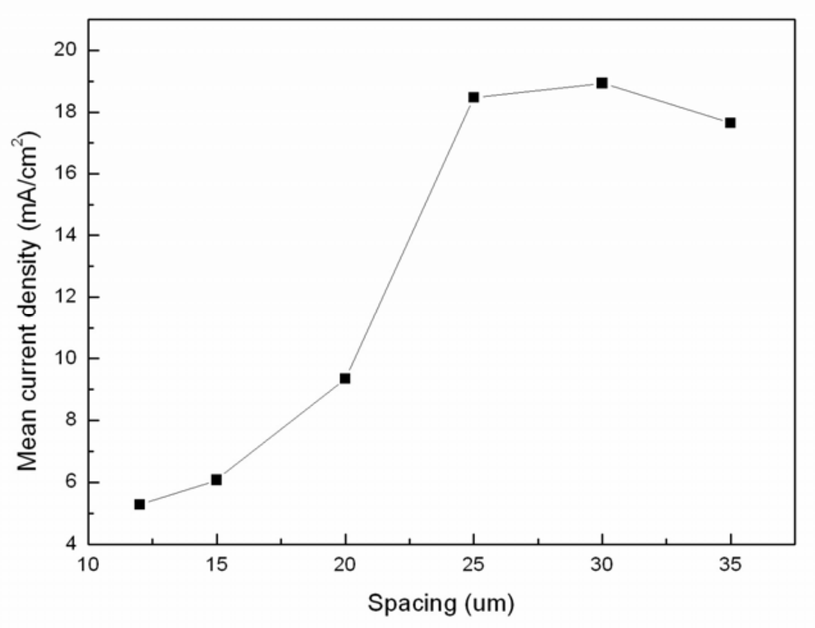

(b)

Figure 3-15 (a) Field emission properties of CNTs with different spacing between pillars at 800 V for 1 hour and (b) the mean current density at 800 V for 1hr versus different spacing for growth time of 15 min.

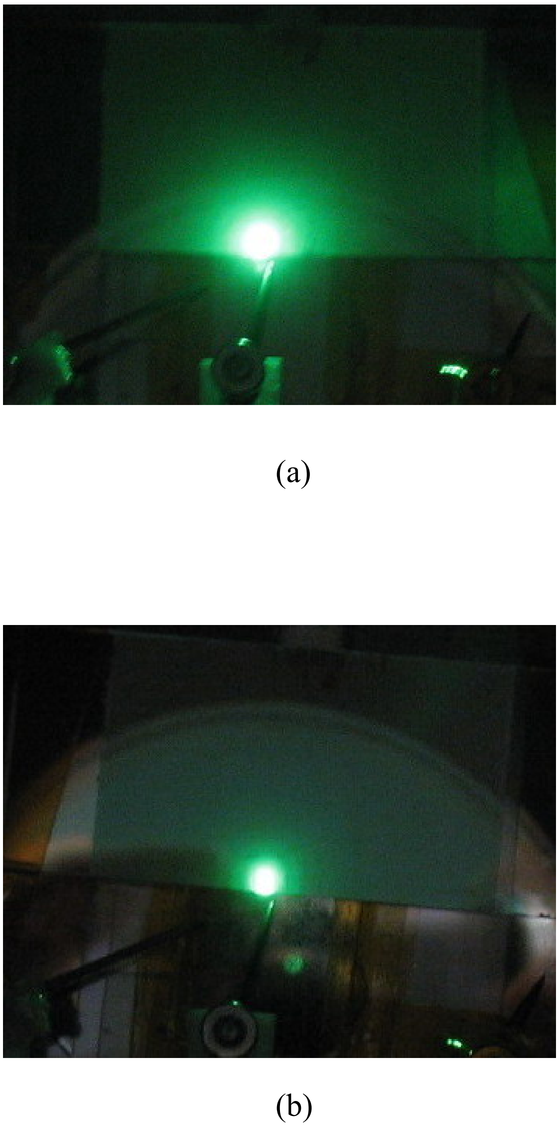

Figure 3-16 The field emission fluorescent images of the CNT pillars with H of 12 μm and R of 30 μm at 800 V (5.33 V/μm) (a) initially and (b) after 1 hr.

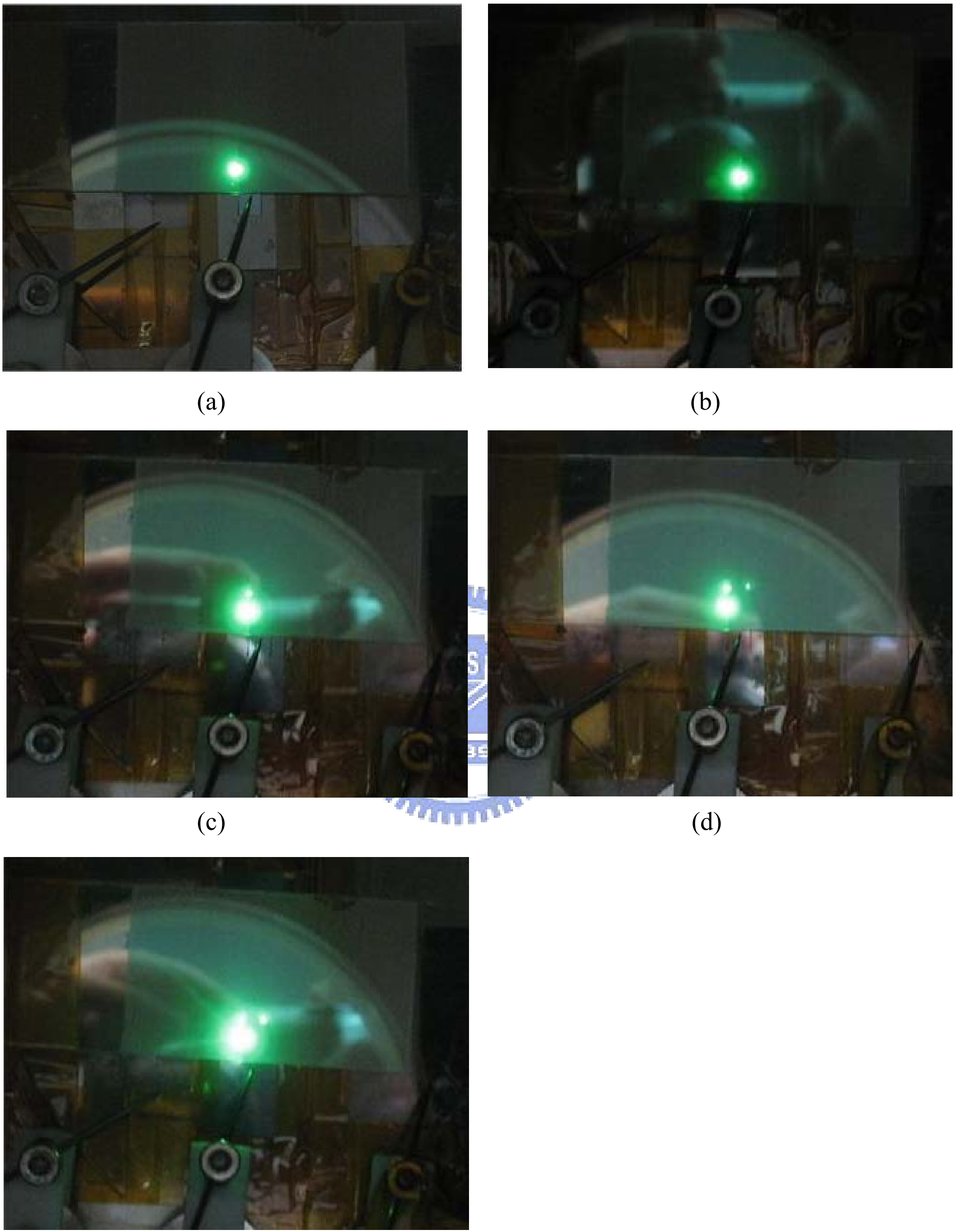

(a) (b)

(c) (d)

(e)

Figure 3-17 The field emission fluorescent images of the CNT pillars with H of 12 μm and R of 30 μm for (a) 400 V (2.67 V/μm), (b) 500 V (3.33 V/μm), (c) 600 V (4 V/μm), (d) 700 V (4.67 V/μm), and (e) 800 V (5.33 V/μm).

(a) (b) (c) (d) (e)

Figure 3-18 The field emission fluorescent images of the full plane CNTs for growth time of 15 min (a) 400 V (2.67 V/μm), (b) 500 V (3.33 V/μm), (c) 600 V (4 V/μm), (d) 700 V (4.67 V/μm), and (e) 800 V (5.33 V/μm).

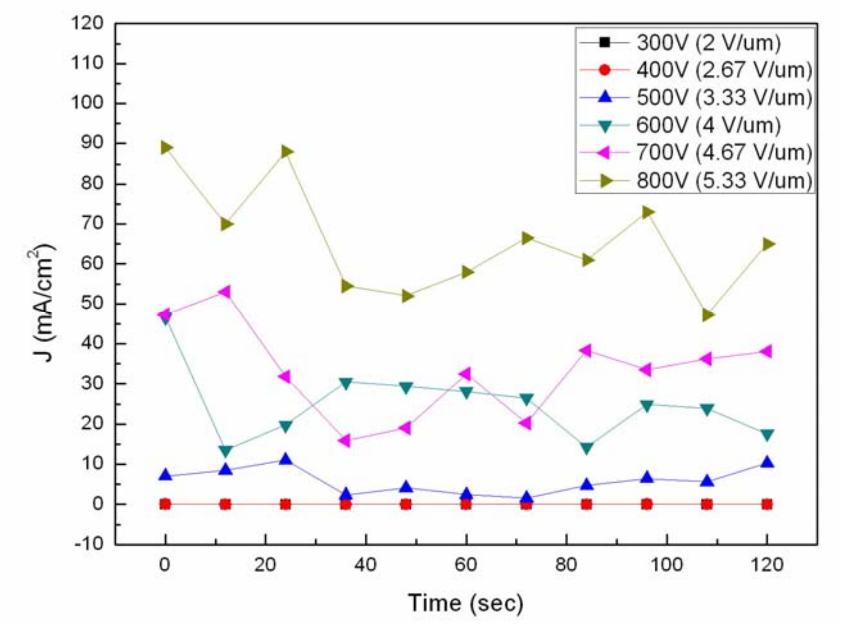

(a)

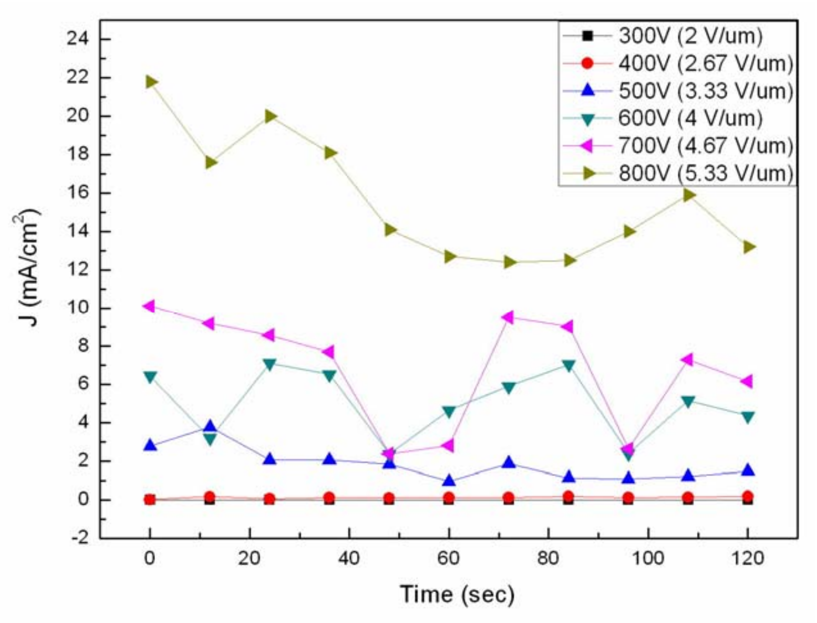

(b)

Figure 3-19 The plots of the field emission current density versus time with different voltages for growth time of 15 min for (a) the CNT pillars and (b) the full plane CNTs.

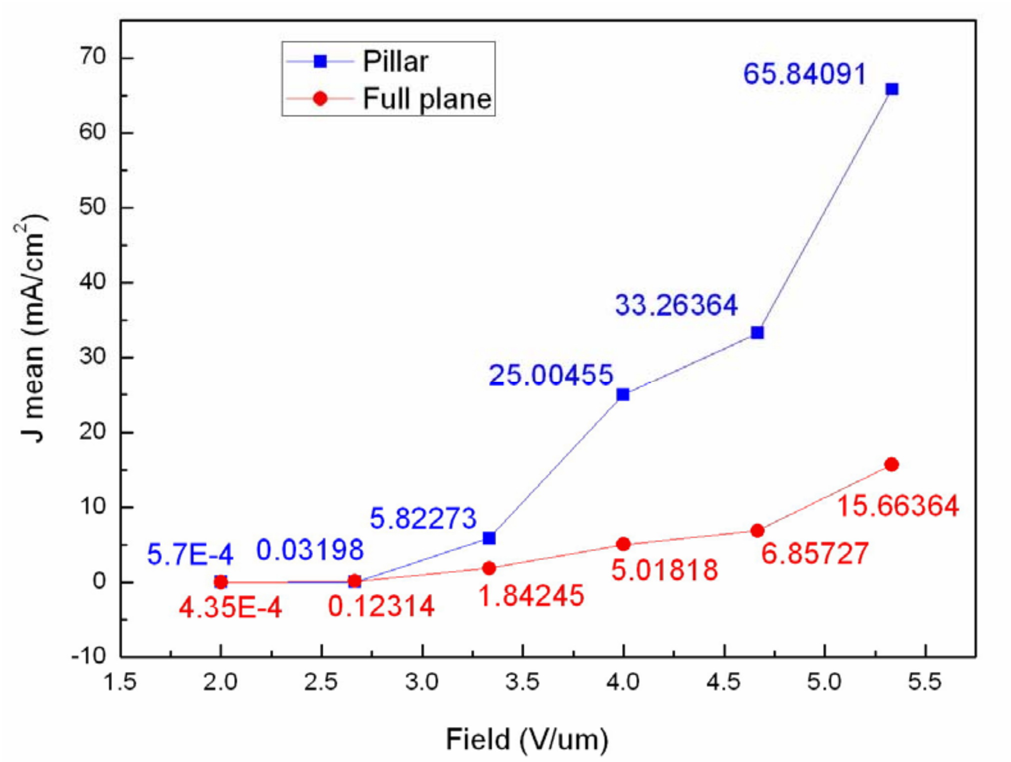

Figure 3-20 The plots of the mean current density versus field under field emission stress test for 120 sec for the CNT pillars and the full plane CNTs.

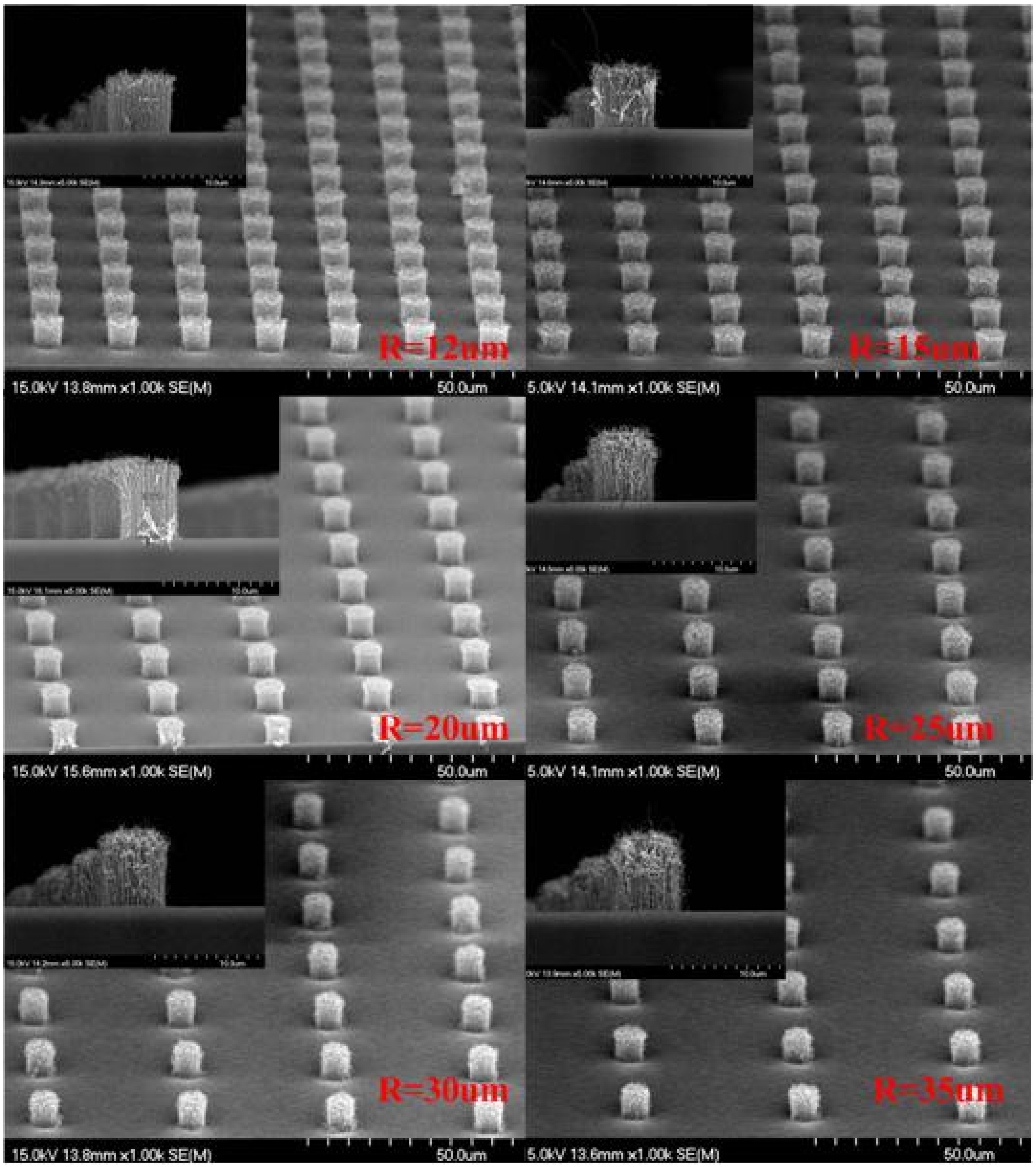

Figure 3-21 The SEM images of CNT pillars in the proposed samples for growth time of 8 min with different R.

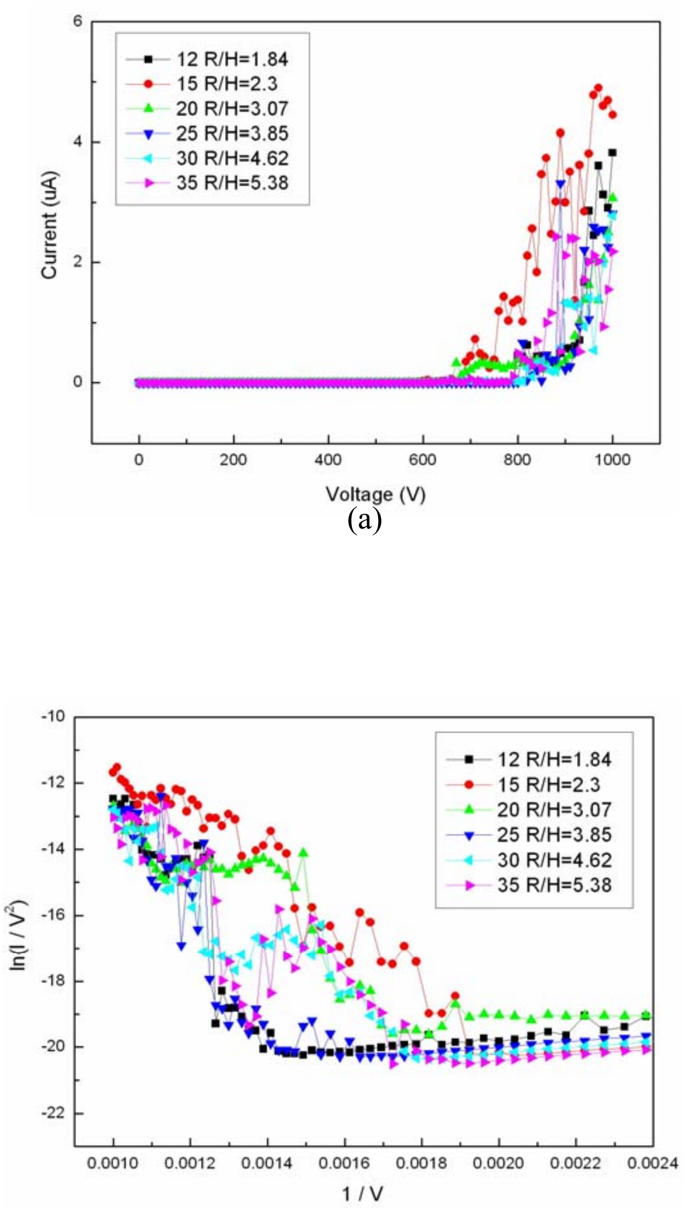

(a)

(b)

Figure 3-22 Field emission properties of CNT pillars for growth time of 8 min with different spacing between pillars. (a) I-V curve and (b) F-N plot.

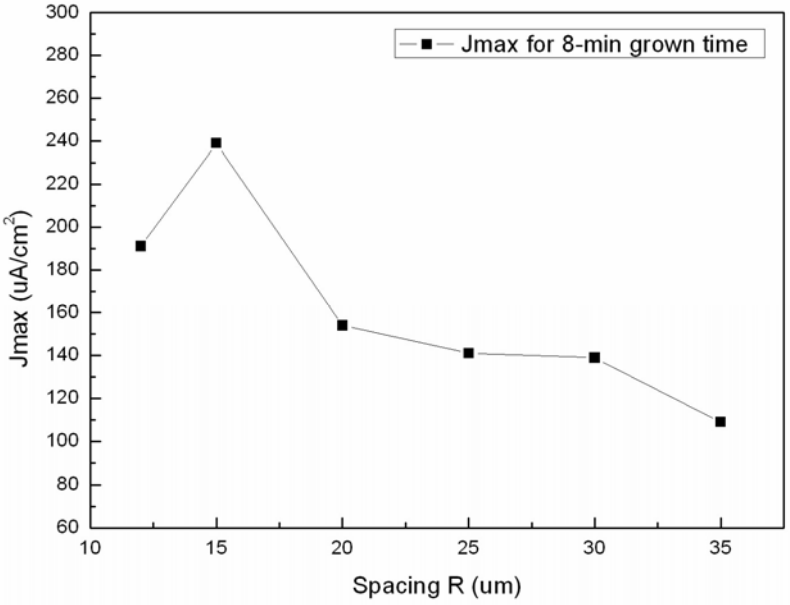

Figure 3-23 The curve of maximum current density versus interpillar spacing for the CNT pillars for growth time of 8 min.

References

Chapter 1

[1.1] J. Bardeen and W. H. Brattain, "The Transistor, A Semi-Conductor Triode," Phys. Rev., vol.74, pp.230-231, 1948.

[1.2] C. A. Spindt, I. Brodie, L. Humpnrey, and E. R. Westerberg, "Electrical Properties of Thin-film Field Emission Cathodes with Molybdenum Cones," J. Appl. Phys., vol. 47, p. 5248, 1976.

[1.3] S. M. Sze, "Physics of Semiconductor Devices," 2nd ed., John-Wiley & Sons pulisher, New York, p. 648, 1981.

[1.4] R. H. Fowler and L. W. Nordheim, "Electron Emission in Intense Field," Proc. R. SOC. A229, pp. 173-181, 1928.

[1.5] S. Itoh, T. Watanabe, T. Yamaura, and K. Yano, "A Challenge to Field Emission Displays," in Proc. Asia Display, pp. 617-620, Oct. 1995.

[1.6] R. Meyer, "Recent Development on Microtips Display at LETI," IVMC'91 Technical Digest, pp. 6-9, 1991.

[1.7] N. E. McGruer and K. Warner, "Oxidation-sharpened Gated Field Emitter Array Process," IEEE Trans. Electron Devices, vol. 38, no. 10, pp. 2389-2391, 1991.

[1.8] S. E. Huq and L. Chen, "Fabrication of sub-10 nm Silicon Tips: A New Approach," J. Vac. Sci. & Technol. B, vol. 13, no. 6, pp. 2718-2721, Nov. 1995.

[1.9] D. W. Branston and D. Stephani, "Field Emission from Metal-coated Silicon Tips," IEEE Trans. Electron Devices, vol. 38, no. 10, pp. 2329-2333, Oct. 1991.

[1.10] V. V. Zhirnov and E. I. Givargizov, "Field Emission from Silicon Spikes with Diamond Coating," J. Vac. Sci. & Technol. B, vol. 13, no. 2, pp. 418-421, 1995.

[1.11] H.G. Kosmahl, "A Wide-bandwidth High-gain Small Size Distributed Amplifier with

Field-emission triodes (FETRODE's) for the 10 to 300 GHz Frequency Rang," IEEE Trans. Electron Devices, vol. 36, no. 11, pp. 2728-2737, Nov. 1989.

[1.12] P. M. Larry, E. A. Netteshiem, Y. Goren, C. A. Spindt, and A. Rosengreen, "10 GHz Turned Amplifier Based on the SRI Thin Film Field Emission Cathode," IEEE IEDM'88, p. 522, 1988.

[1.13] C. A. Spindt, C. E. Hollard, A. Rosengreen, and I. Brodie, "Field Emitter Array Development for High Frequency Operation," J. Vac. Sci. & Technol. B, vol. 11, no. 2, pp. 468-473, Mar./Apr., 1993.

[1.14] C. A. Spindt, "Microfabricated Field Emission and Field Ionization Source," Surface Science, vol. 266, pp.145-154, 1992.

[1.15] T. H. P. Chang, D. P. Kern, et al.," A Scanning Tunneling Microscope Controlled Field Emission Micro Probe System," J. Vac. Sci. & Technol. B, vol. 9, no. 2, pp. 438-443, Mar./Apr., 1991.

[1.16] H. H. Busta, J. E. Pogemiller, and B. J. Zimmerman, "The Field Emission Triode as a Displacement/Process Sensor," J. Micromech. Microeng., p. 45, 1993.

[1.17] H. C. Lee and R. S. Huang, "A Novel Field Emission Array Pressure Sensor," IEEE Transducers- International Solid-State Sensors and Actuators, pp. 241-244, 1991.

[1.18] P. Vaudaine and R. Meyer, "Microtips Fluorescent Display," IEEE IEDM'91, pp. 197-200, 1991.

[1.19] C. Curtin, "The Field Emission Display," International Display Research Conference, p. 12, 1991.

[1.20] C. A. Spindt, C. E. Holland, I. Brodie, J. B. Mooney, and E. R Westerbeng, "Field-emitter Array Applied to Vacuum Fluorescent Displays," IEEE Trans. Electron Devices, vol. 36, no. 1, p. 225, 1989.

[1.21] David A. Cathey, " Field emission display," Information Display, p. 16, Oct.,1995.

[1.22] “Pixtech to Produce Color FEDs from November,” News reported in Nikkei Electronics ASIA, p. 42, Nov., 1995.

[1.23] http://en.wikipedia.org/wiki/Image:Cathode_ray_Tube.PNG

[1.24] R. E. Burgess, H. Kroemer, and J. M. Honston, “Corrected Value of Fowler-Norheim Field Emission Function v(y) and s(y),” Phys. Rev., vol. 1, no. 4, p. 515, May 1953.

[1.25] R. B. Marcus, T. S. Ravi, T. Gmitter, H. H. Busta, J. T. Niccum, K. K. Chin, and D. Liu, “Atomically Sharp Silicon and Metal Field Emitters,” IEEE Trans. Electron Devices, vol. 38, no. 10, pp. 2289-2294, Oct. 1991.

[1.26] C. A. Spindt, “A Thin Film Emission Cathode,” J. Appl. Phys., vol. 39, pp. 3504-3505, 1968.

[1.27] R. Meyer, A. Ghis, P. Rambaud, and F. Muller, “Microtips Fluores-cent Display,” in Proc. Japan Display, pp. 512-514, Sept./Oct. 1986.

[1.28] S. Itoh AND M. Tanaka, “Current Status of Field-Emission Displays”, Proceedings of the IEEE, vol. 90, no. 4, pp. 514-520, April. 2002.

[1.29] M. Ding, H. Kim, and A. I. Akinwande “Highly Uniform and Low Turn-On Voltage Si Field Emitter Arrays Fabricated Using Chemical Mechanical Polishing”, IEEE Electron Device Letters, vol. 21, no. 2, pp. 66-69, Feb. 2000.

[1.30] J Itoh, Y Tohma, K Morigawa, S. Kanemaru and K. Shimizu “Fabrication of Double Gate Si Field Emitter Arrays for Focused Electron Beam Generation” J. Vac. Sci. & Technol. B., vol. 13, no. 5, pp. 1968-1972, 1995.

[1.31] K. Yamamoto, I. Nomura, K. Yamazaki, S. Uzawa and K. Hatanaka, “Fabrication and Characterization of Surface Conduction Electron Emitters,” SID Digest, pp. 1933-1935, 2005.

[1.32] T. Oguchi, E. Yamaguchi, K. Sasaki, K. Suzuki, S. Uzawa and K. Hatanake, “A 36-inch Surface Conduction Electron Emitter Display (SED) ,” SID Digest, pp.

1929-1931, 2005.

[1.33] S. Iijima, “Helical Microtubules of Graphitic Carbon,” Nature, vol. 354, pp. 56-58, Nov. 1991.

[1.34] M. S. Dresselhaus, G. Dresselhaus, K. Sugihara, L. I. Spain, and H. A. Goldberg, “Graphite Fibers and Filaments,” Springer-Verlag, New York, 1998.

[1.35] P. M. Ajayan, “Nanotubes from carbon,” Chem. Rev., vol. 99, pp. 1787-1880, 1999.

[1.36] S. Iijima and T. Ichihashi, “Single-shell Carbon Nanotubes of 1-nm Diameter,” Nature, vol. 363, pp. 603-605, Jun. 1993.

[1.37] D. S. Bethune, C. H. Kiang, M. S. de Vries, G. Gorman, R. Savoy, J. Vazquez, and R. Beyers, “Cobalt-catalyzed Growth of Carbon Nanotubes with Single-atomic-layer Walls,” Nature, vol. 363, pp. 605-607, 1993.

[1.38] http://en.wikipedia.org/wiki/Image:CNTnames.png

[1.39] http://online.itp.ucsb.edu/online/qhall_c98/dekker/

[1.40] Y. K. Kwon, T. H. Lee, S. G. Kim, P. Jund, D. Tomanek, and R. E. Smalley. “Morphology and Stability of Growing Multiwall Carbon Nanotubes,” Phys Rev. Lett., vol. 79, pp. 2065-2068, 1997.

[1.41] Y. Saito, “Carbon Nanotubes: Preparation and Physical Properties,” Asia Display/IDW’01, p. 11, 2001.

[1.42] Min-Feng Yu et al., “Strength and Breaking Mechanism of Multiwalled Carbon Nanotubes Under Tensile Load,” Science, vol. 287, pp. 637-640, 2000.

[1.43] Philip G. Collins and Phaedon Avouris, “Nanotubes for Electronics,” Scientific American , pp. 62-69, Dec. 2000.

[1.44] A. Thess, R. Lee, R. E. Smalley, “Crystalline Ropes of Metallic Carbon Nanotubes,” Science, vol.273, pp. 483-487, July 1996.

[1.45] H. M. Cheng, F. Li., H. Y. Pan, M. S. Dresselhaus, “Large-scale and low-cost synthesis of single-walled carbon nanotubes by the catalytic pyrolysis of hydrocarbons," Appl. Phys. Lett., vol. 72, no. 25, pp. 3282-3284, June 1998.

[1.46] Z. F. Ren, Z. P. Huang, P. N. Provencio, " Synthesis of Large Arrays of Well-aligned Carbon Nanotubes on Glass," Science, vol. 282, pp. 1105-1107, 1998.

[1.47] Z.W. Pan, S. S. Xie, W. Y. Zhou, G. Wang, "Direct Growth of Aligned Open Carbon Nanotubes by Chemical Vapor Deposition," Chem. Phys. Lett., vol. 299, no. 1, pp. 97-102, 1999.

[1.48] C. J. Lee, D. W. Kim, "Synthesis of Aligned Carbon Nanotubes Using Thermal Chemical Vapor Deposition," Chem. Phys. Lett., vol. 312, no. 5-6, pp. 461-468, 1999.

[1.49] C. Bower, W. Zhu, D. Shalom, "On-chip Vacuum Microtriode Using Carbon Nanotube Field Emitters," Appl. Phys. Lett., vol. 80, no. 20, pp. 3820-3822, 2000.

[1.50] W. A. de Heer, A. Chateline, D. Ugrate, "A Carbon Nanotube Field-emission Electron Source," Science, vol. 270, pp. 1179-1180, 1995.

[1.51] J. Dai, J. H. Hafner, A. G. Rinzler, "Large-scale Production of Single-walled Carbon Nanotubes by the Electric-arc Technique," Nature, vol. 388, pp. 756-758, 1997.

[1.52] F. Yuan and H. Ryu, Nanotechnology 15, S596, 2004.

[1.53] Y. C. Kim and E. H. Yoo, "Printed Carbon Nanotube Field Emitters for Backlight Applications," Jpn. J. of Appl. Phys., vol.44, no.11, pp. L454-L456, 2005.

[1.54] X. Xu and G. R. Brandes, "A Method for Fabricating Large-area, Patterned, Carbon Nanotube Field Emitters," Appl. Phys. Lett., vol. 74, no. 17, pp. 2549-1551, April 1999.

[1.55] A. M. Rao, D. Jacques, and R. C. Haddon, "In Situ-grown Carbon Nanotube Arrays with Excellent Field Emission Characteristics," Appl. Phys. Lett., vol. 76, no. 25, pp. 3813-3815, 2000.

[1.56] H. Murakami, M. Hirakawa, C. Tanaka, and H. Yamakawa, "Field Emission from Well-aligned, Patterned, Carbon Nanotube Emitters," Appl. Phys. Lett., vol. 76, no. 9, pp. 1176-1178, Feb. 2000.

[1.57] W. B. Choi, D. S. Chung, J. H. Kang, H. Y. Kim, Y. W. Jin, I. T. Han, Y. H. Lee, J. E. Jung, N. S. Lee, G. S. Park, and J. M. Kim, "Fully Sealed, High-brightness Carbon-nanotube Field-emission Display," Appl. Phys. Lett., vol. 75, no. 20, pp. 3129-3131, 1999.

Chapter 2

[2.1] Y. K. Kwon, T. H. Lee, S. G. Kim, P. Jund, D. Tomanek, and R. E. Smalley. “Morphology and Stability of Growing Multiwall Carbon Nanotubes,” Phys Rev. Lett., vol. 79, pp. 2065-2068, 1997.

[2.2] Y. Saito, “Carbon Nanotubes: Preparation and Physical Properties,” Asia Display/IDW’01, p. 11, 2001.

[2.3] M. Okai, T. Fujieda, K. Hidaka, T. Muneyyoshi, and T. Yaguchi, “In Situ Transmission Electron Microscope Observation of Carbon Nanotubes in Electric Fields ,” Jpn. J. of Appl. Phys. vol. 44, no. 4A, pp. 2051-2055, 2005.

[2.4] Jean-Marc Bonard and Christian Klinke, “Degradation and Failure of Carbon Nanotube Field Emitters,” Phys. Rev. B, vol. 67, no. 11, p. 115406, 2003.

[2.5] Jae-Hee Han, Su Hong Lee, A.S. Berdinsky, “Effects of Various Post-treatments on Carbon Nanotube Films for Reliable Field Emission,” Diamond & Related Materials, vol. 14, pp. 1891-1896, 2005.

[2.6] Chaogang Lou, Xiaobing Zhang, Wei Lei, and Chen Qi, “New Method to Fabricate Field-emission Cathode of Carbon Nanotubes,” Applied Surface Science, vo. 251, pp. 254–257, 2005.

[2.7] J. M. Lauerhaas, J. Y. Dai, A. A. Setlur, and R. P. H. Chang, “The Effect of Arc Parameters on the Growth of Carbon Nanotubes,” J. Mater. Res., vol. 12, no. 6, pp. 1536-1544, June 1997.

[2.8] A. G. Rinzler, J. Liu, H. Dai, P. Nikolaev, and R. E. Smaley, “Large-scale Purification of Single-wall Carbon Nanotubes: Process, Product, and Characterization,” Appl. Phys. A, vol. 67, pp. 29-37, 1998.

[2.9] M Meyyappan, Lance Delzeit, Alan Cassell, and David Hash, “Carbon Nanotube Growth by PECVD: A Review,” Plasma Sources Sci. Technol., vol. 12, pp. 205-216, 2003.

[2.10] Y. S. Woo, I. T. Han, Y. J. Park, and J. M. Kim, "Effect of Ion Bombardment on Microstructures of Carbon Nanotubes Grown by Electron Cyclotron Resonance Chemical Vapor Deposition at Low Temperatures," Jpn. J. Appl. Phys., vol. 42, pp. 1410-1413, 2003.

[2.11] C. J. Lee, K. H. Son, J. Park, J. E. Yoo, Y. Huh, and J. Y. Lee, " Low Temperature Growth of Vertically Aligned Carbon Nnanotubes by Thermal Chemical Deposition," Chem. Phys. Lett., vol. 338, p. 113, 2001.

[2.12] Q. Jiang, N. Aya, and F. G. Shi, "Nanotube Sized-dependent Melting of Single Crystals in Carbon Nanotubes," Appl. Phys. A 64, pp. 627-629, 1997.

[2.13] W. H. Oi, "Size Effect on Melting Temperature of Nanosolid," Physica B, vol. 368, pp. 46-50, 2005.

[2.14] Huang-Chung Cheng, Rui-Ling Lai, Yao-Ren Chang, Kao-Chao Lin, Chuan-Ping Juan, Pei-Chi Chang, Chien-Ying Lee, and Jiun-Kai Shiu, "Improvement of Luminescent Uniformity via Synthesizing the Carbon Nanotubes on an Fe–Ti Co-deposited Catalytic Layer," Japanese Journal of Applied Physics, vol. 46, No. 2, pp. 863-866, 2007.

[2.15] M. Alden, H. L. Skriver, S. Mirbt, and B. Johansson, "Surface Magnetism in Iron, Cobalt, and Nickel," Phys. Rev. Lett. vol. 69, pp. 2296-2298, 1992.

[2.16] Michael J. Bronikowski, "CVD Growth of Carbon Nanotube Bundle Arrays," Carbon, vol. 44, pp. 1822-2832, 2006.

Chapter 3

[3.1] W. A. de Heer, A. Chatelain, D. Urgate, “A Carbon Nanotube Field-Emission Electron Source,” Science, vol. 270, no. 5239, pp. 1179-1180, 1995.

[3.2] G. Z. Yue, Q. Qiu, Bo Gao, Y. Cheng, J. Zhang, H. Shimoda, S. Chang, J. P. Lu, and O. Zhoua, “Generation of Continuous and Pulsed Diagnostic Imaging X-ray Radiation Using A Carbon-nanotube-based Field-emission Cathode,” Appl. Phys. Lett., vol. 81, no. 2, pp. 355-357, 2002.

[3.3] D. J. Lee, S. I. Monn, Y. H. Lee, J. E. Yoo, J. H. Park, J. Jang, B. K. Ju, “The Vacuum Packaging of a Flat Lamp Using Thermally Grown Carbon Nano Tubes,” Vacuum, No. 74, pp. 105-111, 2004.

[3.4] R. L. Fink, Z. Li Tolt, Z. Yaniv, “The Status and Future of Diamond Thin Film FED,” Surf. Coat. Technol., no. 108-109, pp. 570-576, 1998.

[3.5] ITRI / MRL / IEK

[3.6] T. H. Tsou, M. H. Lin, B. N. Lin, W. Y. Lin, Y. C. Jiang, C. H. Lee, Y. Ohgi, H. Hiraki, M. C. Hsiao, and C. C. Lee, “Reflective Structure for Carbon Nano-Tube Backlight Unit,” IDW/AD’05, pp. 1695-1696, 2005.

[3.7] L. Nilsson, O. Groening, C. Emmenegger, O. Kuettel, E. Schaller, L. Schlapbach, H. Kind, J-M. Bonard, and K. Kern, “Scanning Field Emission from Patterned Carbon Nanotube Films,” Appl. Phys. Lett., vol. 76, no. 15, pp. 2071-2073, 2000.

[3.8] Jean-Marc Bonard, Mirco Croci, Christian Klinke, Ralph Kurt, Olivier Noury, and Nicolas Weiss, “Carbon Nanotube Films as Electron Field Emitters,” Carbon, vol. 40, pp. 1715-1728, 2002.

[3.9] Suh JS, Jeong KS, Lee JS, Han IT. “Study of the Field-screening Effect of Highly Ordered Carbon Nanotube Arrays,”Appl. Phys. Lett., vol. 80, no. 13, pp. 2392-2394, 2002.

[3.10] Michael J. Bronikowski, “CVD Growth of Carbon Nanotube Bundle Arrays,” Carbon, vol. 44, pp. 2822-2832, 2006.

簡歷

姓名: 張佩琪

性別: 女

生日: 民國七十二年四月二十四日

籍貫: 台南市

地址: 台南市西和路105號

學歷: 國立台南女子高級中學

（87年9月～90年6月）

國立清華大學材料科學工程學系

(90年9月～94年6月)

國立交通大學電子工程研究所碩士班

(94年9月～96年8月)

論文題目:利用鐵鈦共鍍催化金屬合成柱狀結構之奈米碳管之場發射特性的研究

Study on the Field Emission Characteristics of the Carbon Nanotube Pillars Synthesized from an Fe-Ti Codeposited Catalyst